Competition of ground states in URu2Si2 and UCoGe

Elena Hassinger

Université de Grenoble
Ecole doctorale de Physique de Grenoble

Doctorat
Physique

Elena Hassinger

Compétition d'états fondamentaux dans URu_2Si_2 et UCoGe

Soutenue le 26 octobre 2010 devant la Commission d'Examen :

C. Berthier	Président
H. Amitsuka	Rapporteur
A. de Visser	Rapporteur
C. Geibel	Examinateur
G. Knebel	Examinateur
J. Flouquet	Examinateur

Thèse préparée sous la direction de
Jacques Flouquet
au sein du Service de Physique Statistique, Magnétisme et Supraconductivité, INAC, CEA Grenoble

Competition of ground states in URu_2Si_2 and UCoGe

Abstract

In this thesis, two uranium based heavy fermion compounds are studied under pressure.

URu_2Si_2 has a mysterious ground state below $T_0 = 17.5\,\mathrm{K}$ at ambient pressure. The order parameter has not been identified yet which led to the name "hidden order" (HO). In addition, below 1.5 K the system becomes superconducting. With pressure, the ground state switches from the HO phase to an antiferromagnetic (AF) phase at a critical pressure and superconductivity is concomitantly suppressed. Shubnikov-de Haas measurements under pressure show that the Fermi surface doesn't change between the two phases. The folding of the Fermi surface which occurs in the high pressure AF phase therefore already happens in the HO phase, indicating a unit cell doubling. Our measurements of the complete angular dependence of the oscillation frequencies test the electronic structure and support new theoretical band structure calculations with rather itinerant $5f$ electrons.

The second part of my research focuses on another uranium compound, UCoGe. It is one of the few known materials where superconductivity ($T_{sc} = 0.6\,\mathrm{K}$) coexists with ferromagnetism ($T_{Curie} = 2.8\,\mathrm{K}$). Precise studies of the pressure phase diagram by resistivity, ac calorimetry and ac susceptibility show that the ferromagnetic phase is suppressed at a pressure of about 1 GPa and the superconducting phase extends into the paramagnetic phase induced by pressure. When ferromagnetism is suppressed to the superconducting transition no further distinct ferromagnetic anomalies are observed. Thus, the pressure phase diagram of UCoGe is unique in the class of ferromagnetic superconductors.

Key words

heavy fermion systems
URu_2Si_2, hidden order
UCoGe, ferromagnetic superconductors
pressure phase diagram
quantum oscillations

Acknowledgements
Danksagung
Remerciements

Many people have contributed to this work. Without them, this thesis would have 0 pages.

First of all I thank Hiroshi Amitsuka, Claude Bertier, Christoph Geibel and Anne de Visser, the jury of my thesis defence, for coming partly from very far to take part in this important moment in my life.

Jacques, j'ai eu la chance d'être une de tes thésards, d'apprendre une toute petite partie de ton savoir sur les électrons corrélés. J'admire ta connaissance des humains, tes jugements et la façon, dont tu arrives à motiver les gens au labo.

Einen riesen Dank an Georg, den besten Betreuer und Büronachbar, den ich haben konnte. Wir kennen uns seit 6 Jahren, davon 4 Jahre in intensiver Zusammenarbeit. Die viele Zeit zum Diskutieren über die Physik und das Leben verbindet.

Frédéric, merci de m'avoir laissé faire partie de ton monde de neutroniciens de URu_2Si_2. On a bien travaillé ensemble, je trouve.

Je remercie les techniciens du labo Marie-Jo, Jean-Michel, Michel, Pierre et Frédéric. Leur soutien constant fait fonctionner le labo de facon fluide.

Je remercie Marie-Jo et Daniel pour l'introduction aux techniques de pression avec des cellules diamant.

For helpful and enriching discussions I thank the theoreticians V. Mineev, G. Kotliar, C. Haule, P. Oppeneer and especially H. Harima for doing the calculations we asked for. Your images helped me a lot in understanding the effect of folding on the Fermi surface.

Béatrice, chapeau pour ton travail d'enseignement et merci pour tes conseils et ton soutien.

What would be a lab without the people working and spending a good part of their life in it?
J'ai gagné des amis: Valentin, qui me fait rigoler, Ludovic, qui nous invite à manger du bon fromage dans toutes les formes possibles, Giorgos, immer aufrichtig und so lieb und sozial wie wenige Leute, die ich kenne, Estelle, qui arrive à tout prendre comme ça vient. And I spent moments that I don't want to miss with Amalia, Liam, Tatsuma, Hisachi, Alain, Daniel, Dai, Jean-Pascal, Jonathan, Alexandra, Thomas, Matthieu, Stéphane. C'est dommage qu'on a pas commencé à se voir plus tôt dans la thèse avec les thésards théoriciens du C5.
Vielen Dank für den Doktorhut. Das war eine super schöne Überraschung.

Mama, Papa und Irene brauche ich nicht zu danken. Sie wissen auch so, wie dankbar

ich bin für ihre bedingungslose Unterstützung in allen Lebenslagen. Auch wenn ich jetzt in Kanada bin, mein Herz ist bei Euch.

Pierre-Jean, ich bin so froh, mit dir zusammen zu sein.

Contents

Introduction

By varying the lattice constants of a crystal, the strength of the electronic and magnetic exchange interactions change. If two different ground-states lie energetically close together, a change of exchange energy can alter the ground state. Hydrostatic pressure is therefore a clean tuning parameter to change the ground state of a correlated electron system near a magnetic instability. In heavy fermion systems, rich pressure phase diagrams often reveal new physics, such as non-Fermi liquid behavior, the interplay of magnetism and superconductivity, the coexistence of ferromagnetism and superconductivity or quantum critical phenomena. In this study, two uranium based heavy fermion systems with interesting pressure phase diagrams have been investigated.

URu_2Si_2 has a mysterious ground state below $T_0 = 17.5\,\mathrm{K}$ at ambient pressure. Despite over 25 years of research, the order parameter has not been identified yet, which led to the name "hidden order" (HO). The basic problem is that at the transition, the entropy loss is huge (0.2Rln2) but the phase is non magnetic. Additionally, at low temperature (1.5 K) the system becomes superconducting. A variety of theories exist for an order parameter that could provide such an entropy loss (multipolar orderings of all types, dynamical spin density waves, helical order, hybridization wave...). However, it has not yet been possible to detect the order parameter.

Under pressure, the ground state switches to an antiferromagnetic (AF) spin density wave state and the superconductivity is suppressed at the same pressure. Even though the HO phase and the AF phase are separated by a first order transition line, many physical properties have a very similar temperature behavior in both phases. For example the spin-density wave like anomaly in resistivity is the same for all pressures. Neutron scattering measurements by our group were able to identify a significant magnetic excitation in the HO state at the same wave vector as the AF ordering vector Q_{AF}. It is so far the only microscopic signature of the HO state. The temperature dependence of its intensity follows an order parameter like behavior below T_0, indicating that Q_{AF} is the ordering vector also in the HO state. In this case, the Fermi surface which is reconstructed at the ordering temperatures, will be the same in both HO phase and AF phase. In order to see if the Fermi surface changes, this study reports measurements of the Shubnikov-de Haas effect at several pressures on new very high quality crystals. The measurements show that the Fermi surface does not change between the two phases, and therefore support the previous hypothesis. New proposals for the HO parameter have been published with different degrees of localization of the $5f$-electrons and therefore very different electronic structures. My measurements of the complete angular dependence of the oscillation frequencies test the electronic structure and therefore provide an excellent test of the new theoretical propositions for the still unknown order parameter.

The second part of this work focuses on another uranium compound, UCoGe. It is one

of the few known materials where superconductivity ($T_{sc} = 0.6\,\mathrm{K}$) coexists with ferromagnetism ($T_{Curie} = 2.8\,\mathrm{K}$). The theoretical understanding of the pressure phase diagram of a ferromagnetic superconductor near the critical pressure is to date incomplete, because all the known ferromagnetic materials have a first order transition and theories exist only for a second order transition. The aim in this study is to establish the pressure phase diagram of UCoGe which is the third ferromagnetic superconducting material after UGe_2 and UIr where the critical point can be reached by applying pressure. It has a very small ordered moment and is estimated very close to the critical point. Precise studies of the pressure phase diagram by resistivity, ac calorimetry and ac susceptibility show that the ferromagnetic phase is suppressed at a pressure of about 1 GPa and that UCoGe is the only known ferromagnetic superconductor where the superconducting phase extends into the paramagnetic phase induced by pressure. Ferromagnetism is rapidly suppressed when superconductivity appears first on cooling. Thus, its pressure phase diagram is different of the phase diagram of other known ferromagnetic superconductors. The superconducting phase inside the ferromagnetic phase is smoothly connected to the superconducting state outside the ferromagnetic state, although the superconducting order parameter will inevitably break different symmetries. No conclusive answer can be given to the question of the order of the transition. The interplay of ferromagnetism and superconductivity is a new field with many interesting phenomena, for example field-re-entrant superconductivity.

This work is divided into four chapters. The first chapter gives an overview of the important physical phenomena in heavy fermion compounds in general before describing the relevant physical effects, interactions and theoretical models in more detail. The extreme measurement conditions (low temperature, high magnetic field) and pressure techniques are described in chapter 2. Chapter 3 provides an introduction to URu_2Si_2, including the neutron scattering results obtained by our group for my thesis. Subsequently, the results obtained on the Fermi surface of URu_2Si_2 at ambient pressure in the HO state and under pressure in the AF state are presented. The last chapter presents the measured pressure phase diagram of UCoGe.

Chapter 1

Theory

1.1 From normal metals to heavy fermion systems

In a metal, each atom gives its valence electrons to a common electron gas. Despite the Coulomb interaction, the system can be described as a gas of free electrons in the potential of the atomic cores. In the Drude model, the electrons can move freely between two collisions. According to the Pauli principle, the electrons fill up the available energy states up to the Fermi energy E_F. The Fermi energy depends on the density of electrons and is very high for normal metals like copper ($E_\mathrm{F} \approx 7\,\mathrm{eV}$, $T_\mathrm{F} \approx 10^5\,\mathrm{K}$). In heavy fermion systems, the Fermi energy is much lower. Heavy fermion compounds are intermetallic compounds which contain rare earth elements like cerium (Ce) or ytterbium (Yb) or actinides like uranium (U). Famous examples are $CeAl_3$ or $CeCu_2Si_2$ (Stewart 1984). These elements have a partly filled $4f$-shell for ytterbium and cerium and $5f$-shell for uranium. The $4f$-states are well localized (see figure 1.1b) in real space, i.e. close to the atomic core compared to the closed $5s$ and $5p$-shells because of the strong centrifugal potential $l(l+1)/r^2$ with orbital quantum number $l = 3$ for f-electrons. Therefore they keep their local atomic like character even in solids. The $2j + 1$ degenerate ground state of angular momentum j is split into well defined crystal field levels. Nevertheless the tail of their wave function at the outside of the closed $5s$ and $5p$-shell is not negligible. This part of the wave function can easily be influenced by the potential energy, crystal field and the distance between the lanthanide atoms and it overlaps with the conduction electron wave function. In energy, the $4f$-level is narrow and lies near the Fermi energy so that the f electrons interact and hybridize with the conduction electrons. This evokes spin- and valence fluctuations. The interaction of the conduction electrons with the local f moment can be described by the Kondo effect and it leads to a participation of the f electrons in the conduction bands and a very high density of states at the Fermi level.

The low temperature behavior of macroscopic properties in heavy fermion systems can generally be described by Landau's Fermi-liquid theory (Enss and Hunklinger 2005), as long as the system is not too close to a critical point driven by a magnetic or valence instability. In this theory strongly interacting fermions are substituted by weakly interacting quasiparticles with an enhanced effective mass. This results in an enhanced specific heat, susceptibility and resistivity-coefficients at low temperature. The high effective cyclotron mass can also directly be measured in quantum oscillation measurements. The most important results of this theory are given in paragraph 1.2.

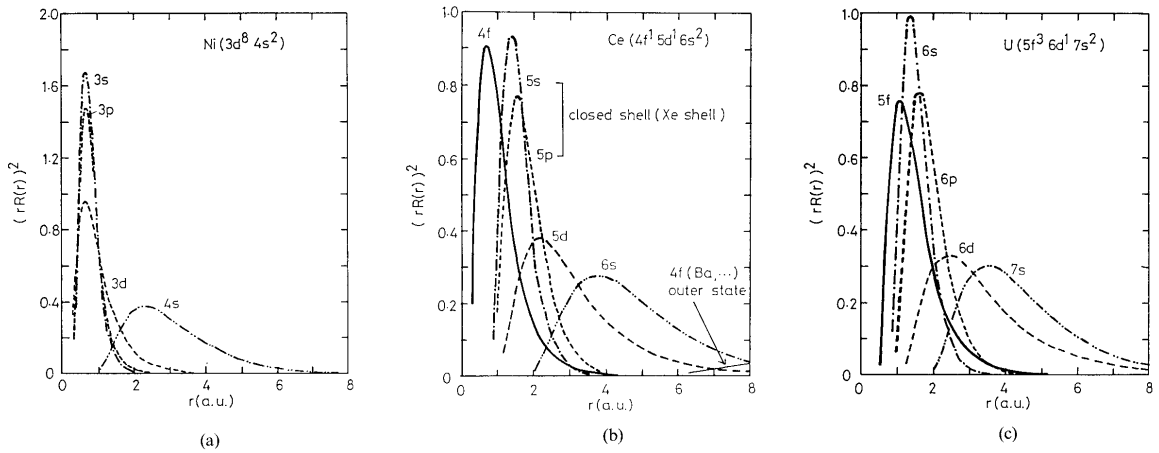

Fig. 1.1 : Effective radial charge densities of (a) Ni, (b) Ce and (c) U atom (Kasuya et al. 1988).

At high temperature these systems show a Curie-Weiss like behavior of the susceptibility $\chi \propto \frac{\mu_{eff}^2}{T-\Theta}$ due to the weakly interacting local magnetic moments of the f-electrons. The Curie-Weiss temperature Θ_{CW} is often negative and the effective magnetic moment μ_{eff} usually larger than 2 μ_B. However, in general it does not exactly correspond to the value calculated by Hund's rules for the electron configuration of the free ion because of the crystal field splitting.

At lower temperatures the local moments are screened by the spins of the conduction electrons like in metals with dilute magnetic impurities as described by the Kondo effect. Additionally the local moments interact indirectly via the conduction electrons by the RKKY interaction (Rudermann and Kittel 1954). The competition between the RKKY interaction which favors long range magnetic order and the moment screening of the Kondo effect leads to different ground states in heavy fermion systems. The Kondo effect, the RKKY interaction and the competition between both interactions are described in paragraph 1.3. At zero temperature the system can be driven from a magnetically ordered ground state to an non-magnetic state by changing a parameter other than temperature. This parameter, normally pressure, magnetic field or chemical substitution tunes the strength of the two competing forces. Such a phase transition happens at a quantum critical point. In the vicinity of this point usually the typical properties of a Fermi liquid are violated at least down to a rather low temperature and so-called non-Fermi-liquid behavior is found (see paragraph 1.5).

In uranium the $5f$-states are less localized than the $4f$-electrons as shown in figure 1.1c where you can see the effective radial charge density of the U atom compared to those of Ce and Nickel (Ni) 1.1b and a, the latter being a typical magnetic system with itinerant (delocalized) $3d$-electrons. We see that the f-state in uranium has a more itinerant character than in Ce and the $5f$-wave function is between atomic-like (as in Ce) and band-like (as the $3d$-state in Ni). As a consequence, magnetism in U compounds probably has a more itinerant character. In the dual model which is discussed, for example in UPd_2Al_3 (Zwicknagl et al. 2002), one of the three $5f$-electrons is delocalized and the

two other ones are localized. In general, uranium compounds with strong electronic correlations show a high complexity. Not only the unknown degree of itineracy but also the presence of several competing energy scales such as strong magnetic anisotropies, strongly hybridized crystal field excitations and soft lattice modes play a role.

There are some heavy fermion systems which show unconventional superconductivity (see paragraph 1.7), for example $CeCu_2Si_2$, UPt_3, URu_2Si_2 or UPd_2Al_3 (Pfleiderer 2009) or the ferromagnetic superconductors, for example UCoGe (Huy et al. 2007). It appears often in the proximity to a quantum critical point under pressure. Highly interesting phenomena like the coexistence of superconductivity with magnetic ordering, anisotropic gaps and coupling of Cooper pairs by magnetic or valence fluctuations need further investigation.

1.2 Fermi-liquid theory

Landau's concept of Fermi liquids was developed to describe the properties of liquid ^{3}He (Landau 1957; Leggett 1975). It takes into account interactions between the fermions. Electrons in a solid interact by Coulomb interaction. In heavy fermion systems, the interaction cannot be neglected like for example in the normal metal copper. In the Fermi-liquid theory the interacting electrons are described as weakly interacting fermionic quasiparticles. The interaction is taken into account by introducing an effective mass m^* in terms of Landau parameters (Enss and Hunklinger 2005). The quasiparticles are excitations of this N body system where the only difference to the excited states of free electrons is the renormalized effective mass. A simple image would be that, when an electric field is applied, the electrons cannot move easily or freely like in an electron gas because of their interaction with the other electrons which gives them a larger inertia and so a larger mass. In this theory the low temperature properties follow the following laws (Fulde 1995; Pines and Nozière 1966): The specific heat C divided by temperature is given as

$$\frac{C}{T} = \gamma_0 \frac{m^*}{m}. \tag{1.1}$$

γ_0 is the Sommerfeld coefficient for a free electron gas and m is the mass of the free electron. Taking into account spin fluctuations and phonons, extra terms βT^2 or $b_{sf} T^2 \log T/T_{sf}$ are calculated in itinerant heavy electron systems and the effective mass is given as $m^*/m = 1 + \lambda_{sf}$ (Doniach and Engelsberg 1966; Lonzarich 1997). Here, b_{sf}, λ_{sf} and T_{sf} are parameters of the model. They can be linked to specific antiferromagnetic or ferromagnetic interactions. Of course, usually a weak βT^2 term may reflect the phonon contribution.

The susceptibility χ is calculated as

$$\chi = \chi_0 \frac{m^*}{m} (1/(1 + F_0^a)) \tag{1.2}$$

where χ_0 is the value of a free electron gas and F_0^a is a Landau parameter. In first order this is a Pauli susceptibility proportional to m^*. In case of magnetic interactions in an itinerant heavy fermion system, for example ferromagnetic interactions, the susceptibility can be described as $\chi = S\chi_0 - aT^2$ in the simple case of a parabolic conduction band, where S is the Stoner factor (Béal-monod et al. 1968).

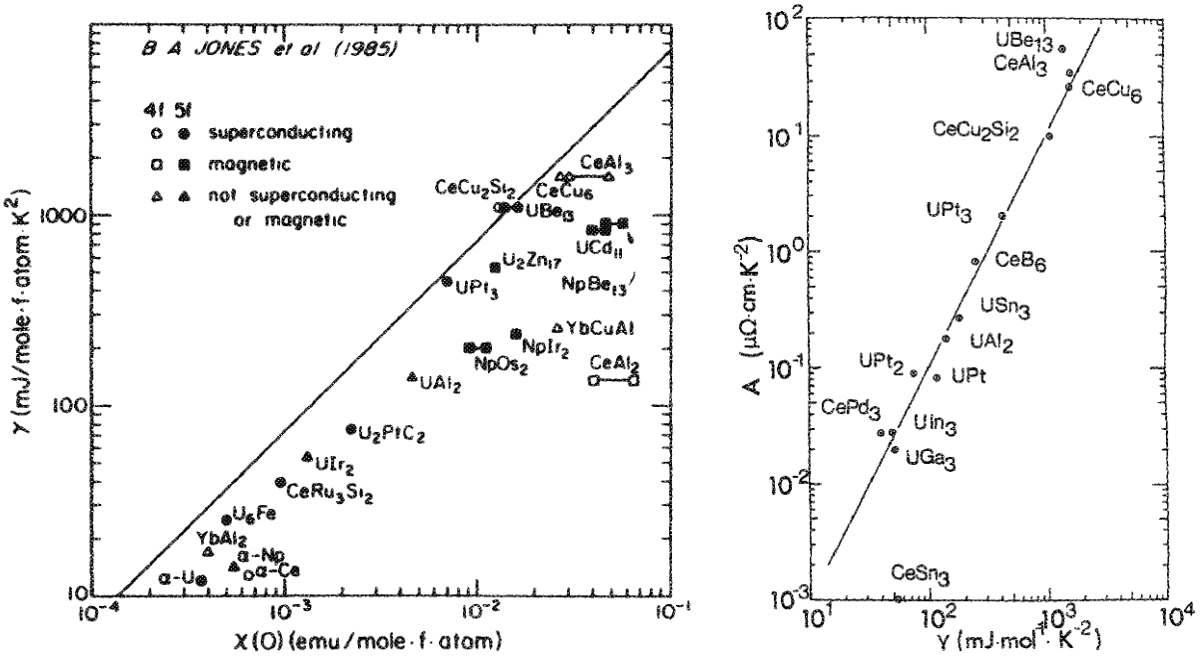

Fig. 1.2 : Left: Specific heat coefficient γ against the zero temperature susceptibility $\chi(0)$ for several heavy fermion compounds. The straight line corresponds to the theoretical value for free electrons (spin = 1/2, degeneracy N=2). Right: A coefficient of T^2 resistivity as a function of γ. The straight line corresponds to $A \propto \gamma^2$. (Auerbach and Levin 1987)

For $T \longrightarrow 0$ the susceptibility and the specific heat depend both on m^* which is proportional to the density of states on the Fermi surface $N(E_F)$. The so called Wilson ratio

$$R = \frac{\chi}{\gamma} \frac{\pi^2 k_B^2}{\mu_0 \mu_{eff}^2} \tag{1.3}$$

is therefore constant. The left graph in figure 1.2 illustrates the scaling of γ and χ for several heavy fermion systems. The ratio R is one for free electrons but between two (pure Kondo effect) and five for heavy fermion systems, depending on the degeneracy of the ground state (all the points lie below the straight line). The enhancement is due to the additional Landau parameter F_0^a in the susceptibility.

For the resistivity in Fermi-liquid theory we obtain

$$\rho = \rho_0 + AT^2. \tag{1.4}$$

with $A \propto m^{*2}$ if the local fluctuations dominate. The first term is due to scattering at impurities and defects and the second term is due to quasiparticle-quasiparticle scattering. Just as the Wilson ratio, a constant is also found for the ratio of $\sqrt{A}/\gamma$, called Kadowaki-Woods ratio (Kadowaki and Woods 1986). This is presented in the right graph of figure 1.2. Taking into account spin fluctuations, A will not be proportional to m^{*2}.

This shows that the majority of heavy fermion systems are well described by the Fermi liquid theory works well. This crude proportionality of χ, C/T and A to m^* and m^{*2} is roughly valid since in heavy fermions the spin dynamics and the mass enhancement are dominated by local fluctuations. By contrast in $3d$ itinerant magnetism where the phenomena occur around a given wavevector this proportionality is not observed.

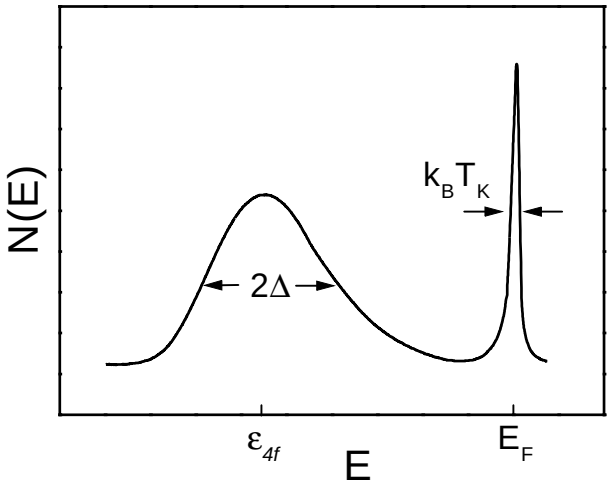

Fig. 1.3 : Schematic density of states of a heavy fermion system. The $4f$-level with a width 2Δ is localized with a distance of $\epsilon_{4f} \approx 2$ eV from the Fermi energy E_F. In the Kondo model a maximum (Kondo resonance) develops in the density of states near the Fermi energy due to hybridization. The Coulomb repulsion against one electron more in the $4f$-level is ~ 5 eV (Bauer 2007).

1.3 Kondo effect versus RKKY interaction

Kondo effect

The signature of the Kondo effect is a minimum in resistivity of metals with dilute magnetic impurities, that means that the resistivity rises again when lowering the temperature (see figure 1.4). This behavior was first explained by Kondo (Kondo 1964), who introduced the perturbation term

$$H_K = -2J\ \boldsymbol{S} \cdot \boldsymbol{s} \tag{1.5}$$

into his Hamiltonian. It describes the scattering of conduction electrons with spin $\boldsymbol{s}$ off a local moment $\boldsymbol{S}$ of the impurity. J is the exchange integral of the attributed spin wave functions. The interaction is antiferromagnetic and owing to higher order processes the spins of the conduction electrons form a screening cloud around the local moment. At low temperature the hybridization V of conduction electrons with the d or f-electrons responsible for the local moment $\boldsymbol{S}$ leads to a peak in the density of states at the Fermi level called Kondo resonance or Abrikosov-Suhl resonance (see figure 1.3). This peak develops to compensate the loss of degrees of freedom of the spin and the orbital moment of the conduction electrons and it has a width of $\sim k_B T_K$. It is this large density of states which leads to the enhanced effective mass in heavy fermion compounds.

In the ground state the spin $\boldsymbol{S}(\uparrow)$ and the spin $\boldsymbol{s}(\downarrow)$ form a non-magnetic bound singlet many body state $\{\boldsymbol{S}(\uparrow) \cdot \boldsymbol{s}(\downarrow) \pm \boldsymbol{S}(\downarrow) \cdot \boldsymbol{s}(\uparrow)\}$ with a binding energy

$$k_B T_K \propto D \exp(-\frac{1}{N(E_F)J}) \tag{1.6}$$

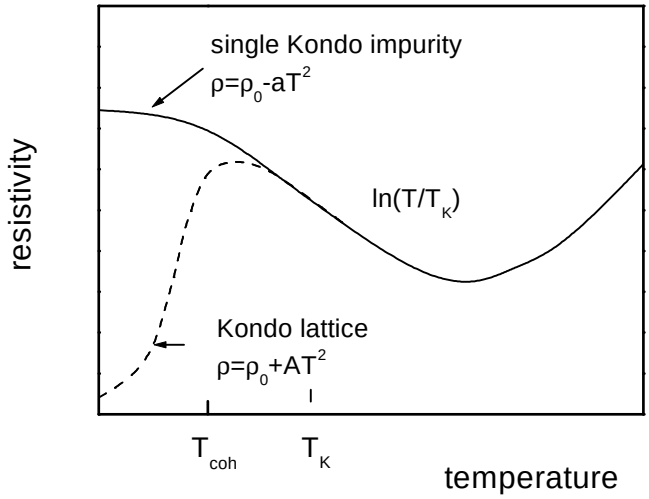

Fig. 1.4 : Temperature dependence of resistivity of a metal with the Kondo effect.

$N(E_F)$ is the number of charge carriers at the Fermi surface and D is linked to the width of the virtual bound state of the magnetic impurity.

Just above the Kondo-temperature T_K, the resistivity of a metal with magnetic impurities rises when lowering the temperature (see figure 1.4) according to the following equation

$$\rho \propto -ln(\frac{T}{T_K}). \tag{1.7}$$

Remarkably in heavy fermion systems where the magnetic "impurities" i.e. the moments of the f-electrons, are present on every cerium-lattice site, the Ce f-electrons behave just above the Kondo-temperature like diluted magnetic moments in spite of their periodicity. Only at a lower temperature T_{coh} do coherence effects start to play a role and the correlations between impurity spins and spins of conduction electrons become important on an extended length scale. Below this temperature Bloch-waves develop and a band of quasiparticles is formed. In these Kondo lattices the resistivity drops strongly due to coherent scattering and follows at low temperature a Fermi-liquid behavior (dashed line).

RKKY interaction

The wave functions of f-electrons are well localized and therefore the corresponding moments cannot interact directly with each other. But the spin polarized screening cloud of conduction electrons described above has a longer range and can mediate indirectly an interaction between two local moments. This so-called Rudermann, Kittel, Kasuya, Yosida (RKKY) interaction extends over a long range and is damped with a sinusoidal oscillation of wave vector k_F (Rudermann and Kittel 1954). Depending on the distance between the magnetic moments $\boldsymbol{S_i}$ and $\boldsymbol{S_j}$ it can be ferro- or antiferromagnetic. The associated energy is:

$$k_B T_{RKKY} = J^2 N(E_F) \frac{\cos(k_F r)}{(k_F r)^3} \tag{1.8}$$

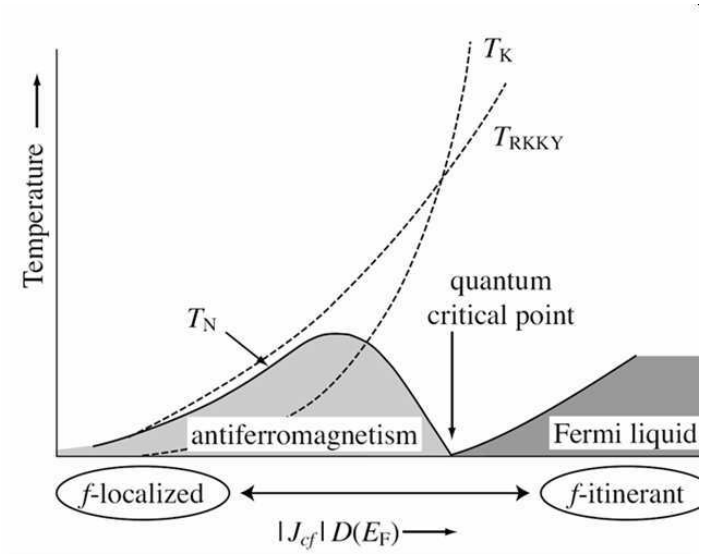

Fig. 1.5 : The Doniach phase diagram shows the competition between the energies associated to the Kondo effect T_K and the RKKY interaction T_{RKKY} as a function of $JD(E_F)$ (corresponds to $JN(E_F)$ in the text) and the corresponding ordering temperature T_N (Brandt and Moschalkov 1984).

Competition of Kondo effect and RKKY interaction

Kondo interaction and RKKY interaction both depend on the exchange J between the conduction electrons and the f-electrons. The system will take the ground state with the lower energy. If the RKKY interaction is stronger, this will be a magnetic ground state but if the Kondo interaction is stronger it will be a non-magnetic one. The competition of those two interactions was first studied by Doniach (Doniach 1977). In the Doniach diagram (see figure 1.5) the energies attributed to these two interactions are drawn as a function of $JN(E_F)$. Heavy fermion systems are systems with a value of $JN(E_F)$ for which the associated energies k_BT_K and k_BT_{RKKY} have a similar value. By varying J, the system can be tuned from a magnetic to a non-magnetic system by passing a quantum critical point. This is a transition point at zero temperature where the ground state of the system passes from one quantum state to another driven by an external parameter other than temperature.

A possible parameter to tune the system through a quantum critical point is pressure. When pressure is applied, the lattice parameters change and therefore the exchange integral between the conduction electron and the f-electron wave function. In the density of states schematically presented in figure 1.3 the width of the virtual $4f$ bound state is defined as 2Δ and its distance to the Fermi level E_F is ϵ_{4f} where the Kondo resonance is located. In case of strong Coulomb repulsion within the f-orbital ($\mathrm{U}\longrightarrow\infty$) the exchange J, the hybridization matrix element V and the width Δ fulfill the relations (Flouquet 2005):

$$JN(E_F) \approx \frac{\Delta}{\epsilon_{4f}} \qquad \Rightarrow \qquad J = \frac{V^2}{\epsilon_{4f}} \tag{1.9}$$

as $\Delta = V^2\mathrm{N}(\mathrm{E}_F)$. Under pressure the f-level becomes wider and its energy level can

also change. With a larger Δ and smaller ϵ_{4f} (in case of Ce) the hybridization and the exchange increase. This tunes the two competing forces and the system moves across the Doniach diagram. Nowadays, different theoretical models for quantum critical points exist (for a review see (Coleman et al. 2001)), but as the compounds studied here are not typical quantum critical systems like the Ce 115 compounds or $YbRh_2Si_2$, we will not go into detail.

Uranium as a free neutral atom has the electron configuration $[Rn]5f^36d^17s^2$. In a solid the most usual ions are U^{3+} with the configuration $[Rn]5f^3$ or U^{4+} with the configuration $[Rn]5f^2$. Both of these states are magnetic. Therefore, the Doniach picture cannot easily be applied for uranium compounds. The magnetic moments calculated by Hund's rules are never found in uranium compounds, because of the partial delocalization of the $5f$-electrons. The delocalized f-electrons form bands and cannot contribute to the stable local moment. Under pressure the hybridization increases between the f-electrons and the conduction band and therefore the occupation of the f-level decreases and the local moment gets lost even without the Kondo effect (Sheng and Cooper 1994). This effect competes with the increase of the RKKY interaction due to increase of the hybridization.

1.4 Intermediate valence

Heavy fermion systems have only a small hybridization between the f-electrons and the conduction electrons. As seen in figure 1.3 the f level is well separated from the Kondo resonance at the Fermi level. In intermediate valence (IV) systems the hybridization becomes stronger and the $4f$-level width increases (Wachter 1993). Additionally, the Kondo resonance is also broad due to high Kondo temperatures. Therefore, there is a strong mixing between f-electrons and the conduction electrons, i.e. the levels are not well separated any more. The occupation number of the f-level n_f is not near 1, but clearly intermediate ($n_f < 0.9$). In Ce IV systems, the crystal field levels are not well defined, their f atomic character is lost. In Yb IV systems, due to the sharpness of the $4f$-level, crystal field effects can be observed even inside the IV regime.

In the case of U atoms, the valence fluctuations occur between the U^{3+} ($5f^3$ configuration) and U^{4+} ($5f^2$ configuration). Under pressure, the occupation number n_{5f^2} will increase reaching a critical value where the magnetic properties seem renormalized to the $5f^2$ configuration even if the valence is not 4. For the $4f$ electrons, a well known comparable example is Tm with a fluctuation between two magnetic configurations Tm^{3+} and Tm^{4+} (Derr et al. 1989).

1.5 Non-Fermi-liquid behavior

In proximity to a quantum critical phase transition heavy fermion systems often exhibit strong deviations from Fermi-liquid theory. One scenario is that this is due to strong spin fluctuations or valence fluctuations (Lonzarich 1997; Millis 1993; Watanabe and Miyake). As a typical example we present the pressure-phase diagram around a quantum critical point for $CeIn_3$ in figure 1.6. For low pressure $p < p_c$ the system is magnetically ordered. One possible theory which explains the phase diagram is based on spin fluctuations. In

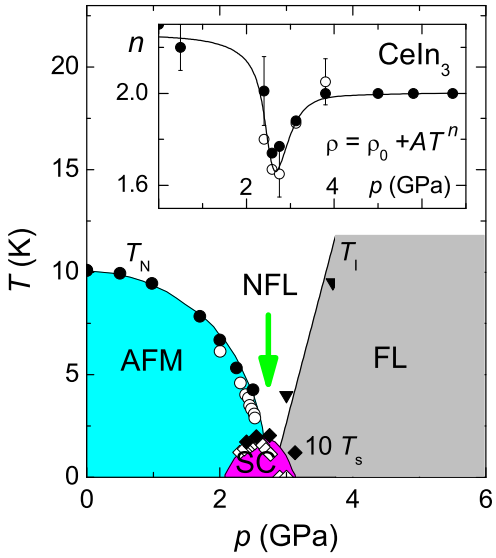

Fig. 1.6 : Pressure-temperature phase diagram around a quantum critical point for $CeIn_3$. The inlay shows the pressure dependence of the exponent n of a $\rho = \rho_0 + AT^n$ fit. (Knebel et al. 2002)

		C/T	$\rho \sim T^n$
F	3d	$-lnT$	$T^{\frac{5}{3}}$
	2d	$T^{-\frac{1}{3}}$	$T^{\frac{4}{3}}$
AF	3d	$T^{\frac{1}{2}}$	$T^{\frac{3}{2}}$
	2d	$-lnT$	T

Table 1.1: Temperature variation of C/T and ρ in the non-Fermi-liquid regime (Flouquet 2005).

this theory, coming close to the quantum critical point at p_c the spin fluctuations become stronger and stronger and the associated energy T_{sf} becomes larger. If the transition is of second order the spin correlation length ξ_s diverges at the quantum critical point. The characteristic spin fluctuation time τ_s is related to ξ_s via the critical exponent z as $\tau_s \sim \xi_s^{-z}$. At the quantum critical point the temperature T_N vanishes. In this fluctuation dominated region non-Fermi-liquid behavior is found. For two and three dimensional spin fluctuations in a ferro- (F) or antiferromagnet (AF) the temperature dependence of resistivity ρ and specific heat C/T is given in table 1.5. The exponent n of the temperature behavior of resistivity $\rho = \rho_0 + AT^n$ as a function of pressure for $CeIn_3$ is shown in the inlay of figure 1.6. It is smaller than two near the quantum critical point but equal to two for higher pressures. On this side of the quantum critical point the system recovers a Fermi-liquid behavior.

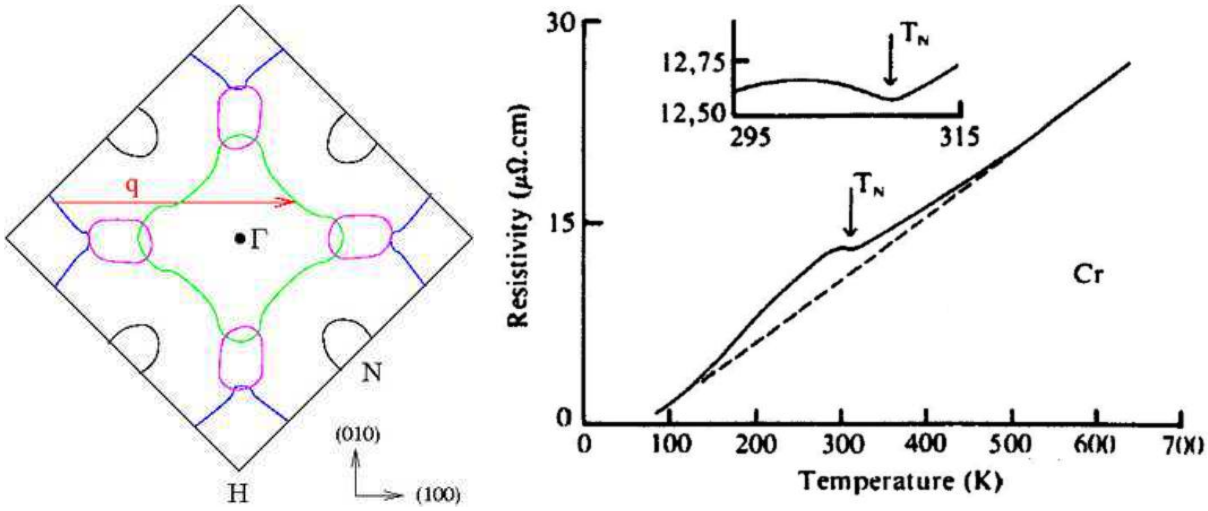

Fig. 1.7 : Left side: A sketch in k-space of a (0, 0, 1) section of the Fermi surface of Cr (Fry et al. 1980). The band structure of Cr yields an electron pocket (green) centered at Γ and a hole pocket (blue) centered at H. The surrounding black square represents the first Brillouin zone boundary. Right side: The typical nesting shape in the resistivity of chromium. (Bridgman 1932; Marcinkowski and Lipsitt 1961) and references therein.

1.6 Spin density wave order

The spin density wave state is an itinerant antiferromagnetic ground state. It often occurs in low dimensional or highly anisotropic systems. The most famous representative of systems with this ground state is chromium (Cr) (for an review see (Fawcett 1988; Fawcett et al. 1994)). On the left side of figure 1.7 is sketched the Fermi surface of chromium in k-space perpendicular to the (0, 0, 1) direction. The band structure of Cr shows an electron pocket (green) centered at Γ and a hole pocket (blue) centered at H. The boundaries of these two kinds of pockets have large parallel regions that match when shifted by the nesting wavevector q (red). If this nesting is possible, the electrons and holes condensate into the spin density wave state with a sinusoidal or helical variation of the spin density. The charge density meanwhile stays constant implying an opposite variation of the density of fermions with spin up and spin down. The energy gain for the condensate is $\Delta N(E)$ with the gap Δ which opens on the relevant part of the Fermi surface. The gap opening leads to a loss of carrier density and therefore firstly to an increase in the resistivity curve below the Neel temperature T_N (see figure 1.7 on the right) and secondly to an exponential decay in resistivity and specific heat. If q is a rational multiple of the lattice constant a the spin density wave is said to be commensurate, otherwise it is incommensurate. The real space periodicity of the resulting spin density wave is given by $2\pi/q$. The spin density wave state is an antiferromagnetic ground state. The typical nesting anomaly of the resistivity at the phase transition is different from the signature of a transition to local antiferromagnetism. As an example for the signature of an antiferromagnetic transition without nesting, figure 1.8 shows data for UIr_2Si_2, another example out of the same class of compounds with UT_2Si_2 structure (T is a transition metal). Here the resistivity has a downward kink at T_N and its derivative is similar to the specific heat.

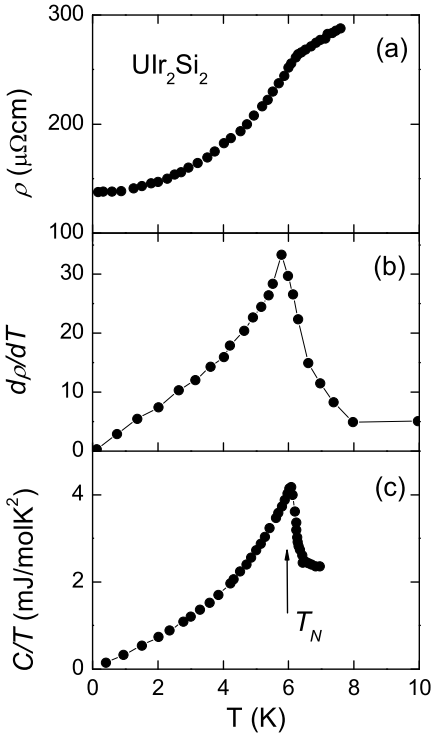

Fig. 1.8 : Temperature dependence of resistivity (a), derivative of resistivity (b) and specific heat (c) of UIr_2Si_2 (Verniere et al. 1995, 1996). Lines are guides to the eye.

The spin density wave ground state is found in many strongly correlated electron systems. The highly one dimensional organic superconductors (Jerome et al. 1980; Kwak 1983) present perfect nesting conditions. The new iron based superconductors are quasi two dimensional and also present good conditions for nesting (Yao and Carlson 2008).

1.7 Unconventional superconductivity

Heavy fermion superconductivity appears usually at a transition temperature $T_{sc} \leq 2$ K. Below this temperature the heavy quasiparticles form Cooper pairs and condense. The fact that quasiparticles and not light electrons take part in the condensation process can be seen from the size of the jump in specific heat $\Delta C \sim \gamma T_{sc}$ which is large due to the enhanced effective mass $\gamma \propto m^*$. Another surprising feature is that the superconductivity occurs even in presence of magnetic ordering or near a quantum critical point. In classical BCS theory with s-wave pairing magnetic impurities destroy superconductivity because the Cooper pair electrons have opposed spin and propagation vector k. Due to the strong Coulomb repulsion in strongly correlated materials however, it is possible to find Cooper pairs with total spin S = 1, 3... i.e. the Cooper pair wave function is not an *s*-wave but a *p*- or *d*-wave. This is probably the case in ferromagnetic superconductors described in the next paragraph.

In heavy fermion systems, superconductivity is often found in proximity to a quantum

phase transition (Mathur et al. 1998). There are many theories which estimate that the magnetic fluctuations mediate the attraction between the members of a Cooper pair and not phonons as in BCS theory. One definition of unconventional superconductivity is that is has a lower symmetry than the lattice. For both conventional and unconventional superconductivity the order parameter can vanish on lines or points on the Fermi surface but in unconventional superconductivity the order parameter changes its sign at these points. In these special directions there is no gap and as a consequence no exponential temperature dependence of physical properties below the transition but simple power laws. The slope of the critical field $\mu_0 H_{c_2}$ (the external magnetic-field where superconductivity is suppressed by field and temperature) for $T \longrightarrow T_{sc}$ is given as

$$\left.\frac{\partial \mu_0 H_{c_2}}{\partial T}\right|_{T=T_{sc}} \propto m^{*2} T_{sc} \tag{1.10}$$

The value and temperature dependence of the critical field $\mu_0 H_{c_2}$ are determined from two mechanisms:

- Orbital pair breaking: the Cooper electrons move in a magnetic field and are exposed to the Lorentz force which tends to separate the pair. As a result, the transition temperature is decreased. This is the limiting mechanism near T_{sc}.

- Pauli limiting: In a conventional singlet BCS superconductor the spins of the Cooper electrons are opposed. Applying a magnetic field tends to align them and will break the pair. This also reduces the transition temperature in field. It is not present in simple triplet states with S=1 and L=1, 3, ...

Ferromagnetic superconductors

Since 2000, four materials have been discovered, where ferromagnetism and superconductivity coexist and are carried by the same electrons, UGe_2, URhGe and UCoGe and UIr. We will restrain our considerations to the first three ones which have an orthorhombic crystal symmetry. The superconductivity in these compounds can be understood as triplet superconductivity, similar to the superfluid phases in ^{3}He (Osheroff et al. 1972). It is mediated by spin fluctuations near the critical point (Fay and Appel 1980).

In a ferromagnetic superconductor, the up and down spin bands are split, and the pairing occurs within the bands to equal spin Copper pairs $|\uparrow\uparrow\rangle$ and $|\downarrow\downarrow\rangle$ or between the bands $|\uparrow\downarrow + \downarrow\uparrow\rangle$. If the splitting is big enough, the third term can be neglected. Ferromagnetic superconductors are principally two-band superconductors (Fay and Appel 1980). As the critical temperature depends on the density of states (or effective mass), each band has a different transition temperature T_{sc}. However, the precise band structure can lead to a case with only one superconducting band.

Symmetry considerations can improve the understanding of the superconducting phase in ferromagnetic superconductors. In a paramagnetic metal, the superconducting state breaks only the gauge theory and the crystal symmetry. In this case in the absence of a field, the superconducting transition temperatures are the same. In a ferromagnetic metal, additionally the time reversal symmetry is broken. In uniaxial ferromagnets with orthorhombic crystal symmetry, the allowed superconducting gap functions have been

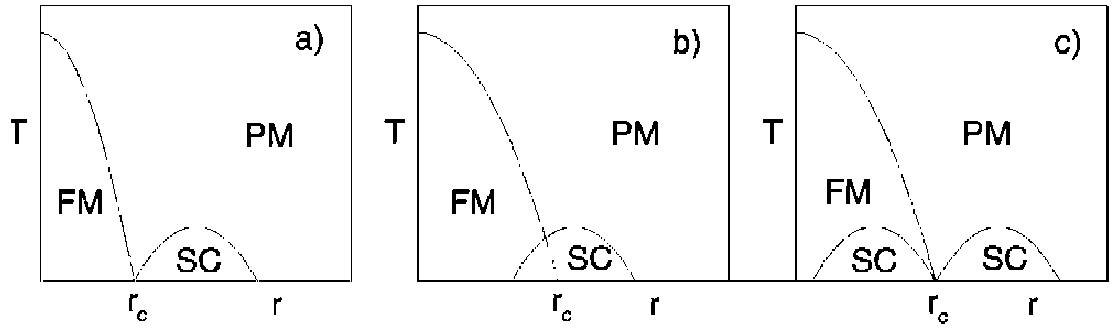

Fig. 1.9 : Three scenarios for spin triplet superconductivity near a second order critical point of a weak ferromagnet (Fay and Appel 1980; Roussev and Millis 2001).

determined (Mineev 2009; Mineev and Champel 2004). For an ordered moment along the c axis, the superconducting gap can either have zeros (nodes) parallel to this axis ($k_x = k_y = 0$) or a line of zeros in the $k_x k_y$ plane.

The phase diagram of weak ferromagnetic superconductors at a second order critical point has been treated by several theorists (Fay and Appel 1980; Kirkpatrick and Belitz 2003; Roussev and Millis 2001). As figure 1.9 shows, three basic scenarios are possible. Fay and Appel predict a superconducting dome on both sides of the critical point, but the critical temperature is zero at the critical point (scenario c) in figure 1.9) (Fay and Appel 1980). Taking into account the existence of magnons in the ferromagnetic state, this can lead to a strong increase of T_{sc} for the dome within the ferromagnetic phase (Kirkpatrick and Belitz 2003). In UGe_2 for example, the transition temperatures within the ferromagnetic state are detectable, whereas in the paramagnetic state, no superconductivity was detected in the achievable measurement range. In the scenario b) proposed by Roussev and Millis (2001), the transition temperature does not vanish at the critical point. This gives the possibility of an extension of the superconducting state in the paramagnetic state. Scenario a) is a more "classical" scenario, where the superconductivity does not extend into the ferromagnetic phase.

The pressure-phase diagrams of the real materials UGe_2 and URhGe are shown in figure 1.10. In UGe_2, the Curie temperature is $T_{Curie} = 53\,\mathrm{K}$ and superconductivity is induced by pressure in a window between 1 GPa and the critical pressure 1.5 GPa with the maximum T_{sc} of around 0.7 K (Saxena et al. 2000). The superconducting phase lies completely inside the ferromagnetic phase. But the situation is more complicated: There is a transition between two ferromagnetic phases FM1 and FM2 with different ordered magnetic moment and superconductivity seems to be related to this transition as the maximum T_{sc} appears precisely at the pressure, where the system switches from FM2 to FM1 (Pfleiderer and Huxley 2002). It is not possible to apply the theories mentioned above, because the ferromagnetic transition becomes first order near the critical pressure.

URhGe is both ferromagnetic ($T_{Curie} = 9\,\mathrm{K}$) and superconducting ($T_{sc} = 0.25\,\mathrm{K}$) at ambient pressure (Aoki et al. 2001). Applying pressure, the system moves away from the critical point. An almost linear increase of T_{Curie} with a slope of $\frac{dT_{Curie}}{dP} = +0.65$ K/GPa up to 12 GPa (Hardy et al. 2005) is observed under pressure but the superconducting transition temperature decreases. Additionally, a spectacular reentrance of superconductivity appears close to a transition under high magnetic fields, where a reorientation of

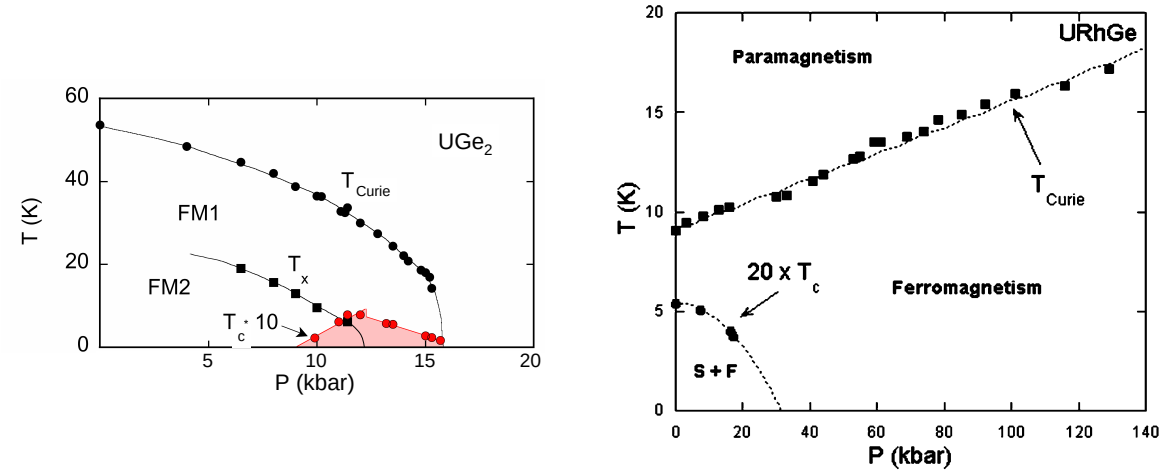

Fig. 1.10 : Pressure temperature phase diagrams of UGe_2 (left side (Pfleiderer and Huxley 2002; Saxena et al. 2000)) and URhGe (right side (Hardy et al. 2005)).

the magnetic moments takes place (Levy et al. 2005). It has been shown by experiment that the reentrant superconductivity is directly connected with the strong enhancement of the effective mass at this reorientation transition (Miyake et al. 2008). The analysis of the superconducting critical field clearly shows that triplet superconductivity is realized (Hardy et al. 2005).

UCoGe is a recently discovered compound with $T_{Curie} = 3\,\mathrm{K}$ and $T_{sc} = 0.6\,\mathrm{K}$ (Huy et al. 2007). Thermodynamic measurements indicate that the critical pressure should be around 1 GPa and thus easily attainable. This compound will be examined closely in chapter 4, especially the pressure-temperature phase diagram.

1.8 Quantum oscillations

Quantum oscillations are a powerful tool to investigate the Fermi surface of a metal (Shoenberg 1984). The theory of the de Haas-van Alphen (dHvA) effect, which describes the oscillations in magnetization was first described by Lifshitz and Kosevich (Lifshitz and Kosevitch 1956). In this study, I measured the Shubnikov-de Haas (SdH) effect, i.e. oscillations of the electric conductivity. In this paragraph, the underlying theory will be explained with emphasis on the effects which appear in URu_2Si_2.

1.8.1 Metals in magnetic fields

Quasi free electrons with effective cyclotron mass $m_{eff} = m^\star \cdot m_e$ in a homogeneous vector potential $\vec{B} = \vec{\nabla} \times \vec{A}$ with vector potential $\vec{A}$ can be described by the Hamiltonian

$$\mathbf{H}\Psi = \frac{1}{2m_{eff}}(\frac{\hbar}{i} - e\vec{A})^2\Psi = \mathbf{E}\Psi$$

For a magnetic field in z-direction, the movement of the electrons is quantized in the k_x, k_y plane and therefore they move along helical trajectories on cylinders called Landau

tubes with the cyclotron frequency

$$\omega_c = \frac{e}{m_{eff}} B. \tag{1.11}$$

Only Landau tubes with an energy below the Fermi energy are populated at zero temperature. With the variation of the magnetic field, the cross sectional area of the Landau tubes varies and the change of the degeneracy creates a change of the population of the different tubes. When a Landau cylinder crosses the Fermi level the density of states at the Fermi level increases. This change of the density of states causes variations of many physical properties with a periodicity of $\Delta(\frac{1}{B})$. The oscillation frequency F is proportional to the extremal cross sectional area S of the Fermi surface perpendicular to the magnetic field:

$$F_i = \frac{1}{\Delta(\frac{1}{B})_i} = \frac{\hbar}{2\pi e} S_i$$

The Fermi surface can contain several sheets, giving several frequencies, and the warping of one sheet can also give several frequencies per Fermi surface sheet.

1.8.2 The Lifshitz-Kosevich theory

The oscillatory part of the magnetization $\widetilde{M}$ in the Lifshitz Kosevich theory is given by the derivative of the oscillatory part of the chemical potential $\widetilde{\Omega}$ as (Lifshitz and Kosevitch 1956)

$$\widetilde{M} = \frac{\partial \widetilde{\Omega}}{\partial B} = \sum_p \sum_i \frac{1}{p^{3/2}} A_i \sin\left(\frac{2\pi p F_i}{B} + \phi_i\right) \tag{1.12}$$

$$A_i \propto B^{1/2} \left| \frac{\partial^2 S_i}{\partial k^2} \right|^{-1/2} R_T R_D R_S \tag{1.13}$$

$$R_T = \frac{\alpha p m_i^\star T/B}{\sinh(\alpha p m_i^\star T/B)} \tag{1.14}$$

$$R_D = \exp(-\alpha p m_i^\star T_D/B) \tag{1.15}$$

$$R_S = \cos(\pi g_i p m_i^\star / 2m_0) \tag{1.16}$$

$$\alpha = 2\pi^2 k_B m_e / e\hbar \approx 14.69\,\mathrm{T/K} \tag{1.17}$$

Here R_T, R_D and R_S are damping factors explained below, p is the number of the harmonic.

The curvature factor

The higher the curvature of the Fermi surface $\left|\frac{\partial^2 S_i}{\partial k^2}\right|$, the more Landau cylinders cut the Fermi surface. In this case, the depopulation of the levels is almost continuous with increasing field and the number of electrons at the Fermi energy is almost constant. This leads to a strong damping of the oscillation amplitude. On the other hand for a long ellipsoidal Fermi surface, in e.g. Bismuth or in quasi two dimensional systems with a cylindrical Fermi surface with the field parallel to the symmetry axis, the curvature is small and the oscillations become very big.

Damping due to finite temperature

R_T is the damping factor due to finite temperature. Finite temperature leads to a broadening of the Fermi edge and this leads to a damping of the quantum oscillations. From the temperature dependence of the amplitude for a fixed field range, we can determine the effective cyclotron mass. For a given field range from B_{min} to B_{max} with average field B_{eff} of the inverse field scale $\frac{1}{B_{eff}} = \frac{1}{2}\left(\frac{1}{B_{min}} - \frac{1}{B_{max}}\right)$ the amplitude is given as

$$A_p(T) = A_0 \cdot \frac{pT/B_{eff}}{\sinh(\alpha p m^\star T/B_{eff})} \tag{1.18}$$

The amplitudes can be obtained from Fourier transforms in the fixed field range and $m^\star$ is obtained directly from a fit. Another possibility is to use the relation $\sinh x = \frac{1}{2}(exp(x) - exp(-x))$ to obtain

$$\ln\left(\frac{A_P(T)}{T}(1 - \exp(-2\alpha p m^\star T/B_{eff}))\right) = -\frac{\alpha p m^\star}{B_{eff}}T \tag{1.19}$$

In this case the left hand side is plotted against T and $m^\star$ is obtained from the slope of the straight line by an iterative plotting in the so-called mass plot.

From the effective cyclotron mass $m^\star$ and the cross sectional area S_F the Sommerfeld coefficient γ can be estimated, under the assumption that the Fermi surface is spherical. In this case $S_F = \pi k_F^2$ and $E_F = \hbar^2 k_F^2/2m^\star$. As a function of the density of states $D(E_F)$, γ is expressed as

$$\gamma = \frac{\pi^2}{3}k_B^2 D(E_F) \tag{1.20}$$

$$= \frac{\pi^2}{3}k_b^2\frac{V}{2\pi^2}\left(\frac{2m^\star}{\hbar^2}\right)^{3/2}E_F^{1/2} \tag{1.21}$$

$$= \frac{k_b^2 V}{3\hbar^2}m^\star k_F \tag{1.22}$$

where V is the molar volume.

Damping due to impurity scattering

The influence of impurity scattering or other effects reducing the lifetime τ of the quasiparticles is taken into account by the Dingle factor R_D. Dingle showed (Dingle 1952) that the broadening of the Fermi level caused by this scattering acts like an additional temperature, the Dingle temperature

$$T_D = \frac{\hbar}{2\pi k_B \tau},$$

assuming that the lifetime does not depend on energy. The field dependence of the oscillation amplitude at fixed temperature T gives us the Dingle temperature according to the formula

$$A_p(B) = A_{p,0} \cdot \frac{TB^{-1/2}R_D(p)}{\sinh(\alpha p m^\star T/B)}. \tag{1.23}$$

This is equivalent to

$$\ln(A_p(B)B^{1/2}\sinh(\alpha p m^\star T/B)) = -\alpha p T_D 1/B. \tag{1.24}$$

Plotting the left hand side against $1/B$, a straight line is obtained and its slope $-\alpha p T_D$ gives the Dingle temperature. Here, the cyclotron mass must be already known. Its uncertainty induces a large uncertainty on the Dingle temperature. In order to avoid this, the Dingle reduction factor can be rewritten as

$$R_D = \exp(-\pi p r_c/l_0) \tag{1.25}$$

Here, $r_c = \frac{m^\star v_F}{eB} = \frac{\hbar k_F}{eB}$ is the radius of the cyclotron motion and l_0 the mean free path of the electrons.

Spin splitting factor

The last factor R_S describes the damping due to the lifting of the quasiparticle spin degeneracy by a magnetic field. The spin up and spin down energy levels are split in a magnetic field creating Fermi surfaces with different size and a polarization of the bands (Pauli susceptibility). The dHvA signal is a superposition of the signals from the two Fermi surfaces

$$\widetilde{M}(T) \propto a_\uparrow(T)\sin(\frac{F_\uparrow(B)}{B} + \phi_0) + a_\downarrow(T)\sin(\frac{F_\downarrow(B)}{B} + \phi_0) \tag{1.26}$$

where $a_\uparrow$ and $a_\downarrow$ are the spin dependent amplitudes:

$$a_\uparrow = \frac{1}{m_\uparrow} R_{D\uparrow} R_{S\uparrow} \qquad a_\downarrow = \frac{1}{m_\downarrow} R_{D\downarrow} R_{S\downarrow}.$$

The phase is constant and spin independent. The observed frequencies $F_{obs,\sigma}(B_1)$ for $\sigma = \uparrow$ or $\downarrow$ are given as

$$F_{obs,\sigma} = F_\sigma(B_1) - B_1 \frac{\partial F_\sigma(B_1)}{\partial B} \tag{1.27}$$

Figure 1.11 shows that for a simple linear Zeeman splitting, the observed frequencies for both Fermi surfaces are the same and equal to the unsplit frequency in zero field (a), whereas in the case of non-linear splitting due to spin-orbit interaction the observed frequencies are split (b).

In the linear case with the assumption that the amplitudes of $\uparrow$ and $\downarrow$ are equal, the introduction of $F_\sigma(B)$ from 1.27 into 1.26 leads to a phase shift ϕ_S between the oscillations coming from the two Fermi surfaces and therefore to a reduction of the amplitude by $R_D = \cos\phi_S$ and here $\phi_S = \frac{\pi p g m_{eff}}{2m_e}$ with the Landé factor g. For free electrons $g = 2$, but the value for g can be modified by spin-orbit interaction.

1.8.3 Shubnikov-de Haas effect

Oscillations in the resistivity, also called Shubnikov-de Haas effect, are complicated to calculate because all scattering mechanisms have to be considered (Shoenberg 1984). Pippard (Pippard 1965a,b) simplified the understanding of the effect by assuming that

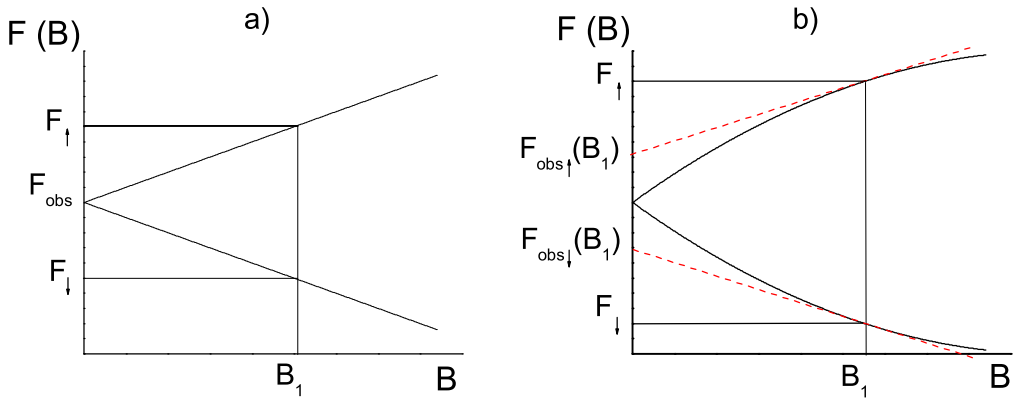

Fig. 1.11 : a) Linear splitting of the spin up and spin down bands in field b) A non-linear field dependence a splitting of the oscillations can be observed.

the scattering probability is proportional to the number of states into which the electrons can be scattered and therefore to the density of states $\widetilde{N}(E_F)$ at the Fermi level. Since

$$\widetilde{N} \propto \frac{\partial^2 \widetilde{\Omega}}{(\partial B)^2} \propto B^2 \frac{\partial \widetilde{M}}{(\partial B)}$$

$$\frac{\widetilde{\sigma}}{\sigma_0} \propto \frac{\widetilde{N}}{N_0}$$

where N_0 is the total density of states. The oscillatory behavior is the same as for $\widetilde{M}$, including the factors R_T, R_D and R_S. The relative size of the oscillations can be estimated, when ignoring R_D and R_S to

$$\frac{\widetilde{\sigma}}{\sigma_0} \approx \left(\frac{B}{F}\right)^{1/2}.$$

In normal metals this is very small, but it can become huge for semi metals such as bismuth, which have a much higher value for $\frac{B}{F}$ because of the low carrier density.

1.8.4 Limits of the Lifshitz-Kosevich theory

If the magnetization M in the sample by the applied magnetic field becomes strong, the field inside the sample is not equal to the field of the magnet. This induces a feedback on the oscillations and the effect is called magnetic interaction. With increasing magnetic interactions the shape of the oscillations in magnetization changes to a saw tooth curve with the peaks to the low field side. Therefore, the harmonic content increases a lot compared to the standard Lifshitz Kosevich theory. Due to the change in the thermodynamic potential in this case, the Shubnikov-de Haas oscillations become peaked on the top. In extreme cases of magnetic interaction, the SdH oscillations diverge and show singularities instead of peaks.

In the Lifshitz Kosevich theory, the Fermi energy is assumed to be constant. For high F/B this can be shown to be a reasonable assumption (Shoenberg 1984). In semimetals

however or near the quantum limit, i.e. when F/B becomes small, or also in two dimensional systems, the Fermi energy sticks to the outer Landau tube and can no longer be treated as constant. In this case, the variation of the Fermi energy can also cause a different shape of the oscillations.

Chapter 2

Experimental methods

2.1 Preparation and characterization of the single crystals

Sample quality plays a crucial role in material physics and most notably in uranium compounds where metallurgical effects can completely change the sample properties. Owing to this, a careful choice of sample is fundamental for a successful experiment.

The single crystals studied in this work were grown by Dai Aoki and Valentin Taufour in CEA Grenoble (Aoki et al. 2010). The basic materials had a very high purity: depleted uranium 99.9 %, Ruthenium 99.99 % and Silicon 99.9999 % for URu_2Si_2. Firstly, these materials are melted in stoichiometric proportions (U:Ru:Si = 1:2:2 or U:Co:Ge = 1:1:1). The melting temperature is not measured, but estimated to be $T_m \approx 1800\,\mathrm{K}$ for URu_2Si_2 (lower for UCoGe). The ingredients are melted and turned five times in a tetra arc furnace in a water cooled copper melting crucible. Moreover the melting is done under purified Argon atmosphere to avoid UO_2 being formed. It's not possible to work in vacuum because all the Silicon would volatilize.

Using x-ray scattering, the structure of the polycrystalline samples is tested and no parasitic phases could be found. The monocrystal is pulled by the Czochralski method in the same cleaned tetra-arc furnace (see the left hand side of figure 2.1). For this the polycrystal is put on a cooled copper plate in the furnace which is first cleaned and evacuated to an ultra high vacuum in order to clean the furnace. Then again under pure Argon atmosphere of a pressure of about 1 atm the sample is melted by four Argon arcs. An oriented mono crystalline seed crystal is dipped into the liquid and pulled at about 5 mm per hour. For URu_2Si_2 the pulling direction was along the crystalline c axis. A rotation of about 20 turns per minute homogenizes the temperature. The single crystal can have a diameter of about 5 mm and a length of several centimeters (see the right hand side of figure 2.1).

The samples are cut by electro erosion. High quality URu_2Si_2 samples are usually smaller than 1 mm. The dimension of the biggest used UCoGe sample was around 4 mm. The very high purity URu_2Si_2 samples all came from the edge of the pulled crystal. One way to define the quality of a metallic crystal is the residual resistivity ratio $RRR = \rho(300\mathrm{K})/\rho_0$. The resistance value at 300 K does not depend on the quality of the sample, but the value at $T = 0$ is governed by impurity scattering and decreases therefore with

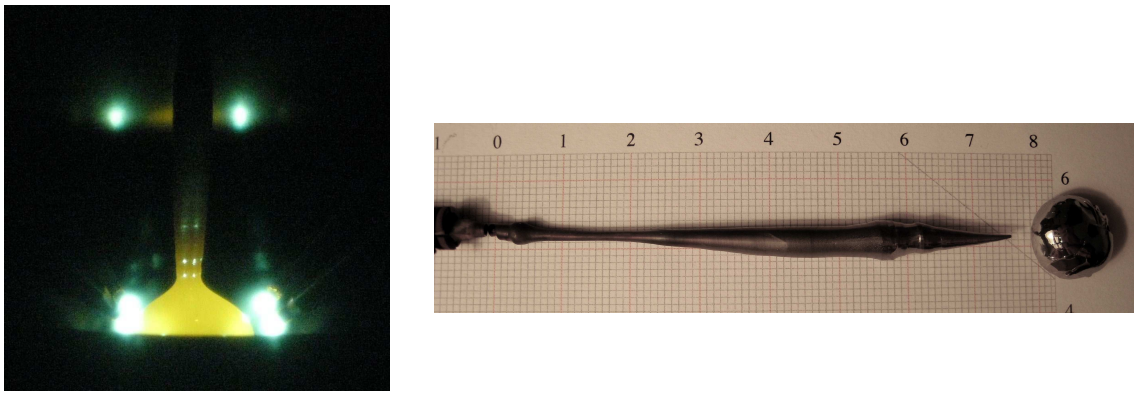

Fig. 2.1 : Photo of a tetra-arc furnace in action (left) and an as grown sample of URu_2Si_2 (right).

decreasing impurity concentration. In figure 2.2 is shown the temperature dependence of the resistivity ρ from 300 K to 0.5 K for two samples with slightly different quality. In URu_2Si_2, ρ_0 is very difficult to define, because superconductivity sets in at $T_{SC} = 1.5$ K. Above T_{SC}, the temperature behavior is not quadratic with temperature (as expected at low temperature) and quite sample dependent. Thus the extrapolation to $T = 0$ is not unambiguous.

The first report of coexistence of superconductivity and ferromagnetism in UCoGe has been published in 2007 (Huy et al. 2007). Therefore, only polycrystals with an $RRR \approx 28$ were available up till 2008 (first study of the pressure phase diagram). The first crystals made by Czochralski pulling method were not perfect single crystals, presenting several large single crystalline grains. The quality of these "almost" single crystalline sample was $RRR \approx 6$. One of these was used for the determination of the pressure phase diagram by simultaneous resistivity and ac-susceptibility measurement. The UCoGe sample for ac calorimetric measurements in a diamond anvil cell was a single crystal, oriented and polished to very small size by Tatsuma Matsuda.

To conclude, a good sample quality plays an important role for several reasons: a) We want to measure the intrinsic properties of a system unaffected by the existence of impurities. In URu_2Si_2 it is known that the sample quality influences the pressure phase diagram, notably the critical pressure (Motoyama et al. 2003). b) Quantum oscillations appear only for high purity crystals, when the mean free path is large. The better the crystals are, the better is the signal in quantum oscillation measurements. c) The pressure effect on superconductivity is strongly dependent on the sample. In resistivity, superconductivity is only suppressed in the AF state, if the quality of the crystals is very high.

2.2 Electrical resistivity

The electrical resistance ρ in a metal is given by the scattering of electrons in a region $k_B T$ around the Fermi surface. The interactions are taken into account by introducing the effective mass $m^\star$. With the scattering lifetime τ the resistivity is given as

$$\rho = \frac{m^\star}{ne^2} \cdot \frac{1}{\tau} \tag{2.1}$$

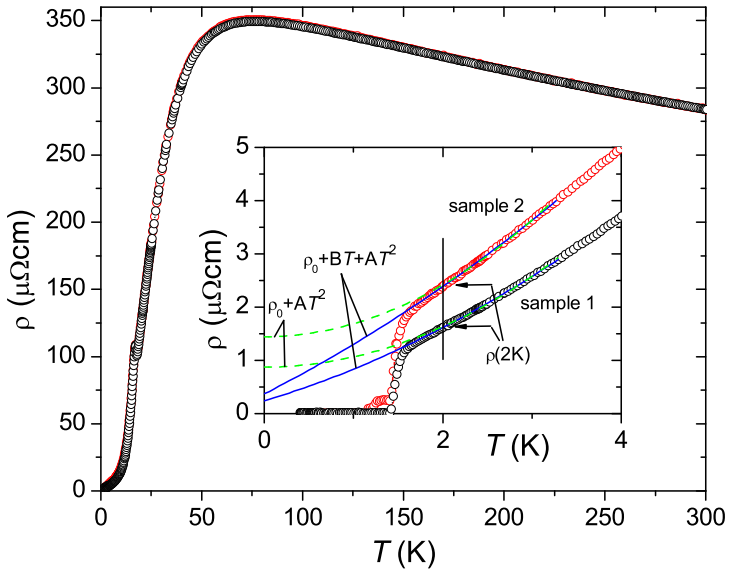

Fig. 2.2 : Resistivity of URu_2Si_2 in the whole temperature range for sample 1 and sample 2 and at low temperature in the inset. The difficulty to define ρ_0 is shown by the fits at low temperatures.

where n is the density of carriers and e the electric charge. The electrical conductivity is $1/\rho$.

In a metal for $T > 0$, there are always several scattering mechanisms and the total resistivity is given as

$$\rho = \rho_0 + \rho_{el} + \rho_{ph} + \rho_{mag}.$$

ρ_0 is the contribution from scattering with impurities. This gives a temperature independent term. The other terms come from scattering with excitations of the system: electrons, phonons and magnons.

At low temperature, far below the Debye temperature, the phonon term, which is proportional to T^5 becomes negligible and the electron contribution becomes dominant. The temperature dependence of the resistivity in the Fermi liquid regime is then given as

$$\rho = \rho_0 + A \cdot T^2.$$

The magnon term ρ_{mag} describes the scattering with magnetic excitations. It depends on the dispersion relation of the magnon spectrum. If there is an energy gap in the dispersion relation of the magnetic excitations, and the temperature is comparable to or lower than the gap energy, the number of magnons increases exponentially according to Boltzmann's principle. Then $\rho_{mag} \propto \frac{1}{\tau} \propto n_{mag} \propto e^{-\Delta/k_B T}$

Resistivity measurement

The resistivity ρ is measured via the standard four point contact method. Four gold wires with a diameter of 17 μm are spot welded on the sample, the outer ones for the injection of the measurement current and the inner ones for the voltage measurement. A Stanford

SR830 Lock In amplifier serves as alternating voltage source. An excitation voltage of 0.1 V through a $R = 10$ kΩ resistance delivers a current of $I = 10$ μA. Decreasing the current does not change the signal, for example the superconducting transition temperature, implying that the sample heating is negligible. The resistance of the cables and the sample can be neglected compared to this resistance. The measurement frequency is 17 Hz. The measurement signal is amplified first by a room temperature transformer by a factor of 100 and second by a Stanford SR560 low noise pre-amplifier by a factor of 1000. The error on resistivity is mainly due to the uncertainty of the geometric factor. This is a systematic error, basically just a wrong normalization factor. In this work, we obtained absolute values for the resistivity by normalizing the room temperature resistivity to the value of a sample with well defined geometrical factor which is $\rho_a(300\,\mathrm{K}) = 285\,\mu\Omega\mathrm{cm}$ for URu_2Si_2 for the current along the crystalline a axis. For the Shubnikov-de Haas measurements, a low temperature transformer with amplification factor 1000 was used with the room temperature preamplifier, which leads to a very low noise level.

2.3 Specific heat

Just like the resistivity, the specific heat has different contributions (electronic, lattice, magnetic and nuclear contributions):

$$C = C_{el} + C_{ph} + C_{mag} + C_{nuc}$$

In this work, the specific heat was measured in order to determine the transition temperature as a function of pressure. At bulk phase transitions, the specific heat usually shows an anomaly. No attention was given to the absolute value of the measurement signal and to the temperature dependence other than the anomaly.

Ac-calorimetry under pressure

For an ideal specific heat measurement, the sample must be thermally isolated from its environment. Then a certain known amount of energy is added increasing the internal energy of the sample by ΔU and the temperature enhancement of the sample ΔT is determined. The specific heat C is calculated with the formula $C = \frac{\Delta U}{\Delta T}$ for $\Delta T \longrightarrow 0$.

In a pressure cell the sample is thermally coupled with the Argon bath and the measurement wires. The coupling depends on temperature and pressure and is not well known. Therefore we use the ac-calorimetric method described more detailed in (Demuer et al. 2000; Wilhelm and Jaccard 2002). In this method the sample is heated with an alternating power $P = P_0(1 + \cos\omega t)$ where P_0 is the mean value and ω the oscillation frequency. The induced temperature oscillations T_{ac} of the sample are then measured with a thermometer. The coupling with the environment is taken into account as a heat leak with thermal conductance κ . A detailed description is given in reference (Sullivan and Seidel 1968).

The sample temperature consists of several terms:

$$T = T_b + T_{dc} + T_{ac}\cos\omega t \tag{2.2}$$

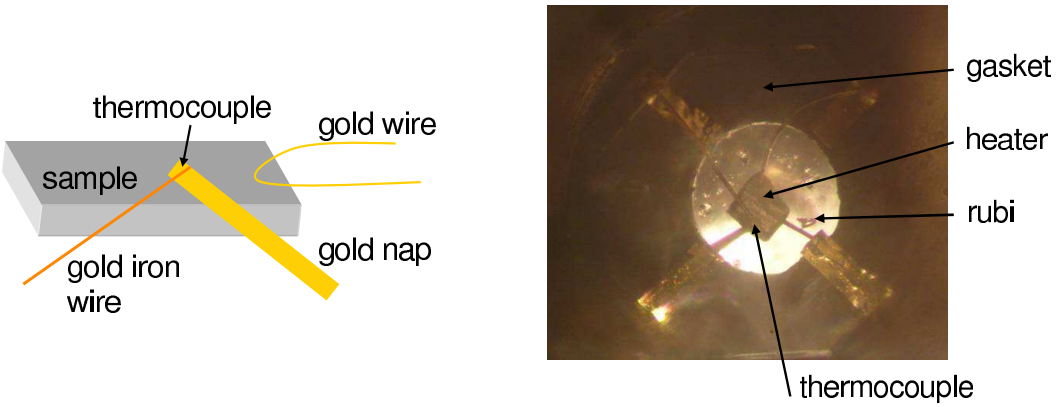

Fig. 2.3 : Schematic ac-calorimetry setup. Gold–gold/iron thermocouple and gold wire welded to the sample (left) and realization on a UCoGe sample in a diamond anvil cell (right).

with the temperature of the bath T_b, the average temperature increase due to heating $T_{dc} = \frac{P_0}{\kappa}$ and the temperature oscillation $T_{ac} \cos \omega t$ with the same frequency as the heating and the amplitude T_{ac}. Thus we obtain

$$T_{ac} e^{i\phi} = \frac{P_0}{\kappa + i\omega C_{ac}}. \tag{2.3}$$

Φ is the phase shift between the heating and the T_{ac} signal. The measurement frequency has to be chosen high enough to decouple the sample from its environment i.e. $\omega C_{ac} \gg \kappa$, but not so high that the heat is distributed inhomogeneously in the sample. In this case we obtain that the specific heat C_{ac} of the sample depends on the measured temperature oscillations T_{ac}

$$C_{ac} = \frac{P_0}{\omega T_{ac}} \propto \frac{1}{T_{ac}}. \tag{2.4}$$

In our setup, the sample is heated by resistive heating with a gold wire spot welded to the sample. The used thermometer is a thermocouple Au:Au(0.07%Fe) with a thermoelectric power $S = \frac{\Delta U}{\Delta T}$. The temperature dependence of the sensitivity of the thermocouple was measured by Chaussy *et al.* (Chaussy et al. 1982) and has at one Kelvin the value $S(1\text{K}) \approx 7\ \mu\text{V/K}$. It is assumed to be independent of pressure (Itskevich and Kraidenov 1978). The ac-part of the thermocouple voltage $V_{ac} = ST_{ac}$ and its phase shift to the heating is measured by a Lock In amplifier. As for the resistivity measurement the signal is amplified by a factor of 100 with a transformer and by a factor of 1000 by a preamplifier. It is then read out by the Lock In amplifier with the second harmonic of the excitation frequency.

Theoretically, we could work out C_p in absolute units. In reality this is not the case. The average heating power P_0 can theoretically be calculated knowing the resistance of the gold wires and the current, but an unknown part of the heating goes into the environment of the sample. As a consequence, the absolute value of the specific heat is not known. Another error comes from the fact that we measure not only the sample but also its environment. This gives us a pressure and temperature dependent background signal. As κ grows with temperature, the chosen frequency has to be determined experimentally by measuring the cutoff frequency of the signal.

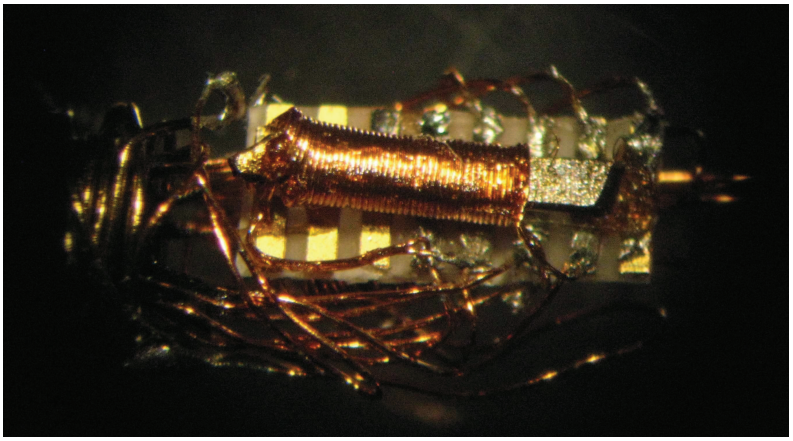

Fig. 2.4 : The setup for simultaneous resistivity and ac susceptibility measurements. One sample is used on the left side for the susceptibility measurements by two coils wound around the sample and on the right side the four small gold wires for the resistivity measurements. The whole setup is fixed to an opturator for a piston cylinder pressure cell.

Because of the unknown P_0 and background this method is only qualitative. It allows us to determine the transition temperatures where the specific heat shows an anomaly and to draw the phase diagram for different pressures. But it is known from previous measurements of e.g. $CeRhIn_5$ that this technique gives reliable even semi-quantitative data in the pressure region up to ~ 4 GPa (Knebel et al. 2004).

2.4 Ac-susceptibility

A system reacts to an applied magnetic field H with a magnetization M. Both quantities are related by the magnetic susceptibility χ by

$$M = \chi H.$$

The electronic contribution of the susceptibility in heavy fermion systems is large due to their large effective mass. The ac-susceptibility was measured with a small excitation and detection coils directly wound around the sample in the pressure cell as shown in figure 2.4. The coil is not compensated and therefore, the background signal is detected as well. Again, we do not look at the absolute value of the signal, the idea being to detect the phase transition temperatures. The strong diamagnetism in the superconducting state makes the susceptibility a very sensitive method to detect the superconducting phase transition. At a ferromagnetic transition a pronounced peak appears in the susceptibility. Above the transition temperature T_{Curie}, strong fluctuations of the moment lead to an increase in the signal with decreasing temperature. The freezing of the moments below T_{Curie} decreases the susceptibility.

2.5 Extreme conditions

2.5.1 High pressure

Pressure is a controllable and reversible tool for tuning sample size and lattice parameter. Along with chemical doping and magnetic field it changes the hybridization in heavy fermion compounds and can induce a quantum phase transition. Contrary to chemical substitution which leads to disorder effects, pressure is a clean method to change the lattice parameter with the slight disadvantage that negative pressures are not procurable. And hydrostatic pressure conditions are difficult to achieve.

Working under high pressure is experimentally difficult for several reasons: Since pressure is defined as

$$P = \frac{F}{A} \qquad [P] = \mathrm{GPa} = 10\,\mathrm{kbar} = 10^9 \frac{\mathrm{N}}{\mathrm{m}^2} = 10^9 \frac{\mathrm{kg}}{\mathrm{ms}^2} \tag{2.5}$$

high pressure requires a large force F on a small surface A. Especially for diamond anvil cells, with a high maximum pressure of around 20 GPa, the pressure chamber and hence sample sizes are very small ($< 50\,\mu$m thick and up to $300\,\mu$m long). This makes handling the sample delicate. Another difficulty is to introduce the measuring wires into the pressure chamber without loosing leak tightness. Typical gaskets are made out of stainless steel. The measuring wires have to be electrically isolated against it to avoid shorts to ground while the setup has to stay leak proof. The technique using an epoxy film for isolation is well established in the laboratory and described in paragraph 2.5.1. Additionally, pressure is not a continuous variable and measurements are usually temperature or field scans at constant pressure. In this study, the change of pressure is implemented at room temperature and pressure reduces upon cooling. In a diamond anvil cell, the reduction is between 0.5 GPa and 1 GPa but below $T = 50$ K it does not change significantly (Thomasson et al. 1989). There is a technique to change the pressure in situ at low temperature. I compared the pressure conditions in the two cases described in paragraph 2.5.1.

A large variety of different pressure cells exist, for example piston-cylinder pressure cells, Bridgman cells and diamond anvil pressure cells. The choice of the sample depends on the required maximum pressure and the measurement method.

Piston cylinder pressure cell

A hybrid non-magnetic piston cylinder pressure cell as presented in figure 2.5 has been used for the Fermi surface studies of URu_2Si_2 and most of the pressure studies on UCoGe. The advantage of these pressure cells is that the pressure chamber is big, which allows an easier sample preparation and setup. With the maximum pressure of 3 GPa, the interesting pressure range is covered for both compounds. The cell consists of a cell body out of CuBe, enforced with an inner cylinder of non-magnetic tungsten carbide (CW). On the lower side the measurement wires are introduced to the pressure chamber through a small hole in the obturator (plug). The obturator is held by a fixed locking nut (lower screw). On the top, a CW piston is pressed on the pressure chamber by a second upper locking nut (upper screw). The pressure chamber is sealed by a Teflon cell, filled with the pressure transmitting medium and stuck onto the sample setup fixed to the obturator.

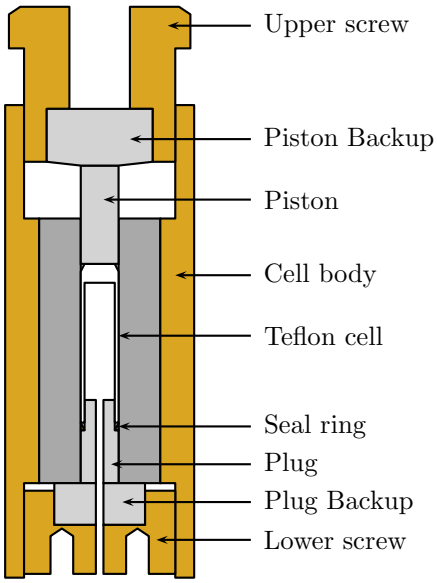

Fig. 2.5 : Scheme of the piston cylinder pressure cell used in this study.

Diamond anvil pressure cell

A diamond anvil cell (see figure 2.6) was used for ac-calorimetric and ac-susceptibility measurements on UCoGe and in my Diplomarbeit for the determination of the pressure-temperature phase diagram of URu_2Si_2. It is made out of CuBe with anvils made out of the hardest material known, diamond. Two flat diamond anvils with a table diameter of $d = 1\,\mathrm{mm}$ are glued to the pistons. They are aligned coplanar with the help of Newton rings. One of the pistons is fixed to the outer cylinder, the other one can be moved by turning three screws in order to apply or to change the pressure. The mobile piston is well guided along the symmetry axis in the cylinder with the help of a groove to avoid inhomogeneous pressure on the diamonds which could make them break. The two diamonds exert pressure on a gasket with a hole, the pressure chamber, filled with the pressure transmitting element. The sample is immersed in this liquid in hydrostatic pressure conditions.

Due to the large forces a pressure cell setup can fail at several stages: During loading the failure rate is about 75 %. Frequent heating and cooling works on the wires and can break them. Last but not least the pressure chamber is deformed when the pressure is changed. This can induce a breaking of the wires and also short circuits, when the wires or the sample touch the gasket.

Gasket The key point to a successful pressure cell setup is the gasket. The pressure cell is first mounted with the gasket only. By applying a force of about 8000 N the gasket is preformed until the thickness of it between the diamonds is about 100 μm. In the center of the diamond impression a hole is drilled by hand with a diameter of 500 μm. This is the pressure chamber (see figure 2.6). The insulation between gasket and measurement wires is assured by a thin layer of epoxy glue (stycast) mixed and saturated with Al_2O_3 powder, which gives the required rigidity and strength to resist high pressure. On four

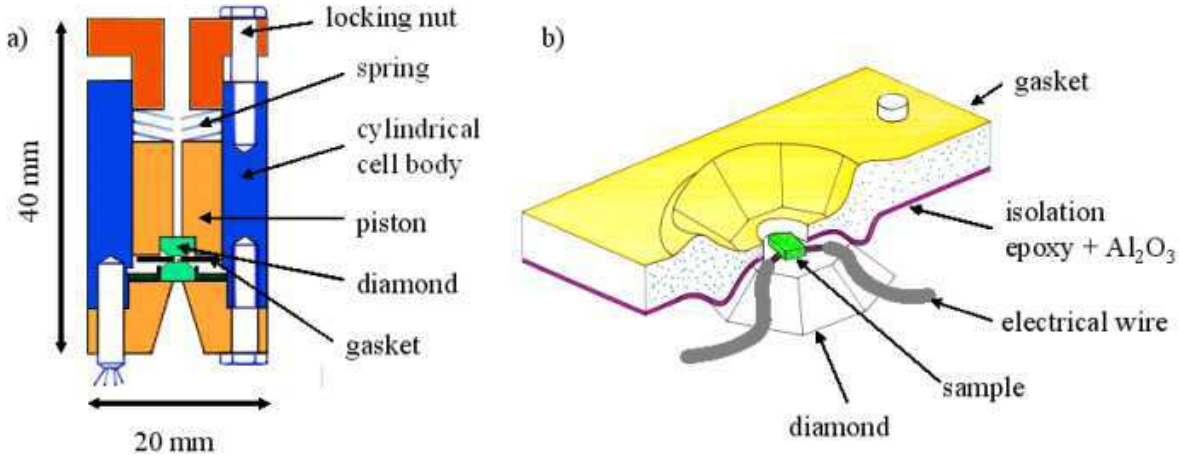

Fig. 2.6 : Diamond anvil pressure cell (a) and gasket (b) as used in this work.

sides of the diamond there are contacts for the measurement wires. Flattened 25 μm gold (or gold-iron for the thermocouple) wires are glued to these contacts with silver paint 6929 and attached perpendicularly to the diamond anvil. They are cut on the anvil table so that they don't enter the pressure chamber. Then the small 10 μm gold wires are contacted to the sample by spot welding. Typical welding parameters for the samples in this study were a voltage of U = 4 V and a time constant of $\tau = 9$ μs. For the resistivity setup the four wires must be bent all in the same direction before welding leading to the flexibility needed when the pressure chamber is deformed. Otherwise the wires or the bond would break. Finally the sample is placed on the diamond as seen in figure 2.6. The small wires are pushed under the broad wires arriving from the outside. The contact is achieved only under pressure when the cell is loaded. Next to it some rubies are arranged which will be necessary for the pressure measurement. In figure 2.3 a specific heat setup is photographed through the (unloaded) pressure cell with the help of a microscope. The diamond, sample in the pressure chamber, small wires, broad wires and the rubies are discernible.

Pressure transmitting elements In this study Argon is used as the pressure transmitting medium in diamond anvil cells. An evaluation of pressure transmitting media for cryogenic experiments with a diamond anvil cell is given in reference (Tateiwa and Haga 2009). The noble gases and especially Helium are the most adequate media because they are highly isotropic. The only interactions between the atoms are van der Waals forces which are non-directional. The enormous disadvantage of He is its high compressibility at low temperatures which induces large changes of the pressure volume. This causes problems with the measurement wires in the pressure chamber due to deformation. Argon is also highly hydrostatic at least up to 10 GPa (Thomasson et al. 1989). To load the cell, it is only slightly closed and plunged into liquid Argon for 45 min. After that time the cell is cold and almost no gas bubbles are formed any more. Pressurizing with a force of about 5500 N induces a pressure of about 1.1 GPa at room temperature.

For piston cylinder pressure cells, the chosen pressure transmitting element is Daphne oil 7373. Organic oils have the advantage that they form glasses at low temperature.

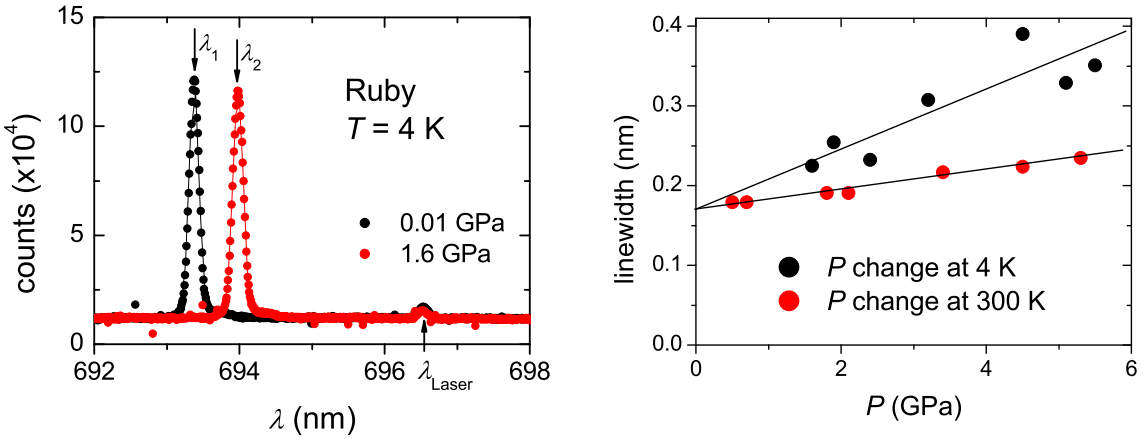

Fig. 2.7 : Left: Ruby spectra at 4.2 K for two different pressures in cell setup 1. Right: FWHM of the ruby line for two different setups. In one setup (red dots), the pressure has been changed at room temperature, and in the other setup (black dots), the pressure has been changed in situ at low temperature.

Pressure measurement

Lead method The superconducting temperature of lead decreases with pressure in a well established manner. By introducing a piece of pure lead into the pressure cell, we can determine the transition temperature by measuring either the resistivity or the ac-susceptibility. In piston cylinder pressure cells, there is enough space for such a pressure probe. The problem is that the transition temperature of lead is also sensitively affected by a magnetic field ($H_{c2} < 0.1$ T). With a remanent magnetic field of a superconducting magnet of around 0.01 T, the appearing pressure is higher than the actual pressure in the cell. By demagnetization cycles we have avoided this effect and for the measurements of the phase diagram of UCoGe, no magnetic field was used.

Ruby method In a diamond anvil cell with transparent anvils, the pressure is determined by ruby fluorescence. We introduce some ruby crystals into the pressure chamber next to the sample, which serve as pressure sensors. The wavelength of the fluorescence lines of rubies depends on pressure and on temperature. Below T$\approx$ 35 K the line position does not depend on temperature any more but only on pressure. By measuring the spectrum, we can deduce the pressure in the chamber at several positions. The rubies are excited by an Argon laser whose light is introduced to the pressure cell via an optical fiber. Here, we benefit from the fact that the diamond anvils are transparent. The outcoming light is again directed outside the cryostat via an optical fiber on the other side of the pressure cell. It is spectral-fragmented with a HR 1000 monochromator of Czerny-Turner type. The emission spectrum is taken with an Andor Technology CCD spectrometer. At room temperature $T = 300$ K and ambient pressure, two ruby lines called R_1 and R_2 are at positions $\lambda_{R_1} = 694.239$ nm and $\lambda_{R_1} = 692.82$ nm. With the help of these lines and a reference line from a Ne lamp the spectrometer is calibrated. Independently of temperature within an error of 3 % (Noack and Holzapfel 1979) the lines shift with 0.365 nm/GPa. The pressure is measured at room temperature and at 4.2 K. At low temperature, the excited state which leads to R_2 is not thermally populated and

therefore the line is not detectable. In the relevant pressure region, the pressure changes between 0.55 GPa and 1 GPa upon cooling. The absolute pressure error is estimated to be about $\Delta p \approx 0.05$ GPa for a change of pressure at room temperature. We always measured the pressure at 4.2 K before the measurements and before heating up. Within the error bar we have never observed changes in pressure between these two measurements without heating up in between. Therefore the pressure is stable. If the pressure in the chamber is not homogeneous, the different rubies will have slightly different emission lines. This leads to a broadening of the line. Hence its width indicates the homogeneity of pressure in the chamber. On the left side of figure 2.7 the ruby spectra at 4.2 K for two different pressures in one cell setup is shown: 0.01 GPa (black dots) and 1.6 GPa (red dots). The lines are Gaussian fits of the peaks with their maximum at $\lambda_1 = 693.38$ nm which corresponds to 0.01 GPa and $\lambda_2 = 693.98$ nm which corresponds to 1.6 GPa. The width of the peak in the low pressure spectrum is $0.137 \pm .0005$ nm, which is exactly the width of the peak of the rubies in the unloaded cell. For 1.6 GPa it is slightly enhanced to $0.147 \pm .0005$ nm showing a tiny loss of hydrostatic conditions. The small peak at $\lambda_{Laser} = 696.54\,\text{nm}$ is a harmonic of the laser.

Different pressure conditions Our laboratory has an apparatus, which allows to change the pressure in situ at low temperature. On the right side of figure 2.7, we compare the linewidth of the ruby line, which is an indication for the pressure homogeneity in the pressure chamber, as a function of pressure, when the pressure is changed at low temperatures with the case where the pressure is changed at room temperature. Clearly, the homogeneity is much higher when the pressure is changed at room temperature. And the linewidth is in both cases approximately proportional to the pressure. When increasing the pressure in situ, the additional pressure is applied on the solid pressure transmitting medium Argon. This creates strain and therefore pressure inhomogeneities. In the ideal case, the pressure is applied on a liquid. However, even at room temperature, Argon solidifies within the pressure ranges attained in our measurements, but it stays malleable at higher temperature, improving the pressure conditions and decreasing the linewidth.

2.5.2 Low temperatures

The principle of dilution cryostats is exhaustively described in the literature (Enns and Hunklinger 2005) and will not be presented here. Two different dilution cryostats have been used in this study. The measurements on UCoGe have been carried out with a home-made dilution cryostat with base temperature of $\approx 55\,\text{mK}$, the quantum oscillation measurements with a KelvinOx system with base temperature of $\approx 20\,\text{mK}$. The rotation system described below, was connected to the mixing chamber of this cryostat. The pressure cell or the sample is thermally connected to the mixing chamber. The temperature of the mixing chamber is measured with a calibrated RuO_2 thermometer in the field compensated region. A carefully field calibrated RuO_2 thermometer is thermally connected directly near the sample or pressure cell. The temperature regulation is assured by a ORPX 2 temperature controller with a regulation heater resistance.

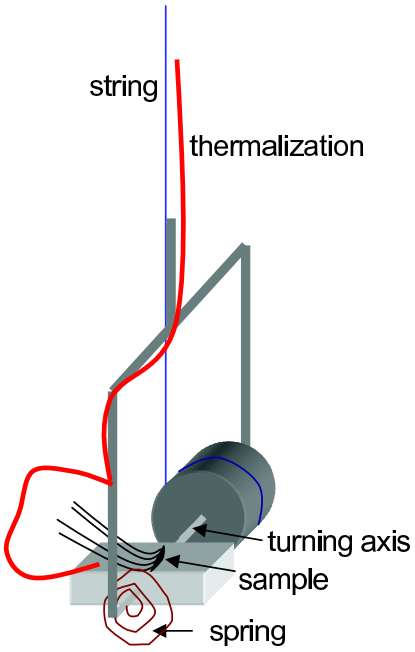

Fig. 2.8 : Scheme of the rotation system used for the measurement of the angular dependence of the Shubnikov-de Haas oscillations.

2.5.3 High magnetic fields

Magnetic fields for the quantum oscillation measurements were produced by a superconducting magnet with a maximum field of 13.2 T. The field was uniformly swept at a rate of 0.02 T/min for the ambient pressure measurements and at 0.01 T/min with the pressure cell in order to avoid eddy current heating. Nevertheless, a small temperature increase of the pressure cell was registered (≈ 5 mK) with increasing field causing an uncertainty of the temperature and thus a slightly higher error in the determination of the effective masses.

2.5.4 The rotation system

The rotation system used for the Fermi surface study is shown in figure 2.8. It is made out of plastic in order to reduce eddy current heating. The sample is fixed on a sample plate, itself fixed to a turnable axis. The axis is held rotatably in a frame and fixed to it via a spring, which is always held under tension. The axis can be turned from outside the cryostat by pulling on an inductile Kevlar string via a micrometric screw. Thermalization between the thermometer and the sample stage is achieved by a silver foil (here presented in red), on which the sample is glued. The angle is determined by the well known angular dependence of the superconducting critical field (Ohkuni et al. 1999).

2.6 Analysis of Shubnikov-de Haas measurements

The oscillation signal in URu_2Si_2 consists of several fundamental frequencies and their harmonics and combinations. It is therefore very difficult to determine the oscillation amplitudes and frequencies directly in the raw data. In order to determine the amplitudes separately, Fast Fourier transforms (FFT) have been performed. The data treatment has

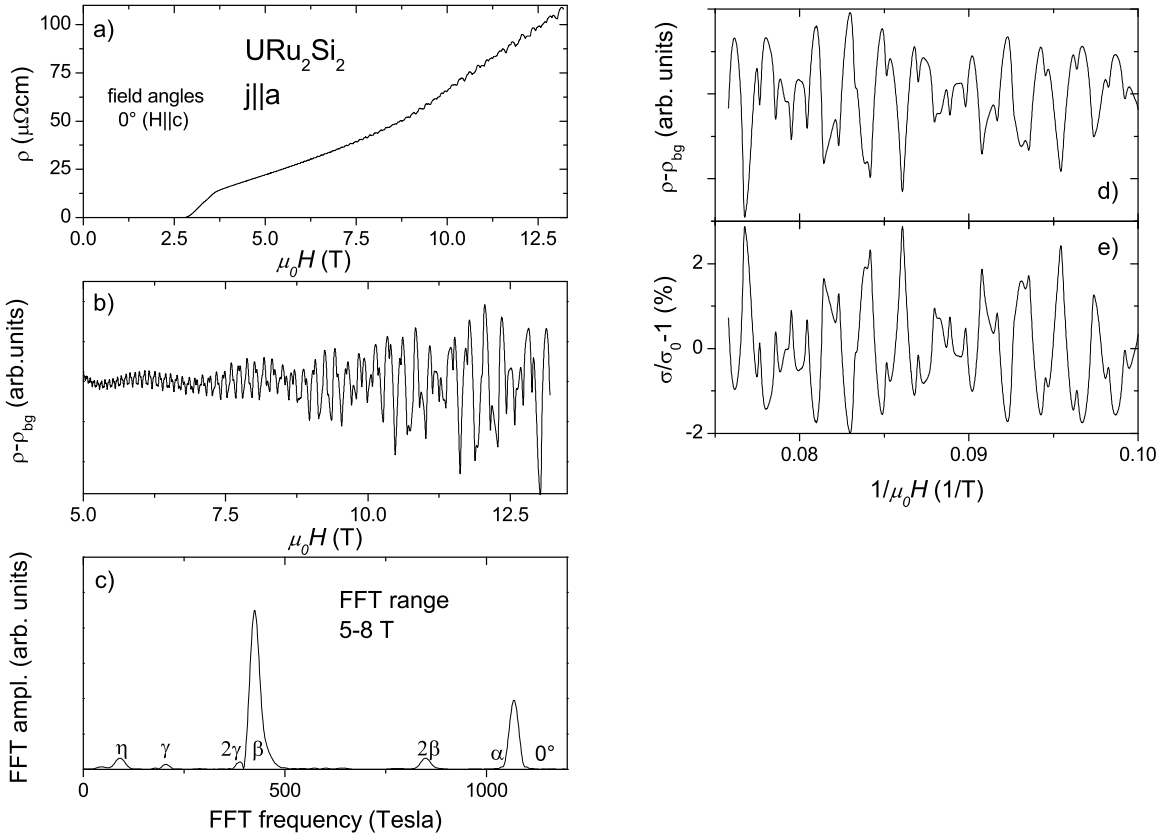

Fig. 2.9 : a) Magnetoresistance of URu_2Si_2at the lowest temperature $T = 25\,\mathrm{mK}$. b) Oscillatory part of the resistance as a function of field. c) FFT amplitude of this oscillatory part between 5 T and 8 T. d) Oscillatory part of the resistance as a function of the inverse field. e) Relative oscillatory part of the conductivity as a function of the inverse field.

been automatized with a specially written Matlab program. It consists of the following steps presented in figure 2.9. The resistivity as a function of the magnetic field $\rho(H)$ at constant temperature is shown in figure 2.9a. Firstly, this signal is interpolated by equidistant 2^n points (n is a natural number) in $1/H$, with 2^n higher than the number of measurement points. This number of points determines the highest frequency in the FFT spectrum and the 2^n is needed to optimize the Fourier transform (FT) algorithm. The non-oscillatory "background" of the resistivity ρ_{bg} is obtained by a polynomial fit in $\rho(H)$. The order of the polynomial does only affect the very low frequency part of the spectrum. The oscillatory part of the resistivity can be obtained by subtracting the ρ_{bg} as in figure 2.9b as a function of field. For fields higher than 10 T, the same signal as a function of reciprocal field is shown in figure 2.9d.

The conductivity is $\sigma = \frac{1}{\rho}$. The oscillatory part $\widetilde{\sigma}$ is then obtained by subtracting $\sigma_0 = \frac{1}{\rho_{bg}}$ from σ and the relative oscillations, given in the Lifshitz Kosevich theory by the relative oscillations of the density of states is then given as $\frac{\widetilde{\sigma}}{\sigma_0}$ (see figure 2.9e). The FFT of this SdH signal is then given in figure 2.9c.

2.6.1 Fourier transforms

In this paragraph, only very few aspects of a FT will be mentioned, which will be important for our study. For further reading see for example (Brigham 1974). Usually, the FT of a signal in time will give a frequency spectrum (here, only the real part of the FT is taken into account). In a SdH study, the analog of time is the inverse field. Therefore, the frequencies will appear in units of the field (Tesla). FFTs have been performed on the discrete signal to determine the power spectrum. Other methods have been tried (see figure 2.10), but the results of the FFT are most convenient for our study with the best resolution and no sensitivity of the frequencies to the window function (compare for example the spectra obtained by the Yule-Walker method without a window function and with a Hanning window function). In real measurements, the time respectively inverse field of the measurement T_c is finite. Mathematically this corresponds to multiplying the measurement function with a window function. If the signal in time is a multiplication of several functions, for example a perfectly periodic sine function with a square window function, then the FFT spectrum will be a convolution of the FT of the two functions, i.e. a convolution of a delta peak with a sine cardinal. The window function will enhance the width of the peak in the FT spectrum according to Heisenberg's uncertainty relation. The discontinuous jumps of the window function create strong side peaks called "side lobes". These side lobes can be reduced by multiplying the signal with a smooth function going to zero at the window edges. One example is the Hanning function H, which is used in this study

$$H(t) = \frac{1}{2} - \frac{1}{2}\cos(2\pi t/T_c)$$

It is a good compromise between the width of the peak and the intensity of the side lobes. The maximum inverse field range measured T_c gives the minimum detectable frequency $f = 1/T_c$. The distance of the measurement points gives the maximum detectable frequency. By adding zeros to the signal, we artificially increase the measurement time. Of course, the resolution is not enhanced but this method (called "zero padding") creates a

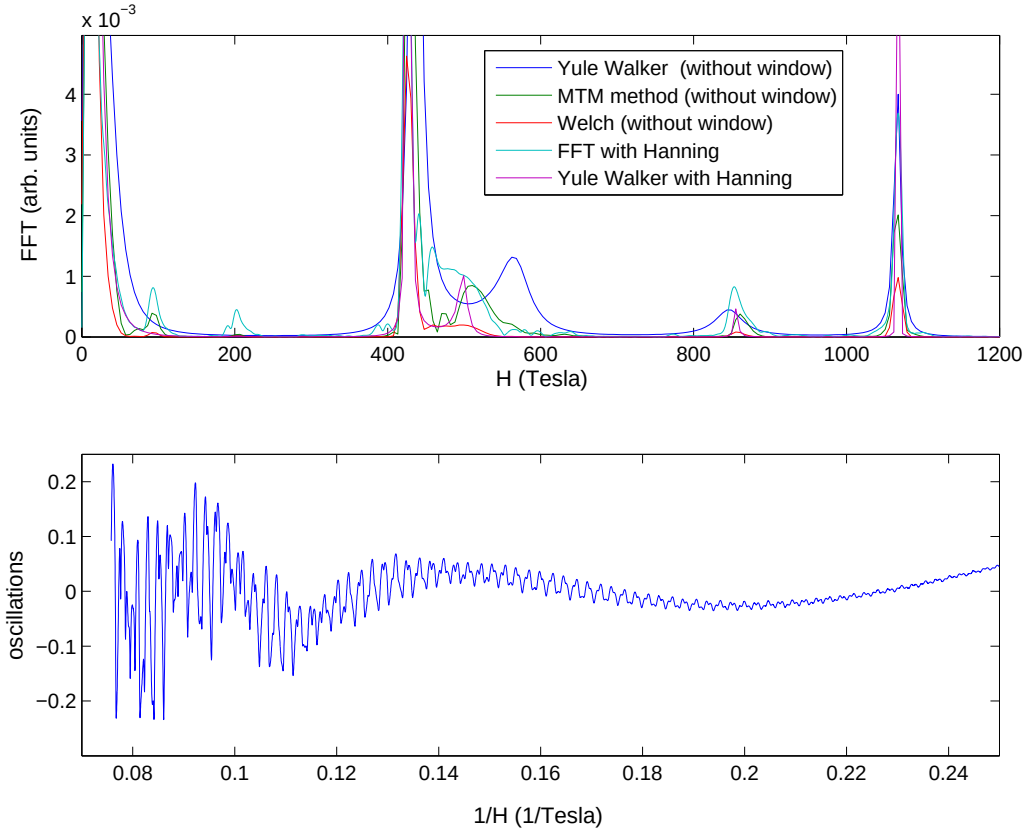

Fig. 2.10 : The spectral weight obtained from different spectral analysis algorithms. "Without window" means effectively a square window function. In the bottom panel this signal which was evaluated is shown.

smooth curve in the spectrum. This way, it is easy to determine the maximum value of a peak and its position without fitting.

The shape of the peaks in the FFT spectrum of a SdH signal is quite complicated. It is the convolution of the FT of the Lifshitz Kosevich function for $\frac{\tilde{\sigma}}{\sigma_0}$ with the FT of the Hanning window function given as:

$$\left|\tilde{H}(f)\right| = \frac{1}{2}Q(f) + \frac{1}{4}\left[Q\left(f + \frac{1}{T_c}\right) + Q\left(f - \frac{1}{T_c}\right)\right]$$

where

$$Q(f) = \frac{\sin(\pi T_c f)}{\pi f}.$$

For the field dependent analysis of the mean free path l_0, the inverse field range is divided into a smaller ranges, for example 0.5 times the total field range (in my notation $FFTrange = 0.5$). The smaller the range, the larger is the highest attainable effective field. However, the smaller the inverse field range over which the FFT is taken, the worse the resolution. As in URu_2Si_2 the frequencies are small and close to each other, this leads to interference effects of the FFT and two peaks can not be separated. One example of

such an effect is the beating of two very close frequencies. If the inverse field range is on the belly of the signal, only one frequency appears in the FFT spectrum, but if the inverse field range includes a node, two frequencies are resolved.

Chapter 3

Fermi surface studies in URu_2Si_2

3.1 Introduction to URu_2Si_2

Despite more than 25 years of intense research, details of the electronic structure and the Fermi surface in the HO state of URu_2Si_2 are still unknown. There are recent propositions for a variety of order parameters which lead to different Fermi surfaces due to different participation of the $5f$ electrons to the Fermi surface: multipolar orders (Cricchio et al. 2009; Harima et al. 2010; Haule and Kotliar 2009), dynamical spin density wave (Elgazzar et al. 2009) or hybridization wave (Dubi and Balatsky 2010).

Experimentally, the electronic structure has not been determined in a sufficient way to solve this problem. Optical conductivity (Bonn et al. 1988) and Hall effect (Schoenes et al. 1987) indicate a gap opening and a drop in the number of charge carriers at T_0. Recent STM measurements directly show that a hybridization gap opens suddenly at T_0 (Aynajian et al. 2010; Schmidt et al. 2010). High resolution ARPES measurements also detect abrupt changes of the Fermi surface at T_0 (Santander-Syro et al. 2009; Yoshida et al. 2010), but they only access limited regions of reciprocal space. To date, quantum oscillation measurements have detected three small pockets at low fields (Bergemann et al. 1997; Keller et al. 1998; Ohkuni et al. 1999) and one bigger pocket at fields $H > 17\,\mathrm{T}$ (Shishido et al. 2009) but these can only explain a small fraction of the enhanced mass implied by specific heat.

The pressure phase diagram is well established now with an antiferromagnetic state appearing above a critical pressure of $P_x \approx 0.8\,\mathrm{GPa}$ (Amitsuka et al. 2007; Butch et al. 2010; Hassinger et al. 2008) with an ordered moment of $\approx 0.33\,\mu_\mathrm{B}$. At $T_\mathrm{SC} \approx 1.4\,\mathrm{K}$ superconductivity sets in in the HO phase, but it is suppressed under pressure in the AF phase (Amitsuka et al. 2007; Hassinger et al. 2008). The fact that there is a clear first order transition line between HO phase and AF phase (Bourdarot et al. 2005a; Hassinger et al. 2008; Motoyama et al. 2003; Niklowitz et al. 2010) implies that the symmetry of the two phases can be completely independent. However, the electronic properties seen in the anomaly at the transition temperature show little change when entering either the HO phase or the AF phase from the paramagnetic state (Hassinger et al. 2008; McElfresh et al. 1987), suggesting that the reconstruction of the Fermi surface is similar in both phases. Inelastic neutron scattering experiments reveal two different magnetic excitations at wavevectors $\mathrm{Q_{AF}} = (0\ 0\ 1)$ and $\mathrm{Q_{inc}} = (0\ 0\ 0.6)$ in the HO state. By applying pressure the excitation at $\mathrm{Q_{AF}}$ disappears in the AF state (Villaume et al. 2008). To

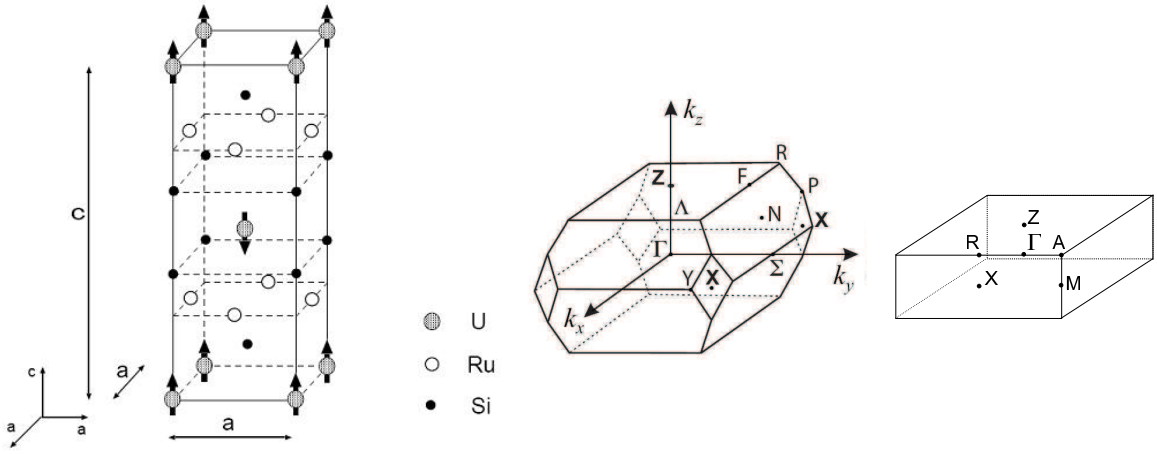

Fig. 3.1 : Left: Crystal structure of URu_2Si_2 with the ordered moments in the AF phase. If moments are neglected the crystal structure is body centered tetragonal (bct), in the ordered phase it is simple tetragonal, as the U atom in the middle is not equivalent to the surrounding U atoms any more. Middle: Brillouin zone of the bct crystal structure. Right: Brillouin zone of the simple tetragonal crystal structure of the AF phase.

date, the magnetic excitation at Q_{AF} is the only microscopic signature of the HO state. This led to the proposal that Q_{AF} could be the ordering vector also in the HO state. In the AF state the measured changes of the Fermi surface at the transition temperature can be explained by band folding, when the magnetic order changes the Brillouin zone (Elgazzar et al. 2009). If the same band folding also happens in the HO phase, because the ordering vector is the same, the Fermi surface should not change drastically between AF and HO states as indicated already by Shubnikov-de Haas (SdH) measurements of one light band in both phases (Nakashima et al. 2003).

It is one of the fundamental questions about the hidden order, which symmetry the order parameter has. Our approach to the solution of this problem, is the comparison of the electronic properties in the HO phase to the electronic properties in the AF phase. In order to probe the Fermi surface directly in both phases, we carried out magnetoresistance and SdH measurements at ambient pressure in the HO state and under pressure in the AF state on new high quality single crystals. As URu_2Si_2 is a semimetal, this is a good method to detect quantum oscillations in this material. Knowing the Fermi surface allows testing different calculations of the Fermi surface based on different order parameters. Hence, the question of the participation of the f electrons to the Fermi surface can be answered.

3.1.1 URu_2Si_2 at ambient pressure

Hidden order phase: Condensation process out of a Kondo liquid

URu_2Si_2 is a uranium based heavy fermion system. It has a body centered tetragonal $ThCr_2Si_2$ crystal structure with I4/mmm group symmetry (see figure 3.1)(Palstra et al. 1985). Its lattice parameters are a = b = 4.124 Å, c = 9.5817 Å at 4.2 K. These values are $\sim 0.1\,\%$ smaller than the values at room temperature and the crystal structure does not change upon cooling (Palstra et al. 1985). After Schlabitz *et al.* had found hints to superconductivity in polycrystalline samples of URu_2Si_2 (Schlabitz 1984), single crystals

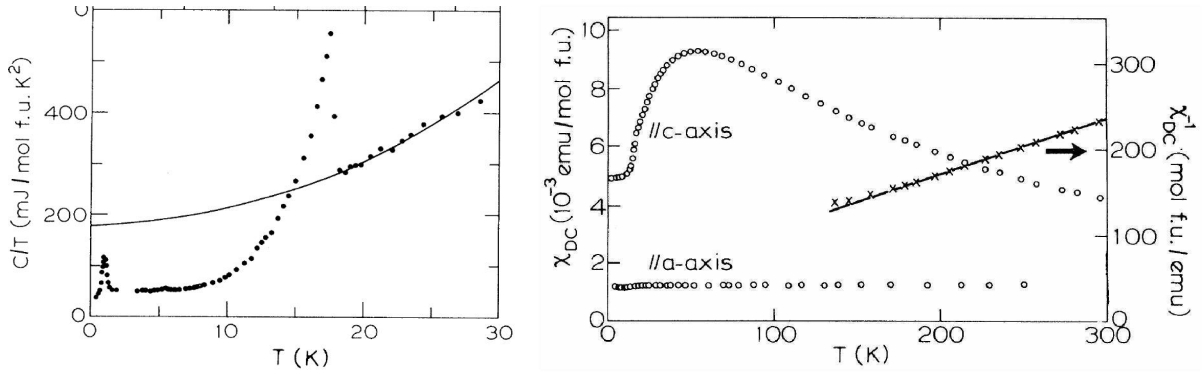

Fig. 3.2 : Left: Specific heat C/T of polycrystalline URu_2Si_2 sample. Right: Dc-susceptibility χ_{dc} of a monocrystalline URu_2Si_2 sample along $\vec{a}$ and $\vec{c}$ direction in a field of $\mu_0 H = 2\,\mathrm{T}$. The line is a Curie Weiss fit of the high temperature $1/\chi_{dc}$ data (crosses) along the c axis (Palstra et al. 1985).

have first been studied by Palstra *et al.* in 1985 (Palstra et al. 1985). Specific heat (of an annealed polycrystalline sample), susceptibility and magnetization at ambient pressure show two large anomalies. The anomaly at $T_0 = 17.5\,\mathrm{K}$ was interpreted as transition to antiferromagnetic order and the anomaly at $T_{sc} = 1\,\mathrm{K}$ as a transition to a superconducting state. Figure 3.2 shows the specific heat C/T with the two large anomalies. The line is a $\frac{C}{T} = \gamma + \frac{12\pi^2 N k_B}{5T_D^3} T^2$ fit to the high temperature data with a Debye temperature of $T_D \approx 300\,\mathrm{K}$. The y-axis intercept gives the γ value. One can see that it drops during the transition from $\sim 180\,\mathrm{mJ/molK^2}$ above T_0 to $\sim 65\,\mathrm{mJ/molK^2}$ at low temperature. This corresponds to an entropy change of $\Delta S \approx 0.2\,\mathrm{Rln}\,2$ and the estimated effective mass in the ordered phase is $m^\star \approx 25\,m_e$(Maple et al. 1986). The difference of the γ values above and below T_0 indicates that $\approx$60% of the conduction electrons are removed. The transition at T_0 resembles a BCS-like electronic condensation process (Maple et al. 1986) with a gap opening on part of the Fermi surface. The specific heat data can also be well fitted with a gap-like exponential decay for temperatures between 2 K and 17 K:

$$C = \gamma T + \beta T^3 + \delta \exp(-\Delta/T) \tag{3.1}$$

This fit gives an energy gap of $\Delta \approx 120\,\mathrm{K}$. Furthermore a broad Schottky-like anomaly is found at $\sim 60\,\mathrm{K}$ beyond the presented temperature scale, but a comparison to the specific heat of $ThRu_2Si_2$ shows that it is not a Schottky anomaly (Wiebe 2009). No crystal field levels are observed in specific heat, a first indication that URu_2Si_2 is an intermediate valence system with fluctuations between the configurations U^{3+} and U^{4+}.

The right side of figure 3.2 shows the dc-susceptibility χ_{dc} of a single crystal measured along the two different crystallographic axes (Palstra et al. 1985). The response is highly anisotropic with the easy axis $\vec{c}$ and small magnetization along $\vec{a}$. The large anisotropy implies that magnetism is understood on the basis of an Ising-like localized moment picture. The Curie-Weiss fit for the high temperature data $1/\chi_{dc}$ (crosses) indicates an effective moment of $3.51\,\mu_B$ with a Curie-Weiss temperature $\Theta_{CW} = -65\,\mathrm{K}$. The data deviate from the Curie-Weiss behavior already at 150 K, when Kondo screening sets in. Below the temperature of the maximum at around 50 K coherence effects set in. The value of the dc-susceptibility at 300 K is 30 times larger than the value for the non-magnetic

analogue $ThRu_2Si_2$ (Hiebl et al. 1983). Magnetization measurement reveal that the slope dM/dT becomes larger for $T < T_0$ indicating the formation of a spin gap (Park et al. 1997).

The resistivity is also anisotropic and much larger along the a axis (see figure 3.3 (Palstra et al. 1986)). Its behavior for $I \parallel a$ has five regions:

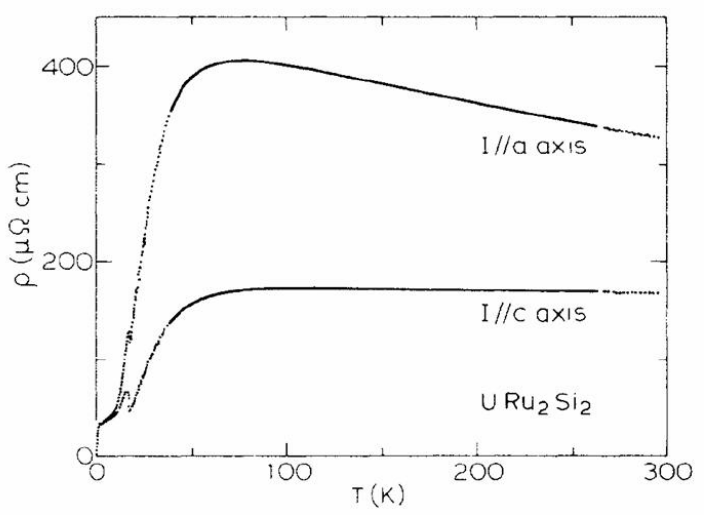

Fig. 3.3 : Resistivity of a monocrystalline URu_2Si_2 sample along a and c direction (Palstra et al. 1986).

- At high temperature the resistivity is determined by the Kondo effect with a $\rho \propto -\ln(\frac{T}{T_K})$ behavior. Here the uranium atoms are the magnetic impurities. The Kondo temperature derived from resistivity is very high $T_K \approx 370\,\mathrm{K}$ (Schoenes et al. 1987).

- Below the large maximum at $T_m \approx 75\,\mathrm{K}$ the resistivity decreases dramatically due to coherence effects in a Kondo lattice. The quasi-particle bands are formed.

- At T_0, the resistivity curves in both crystal directions show a remarkable transition similar to that of the SDW itinerant antiferromagnet chromium with an evident loss of carrier density causing a jump in resistivity. However, this anomaly is rather small for a current along the a axis and large for a current along the c axis. This is an indication of an anisotropic gap opening.

- Below T_0 attempts have been made to describe the resistivity by the theory of a an energy gap (Δ) antiferromagnet (Hessel Andersen 1980) with an additional Fermi-liquid T^2 term:

$$\rho = \rho_0 + AT^2 + bT(1 + 2T/\Delta)\exp(-\Delta/T) \tag{3.2}$$

with $\Delta = 90(68)\,\mathrm{K}$ parallel to the $a(c)$ axis. This fit is obviously not valid, knowing that the HO is non-magnetic that the spin excitations are longitudinal and thus that standard magnons don't exist in this compound. Neutron scattering however

reveals well defined gapped spin excitations, which is the reason for the exponential behavior. At low temperature, just above the superconducting transition, no T^2 behavior is found (Hassinger et al. 2008; Maple et al. 1986; McElfresh et al. 1987; Zhu et al. 2009). In a recent study, the resistivity and Seebeck coefficient had a Fermi liquid like behavior for $j \parallel c$, but a linear dependence of the resistivity for $j \parallel a$ (Zhu et al. 2009).

- Below $T_{sc} \approx 1.4\,\mathrm{K}$ the compound becomes superconducting and the resistivity drops to zero.

Not only resistivity, but also other transport properties like thermal conductivity (Behnia et al. 2005) and Hall effect show signs of a strong reduction of the carrier number at T_0. The Hall coefficient for $H \parallel c$ shows a large hump similar to the susceptibility at around 60 K (Dawson et al. 1989; Kasahara et al. 2007; Schoenes et al. 1987). In both field directions, the Hall coefficient is positive (dominated by holes, which have a higher mobility than the electrons) and jumps by a factor of four for $H \parallel c$ and by a factor of ten for $H \parallel a$ (Kasahara et al. 2007; Schoenes et al. 1987) in the HO state. This is evidence for a reconstruction of the Fermi surface at T_0 with a loss of carriers. The carrier density in the HO state is therefore very small: From the Hall measurements, it is estimated to 0.05 holes per formula unit with crude assumption that it is a one band system (Schoenes et al. 1987) or to 0.021 holes per formula unit (Kasahara et al. 2007). URu_2Si_2 is therefore counted among the semi-metals.

URu_2Si_2 is also a compensated metal, impossible in a one band system. This was noticed by a large transverse magnetoresistance without saturation up to high magnetic fields of 10 T ($\Delta\rho/\rho_0 = 300$ at 10 T) (Kasahara et al. 2007; Ohkuni et al. 1997). The reason for the transverse magnetoresistance is the orbital motion of the electrons perpendicular to the field. In a compensated metal, the number of electrons (n_e) and holes (n_h) are equal, giving a magnetoresistance (Pippard 1989)

$$\frac{\rho - \rho_0}{\rho_0} = (\omega_c^e \tau_e)(\omega_c^h \tau_h)$$

with the scattering times for electrons and holes τ_e and τ_h. As the cyclotron frequency is given as $\omega_c = eB/m^\star$, the magnetoresistance has a quadratic field dependence. If the compensation is not perfect, it will reach a saturation value (Pippard 1989) at high field. In very pure Bismuth crystals, the compensation is nearly perfect: A quadratic rise has been found up to $\Delta\rho/\rho_0 = 10^6$, the imbalance of $n_e/n_h - 1 < 10^{-3}$. In case of compensation, the Hall effect is also linear up to very high fields. This is confirmed up to 10 T in URu_2Si_2 (Kasahara et al. 2007).

The Seebeck coefficient (defined as the voltage induced along a sample by application of a temperature gradient $S = \Delta U/\Delta T$) divided by temperature S/T is slightly negative above the HO transition and decreases step like by a factor of ≈ 3 at T_0 (Bel et al. 2004). Its sign is not the same as the Hall coefficient, implying that the electrons carry more entropy (are heavier). The increase of the absolute value contrasts with the decrease of the Sommerfeld coefficient γ from $180\,\mathrm{mJ/molK^2}$ to $65\,\mathrm{mJ/molK^2}$. However, the γ value gives a measure of the entropy per volume (or per mole of URu_2Si_2) and the Seebeck coefficient gives a measure for the entropy per carrier. Hence, the transition leads to a

reduction of entropy per volume, but an enhancement of entropy per carrier (Bel et al. 2004).

The Nernst coefficient has an unprecedented high value for a heavy fermion superconductor with the same order of magnitude as that in the high T_{sc} superconductors (Bel et al. 2004). Thermal conductivity increases suddenly in the HO state due to sudden freezing of a major scattering mechanism of the heat carriers by reduction of the carrier number (Behnia et al. 2005; Sharma et al. 2006). Optical conductivity measurements also suggest (Bonn et al. 1988; Levallois et al. 2010) a charge gap.

New STM measurements with the quasiparticle interaction technique show that a hybridization gap opens suddenly at T_0 (Schmidt et al. 2010). The value of the gap in this case is $\Delta \approx 4\,\mathrm{meV}$. They estimate an effective mass of $m^\star \approx 28\,m_e$, comparable to an analysis of C/T (Maple et al. 1986).

High resolution ARPES measurements indicate strong changes at the Fermi surface (Santander-Syro et al. 2009; Yoshida et al. 2010) but they only access small regions of reciprocal space. Santander *et al.* (Santander-Syro et al. 2009) measure in the plane perpendicular to c slightly above the Γ point in the body centered tetragonal (bct) crystal structure (see the middle of figure 3.1), due to the photon energy provided by a He lamp. Above and below T_0 they detect a light band with larger vector $k_{(110)} \approx 0.2\,\mathrm{\AA}^{-1}$ than $k_{(100)} \approx 0.15\,\mathrm{\AA}^{-1}$. Additionally, they see a very flat and heavy band with $m \approx 22\,m_e$ passing below the Fermi level at T_0 when lowering the temperature. Yoshida et al. (Yoshida et al. 2010) carry out their measurements near the Z point of the body centered tetragonal Brillouin zone (BZ) as they use an ultraviolet laser (photon energy of 6.994 eV) as light source. They also detect a Fermi surface pocket at the Z point. Below the transition temperature, they detect a heavy band appearing below the Fermi energy. But contrary to Santander *et al.* they do not see it above T_0. They interpret this phenomenon by claiming that the unit cells doubles at T_0 by an ordering with wavevector Q_{AF} and therefore the Γ and the Z point become equivalent: In the tetragonal crystal structure (see the right side of figure 3.1), the BZ has only half the volume and half the height compared to the bct BZ in the middle of the figure. Therefore the Γ point of the second BZ on top of the tetragonal BZ, is equivalent to the Z point in the bct BZ.

Neutron scattering

During my PhD thesis a very strong interaction with the neutron scattering group of the SPSMS lead to several joint publications. I participated in the measurements and interpretation of the results, but did not do the data treatment. These results appear mostly in the following sections.

All neutron diffraction measurements reveal small antiferromagnetically ordered moments below T_0 (Broholm et al. 1987) at low temperature in the HO phase. In figure 3.1 the crystal structure of URu_2Si_2 is drawn. The moments m are ordered ferromagnetically in the planes perpendicular to c and antiferromagnetically between these planes, $Q_{AF} = (0,\, 0,\, 1)$. Figure 3.4 (Amitsuka et al. 2007) shows the results by different groups for the temperature dependence of the integrated scattering intensity I of the magnetic Bragg peak (for three-dimensional order $I \propto m^2 V_{af}$, where V_{af} is the antiferromagnetic volume) at $Q = (1, 0, 0)$ in reciprocal space. This is a forbidden nuclear peak and equivalent to Q_{AF} in the next Brillouin zone. As the moments are Ising like and ordered along

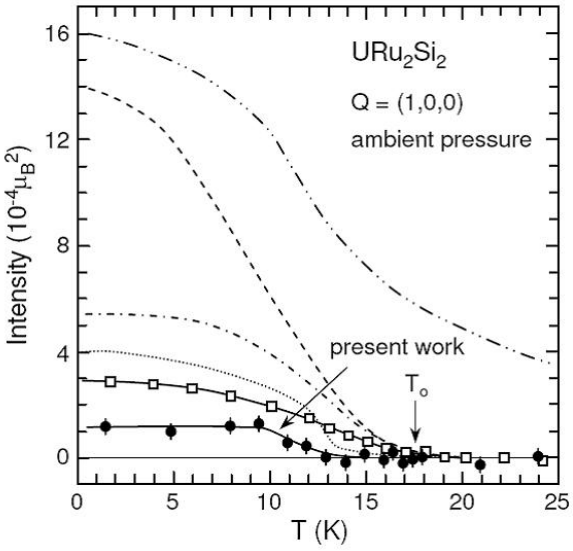

Fig. 3.4 : Neutron scattering intensity of the magnetic Bragg peak of URu_2Si_2 at $Q = (1, 0, 0)$ as a function of temperature from reference (Amitsuka et al. 2007). Data is from (Amitsuka et al. 2007) (closed circles), (Amitsuka et al. 1999) open squares, (Broholm et al. 1987) dash-double-dotted line, (Mason et al. 1990) (broken line), (Fak et al. 1996) (dash-dotted line), (Honma et al. 1999) (dotted line).

the c axis, they cannot be detected for Q_{AF}. The ordered moment for $T \longrightarrow 0$ is very small $m \approx 0.03 \pm 0.01\,\mu_B$ and stands in contrast to the fluctuating moment obtained from the high temperature susceptibility of $m \approx 3.5\,\mu_B$. Additionally, the ordered moment at low temperature depends on the sample as seen in the figure 3.4 (Fak et al. 1996). The small ordered moment cannot account for the large entropy loss at T_0 that is observed as a jump in the specific heat, if we apply the following mean field formula (Marcenat et al. 1988), which is often obeyed in heavy fermion systems far from the critical point:

$$m_0^2 = 2\chi(T_N) \int_0^{T_N} C(T)\, dT \tag{3.3}$$

UPt_3 in comparison has a similar moment of $m = 0.02\,\mu_B$ in the antiferromagnetic phase below $T_N = 5\,\mathrm{K}$ but it shows no anomalies at the magnetic transition in macroscopic properties (Aeppli et al. 1988; Stewart et al. 1984).

In recent years, there is an agreement on the fact that the small moment is not intrinsic to the HO phase but rather a remainder of the pressure induced large moment antiferromagnetic phase in small regions of the sample near lattice defects (see section 3.1.2). URu_2Si_2 is also very sensitive to uniaxial pressure(Yokoyama et al. 2005). In agreement with that, NMR measurements on very pure samples detect no ordered moment within their sensitivity (Takagi et al. 2007). Therefore, the HO phase is not a phase of ordered magnetic dipoles.

Despite the absence of an elastic signal in neutron scattering measurements in the HO phase, there are strong inelastic signatures. The dispersion of the magnetic excitations of URu_2Si_2 in the HO phase is shown figure 3.5. There are two minimum and therefore two magnetic excitations with a commensurate propagation vector $Q_{AF} = (1\,0\,0)$ and an incommensurate propagation vector $Q_{inc} = (1.4\ 0\ 0)$. Note that the points $(1\,0.4\,0)$, $(1.4\,0, 0)$, $(0.6\,0\,0)$... are equivalent to Q_{inc} in the Brillouin zone. The two gaps are $\Delta_{AF} \approx 1.7\,\mathrm{meV}$ and $\Delta_{inc} \approx 4.8\,\mathrm{meV}$. Both excitations are very sharp (long lived). The excitation at Q_{AF} has an unusual asymmetric line shape (see the left side of figure 3.6 and the right side of figure 3.5) which can be explained taking into account the resolution of the spectrometer and the very steep dispersion relation (Bourdarot et al. 2010b). The

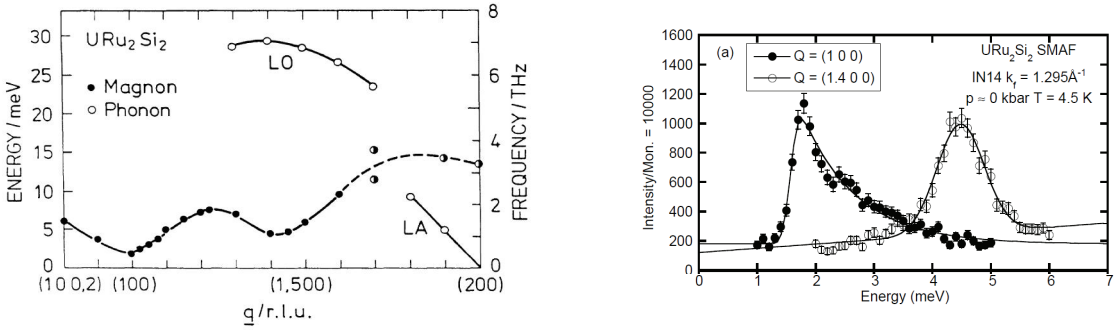

Fig. 3.5 : Left: Dispersion of magnetic (full circles) and phonon (open circles, linear optic phonons LO, linear acoustic phonons LA) excitations of URu_2Si_2 along $(\xi, 0, 0)$ and partly $(1, 0, \xi)$ at 4.2 K. Half filled circles denote a hybridized exciton-phonon mode (Broholm et al. 1991). Right: Energy spectra at fixed Q vector at the positions of the two minimum (Bourdarot et al. 2003b). Lines are guides to the eye.

fact that the excitations cannot be detected parallel to $Q = (0\,0\,1)$(just like the magnetic Bragg peaks), proves that these excitations are purely longitudinal (Broholm et al. 1991) and therefore not standard spin waves. This is not surprising in an Ising-like system. Our recent inelastic neutron experiments with polarized neutrons confirm this and also prove that these excitations are purely magnetic (Bourdarot et al. 2010b). It is not clear up to now, if the two minimum are connected or if they are represented by two independent dispersion lines which come close at higher energy.

The precise temperature dependence of the two excitations has been studied, but the results are sensitive to the model with which the spectra are fitted (Bourdarot et al. 2010b; Broholm et al. 1987; Mason et al. 1995; Wiebe et al. 2007). First measurements show that above T_0 the itinerant-like spin excitations with incommensurate wave vector $Q_{inc} = (1\,0.4\,0)$ are highly damped (i.e. very broad) and the gap stays finite (Broholm et al. 1987). Measurements of the intensity at this q-vector and a finite energy $E = 0.25$ THz in the gap show an exponential decrease below T_0 with an activation energy of 110 K, the same as the gap obtained in the specific heat (Wiebe et al. 2004). Maps of a large section of the (h 0 l) plane, which measure the intensity for a large range of energies, imply that the intensity at the Q_{inc} is higher than the intensity of the Q_{AF} excitations. Hence, the gapping of the excitations at Q_{inc} can explain the entropy jump at T_0 (Wiebe et al. 2007). However, the intensity difference could be an effect of the bad resolution, which artificially decreases the intensity of the more peaked excitation at Q_{AF}.

In our most recent measurements, after identifying Q_{AF} as the significant wavevector in the HO state (see section 3.1.2), we have measured the temperature dependence of the excitation at Q_{AF} with a very high energy resolution (Bourdarot et al. 2010b). The data at different temperatures are shown in figure 3.6. It is clear that the gap (right side of figure 3.6) is constant up to quite high temperatures (12 K) and then drops drastically to zero when approaching T_0 from low temperatures. The damping grows very quickly in the same manner just below T_0 (see the left side of figure 3.7). Above T_0 the behavior is quasi-elastic and the width continues to grow. The energy-integrated intensity has a temperature behavior of a mean-field like order parameter below T_0 (see the right side of figure 3.7).

Recently, inelastic neutron scattering (Broholm et al. 1991) measurements by our

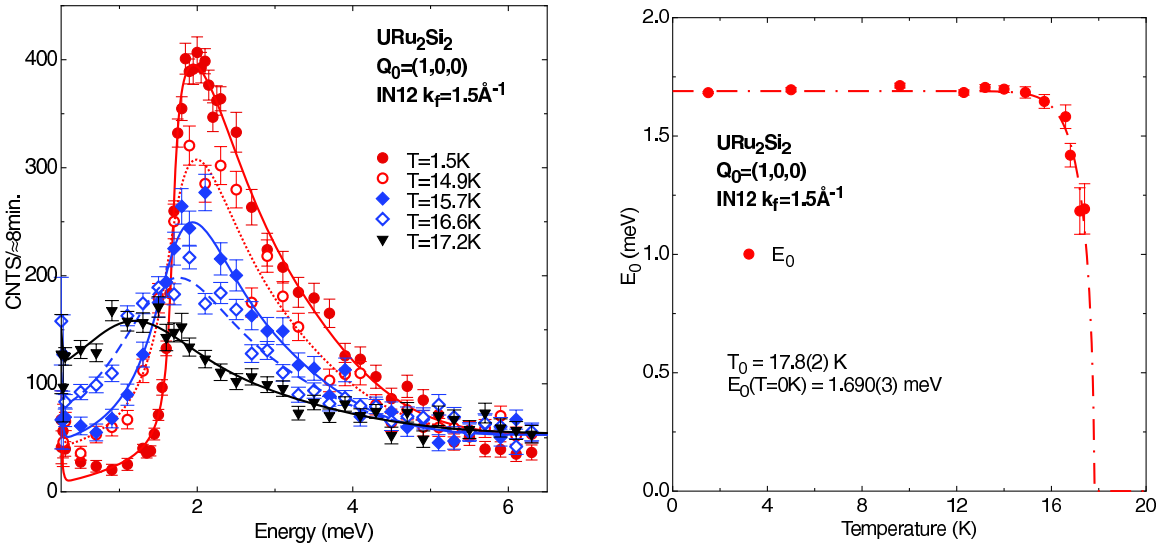

Fig. 3.6 : Left: Energy spectra at $Q_{AF} = (0\ 0\ 1)$ at different temperatures. Right: Temperature dependence of the gap obtained from these measurements. (Bourdarot et al. 2010b)

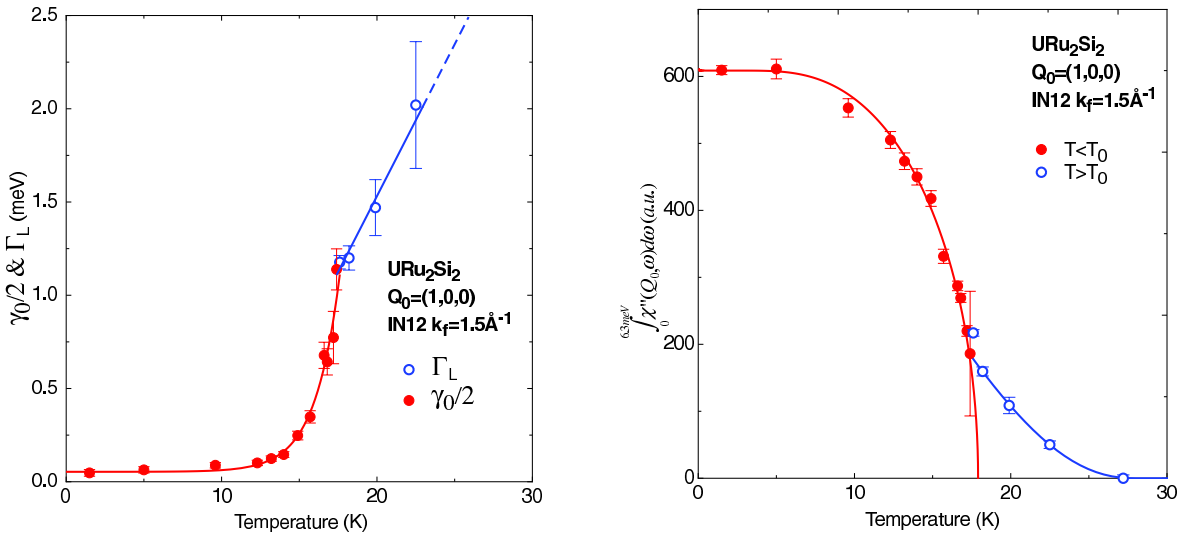

Fig. 3.7 : Left: The width of the excitation at $Q_{AF} = (0\ 0\ 1)$. Right: The integrated intensity of this excitation which follows a mean-field like temperature behavior. (Bourdarot et al. 2010b)

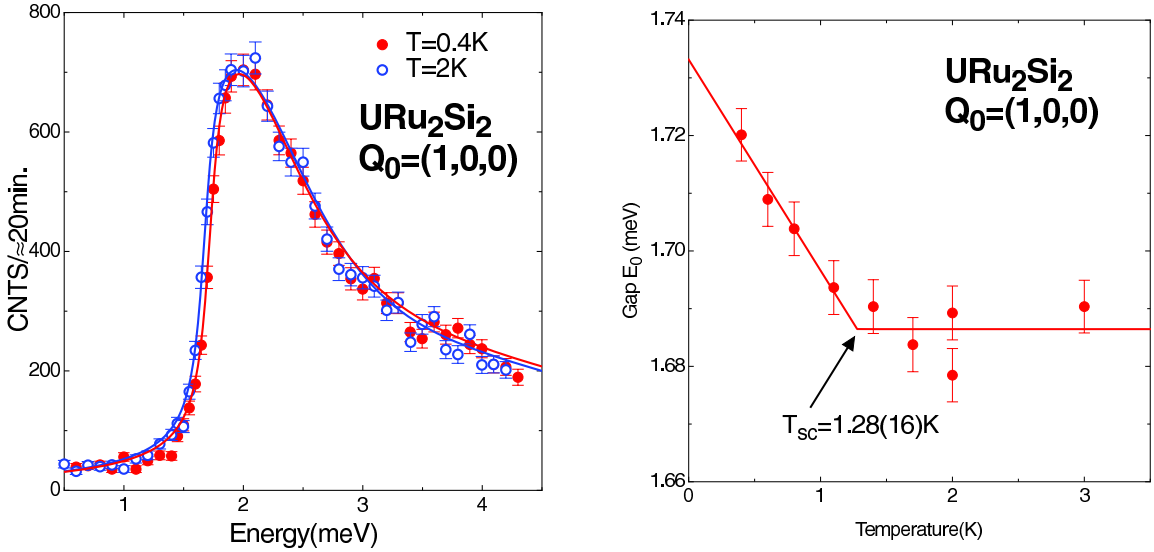

Fig. 3.8 : Left: Energy spectra above and in the superconducting state at $Q_{AF} = (0\,0\,1)$. Right: The temperature dependence of the gap of the excitation at Q_{AF} around the superconducting transition temperature. (Bourdarot et al. 2010a)

group using polarized neutrons (Bourdarot et al. 2010b), show that there is a continuum of magnetic excitations in a broad range of Q vectors up to very high energy $E > 28\,\text{meV}$. This is typical for intermediate valence systems. Accordingly, all attempts to measure crystal field excitations in URu_2Si_2 in the paramagnetic state have failed.

Broholm *et al.* found no transverse excitations with energies up to 400 K. This explains the anisotropy of the susceptibility below 300 K (Broholm et al. 1991).

Superconductivity in URu_2Si_2

Superconductivity coexists with the HO state below 1.5 K. Many measurements on new very high quality crystals in the recent years have contributed to the characterization of the superconducting phase in URu_2Si_2. We will mention only briefly some measurements of the superconducting properties. Only electrons which are left on the Fermi surface during the condensation process at T_0 can form Cooper pairs.

The specific heat transition is seen at about 1.2 K (from the equal entropy fit) and in resistivity it is found at a slightly higher temperature (1.5 K) if the criterion is reduction by half of the resistivity (Hassinger et al. 2008). The transition can have a double or triple step, depending on the sample and its heat treatment (Ramirez et al. 1992). In contrast to the double transition in UPt_3 this is not intrinsic and not present in every sample.

Precise measurements of the excitations around the superconducting transition temperature of our group (Bourdarot et al. 2010a) show that the gap of the excitation at Q_{AF} shifts slightly to lower energies by $\approx 40\,\mu$eV when entering into the superconducting state (see figure 3.8). The role of the excitations for superconductivity in this compound has to be studied further.

The estimated coherence length is $\xi \approx 100\,$Å(Palstra et al. 1986). In good samples, the mean free path exceeds 1000 Å (Brison et al. 1995), and therefore the system is in the

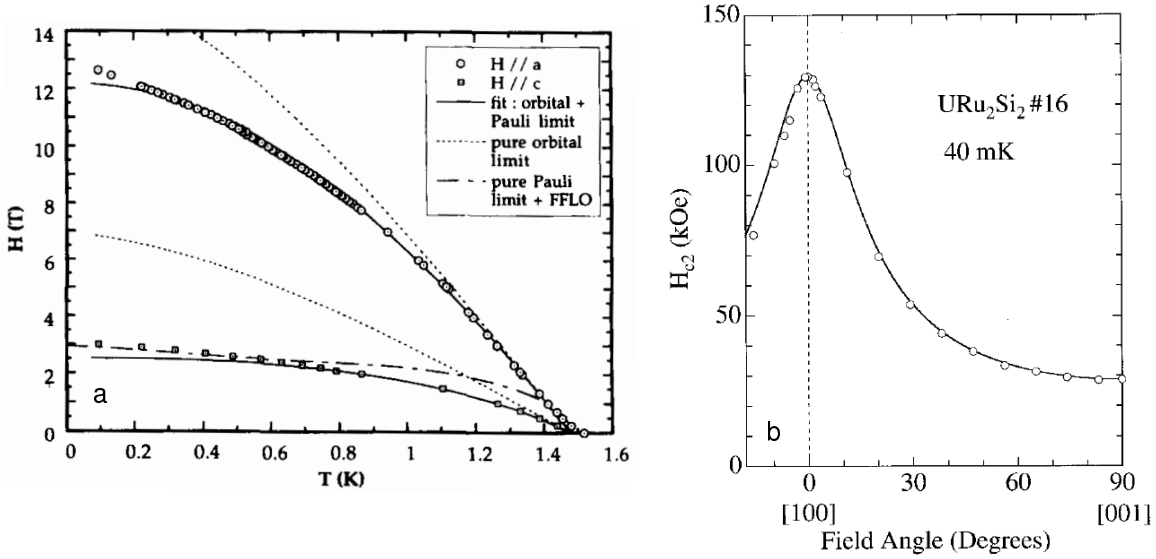

Fig. 3.9 : a) Upper critical field $\mu_0 H_{c2}$ of URu_2Si_2 for $H \parallel$a and $H \parallel$c (Brison et al. 1995). Dashed lines are from pure orbital limit calculations and dashed-dotted lines from BCS- Pauli limit. b) Angular dependence of the upper critical field H_{c2} (Ohkuni et al. 1999). The line is a fit according to formula 3.4.

clean limit. The upper critical field is anisotropic (see figure 3.9) and large (Palstra et al. 1985) with a value of about $H^a_{c2} \sim 13\,\mathrm{T}$ for $H \parallel a$ and $H^c_{c2} \sim 3\,\mathrm{T}$. It can be described taking into account anisotropic orbital and Pauli-limitation in the clean limit (fit line figure 3.9). The angular dependence of H_{c2} both near T_{sc} (but also at low temperature see figure 3.9) can be explained by the angular dependence of the effective masses, assuming that the anisotropy of H_{c2} comes only from the anisotropy of the orbital limit. It is then well described by the formula

$$H_{c2}(\phi) = \frac{H^a_{c2}}{[\cos^2\phi + \epsilon^2 \sin^2\phi]^{\frac{1}{2}}} \tag{3.4}$$

with $\epsilon = \frac{H^a_{c2}}{H^c_{c2}}$. The ratio of ϵ at a constant temperature near T_{sc} gives the ratio of the slopes $\frac{dH_{c2}}{dT}|_{T_{sc}}$. As the slope is set by the magnitude of the superconducting coherence length ξ, the anisotropy directly yields the anisotropy of ξ. In a BCS superconductor, the coherence length at $T = 0$ is set by the Fermi velocity: $\xi_0 = \frac{0.18\hbar v_F}{k_B T_{sc}}$. This implies $\frac{\xi_a}{\xi_c} = \frac{v^a_F}{v^c_F} \approx \sqrt{\frac{m^*_c}{m^*_a}} \approx 3$ implying $m^*_c > m^*_a$.

Looking at the anisotropy of the temperature dependence of the resistivity (Zhu et al. 2009), this is a somewhat surprising result: First measured by (Palstra et al. 1986) and often confirmed afterwards, the charge conductivity in URu_2Si_2 is more than twice larger for a current along the c axis than for a current along the a axis at room temperature. In the Drude-Boltzmann picture, the ratio of conductivities is directly related to the ratio of the Fermi velocities $\frac{\sigma_c}{\sigma_a} = \left(\frac{v^c_F}{v^a_F}\right)^2$. This would imply that the Fermi velocity is larger along the c axis than along the a axis. This is in contradiction to what is obtained from the anisotropy of H_{c2}. We will come back to this paradox later after the determination of the cyclotron masses in the quantum oscillation measurements.

Measurements of the thermal conductivity down to very low temperature on a high quality single crystal (Kasahara et al. 2007) show a residual value in the $T \to 0$ limit. This implies that the superconducting gap contains nodes. With increasing field, this residual value increases first strongly up to a plateau between $0.05\,H_{c2}$ and $0.2\,H_{c2}$ for both field directions (heat current along a axis). For a field along a, the residual value increases up to a value of $\kappa/T = 1.6\,\mathrm{W/K^2m}$ just before falling to the value predicted by the Wiedemann-Franz law above H_{c2}. For a field along c, the value stays the same as at the plateau and then also falls to the value predicted by the Wiedemann-Franz law. The increase of the thermal conductivity (entropy flow) when entering into the superconducting state is surprising. Normally, the heat conduction is smaller in the superconducting state owing to the reduction of the number of quasiparticles carrying heat and the enhancement of the scattering rate by vortices. In URu_2Si_2 the increase of κ/T in the zero temperature limit or rather its small value in the normal state above H_{c2} was explained by the fact that it is a compensated metal (see paragraph 3.1.1) with low carrier density (Adachi and Sigrist 2008). The high magnetoresistance of a compensated metal in a magnetic field leads to a very low thermal conductivity. In the superconducting state, the compensation is violated and therefore the heat transport drastically changed. The large increase of κ/T for very low fields is reminiscent of two band superconductivity as in MgB_2 (Sologubenko et al. 2002) or $PrOs_4Sb_12$ (Seyfarth et al. 2005), when the superconductivity of one band is very quickly suppressed in field due to its smaller gap. The conclusions of the measurements by Kasahara *et al.* about the Fermi surface topology of electron and hole Fermi surface and the superconducting gap structure is based on an old band structure calculation (Ohkuni et al. 1999), which is not in agreement with quantum oscillation measurements (see paragraph 3.1.1) and requires to be revisited. They predict from their measurements interlayer spin singlet pairing of d-wave symmetry in view of the structure of the magnetic correlations appearing under pressure. In-plane singlet pairing is suppressed due to ferromagnetic spin correlations.

Measurements of the angular dependence of the specific heat in a magnetic field show first that for fields in the plane no anisotropy can be detected and second that the increase of the specific heat with field is much stronger for $H \parallel a$ than for $H \parallel c$ (Sakakibara et al. 2008; Yano et al. 2008). This implies an axial symmetry around the c axis of the superconducting gap with nodes $\perp c$ and a full gap $\parallel c$.

Theories for the hidden order parameter

Theoretical models for the hidden order state are quite varied and will not be discussed in detail here. The models can be basically divided into two groups (Amitsuka et al. 2007). In group (A) the order parameter is a magnetic dipole and the antiferromagnetism is an intrinsic property of the hidden order phase. This was the predominant opinion in the early years after the discovery of URu_2Si_2. With the publication of experimental results indicating that the small moment is extrinsic, proposals were published where the order parameter is some other degree of freedom (group (B)). In this case antiferromagnetism is not intrinsic but an additional order parameter.

In the first group we include for example crystalline electric field effects (Nieuwenhuys 1987), dynamically phased order parameter (Bernhoeft et al. 2003), spin density waves (Mineev and Zhitomirsky 2005) or a combination of local and itinerant magnetism (Okuno

and Miyake 1998).

In group (B) are: multipolar orders up to rank 5: quadrupolar ordering (Harima 2010; Ohkawa and Shimizu 1999; Santini and Amoretti 1994), octupolar ordering (Kiss and Fazekas 2005), hexadecapolar ordering (Haule and Kotliar 2009), triakontadipolar ordering (Cricchio et al. 2009): Besides that, there are the following propositions: unconventional density waves (Ikeda and Ohashi 1998), helicity order (Varma and Zhu 2006), orbital antiferromagnetism (Chandra et al. 2002), Jahn-Teller distortion (Kasuya 1997), charge density wave (Balatsky et al. 2009), hybridization wave (Dubi and Balatsky 2010) or fluctuating dipolar order (Elgazzar et al. 2009).

In group (B) two possibilities were discussed over the years: i) The additional hidden order parameter can induce antiferromagnetic order that means as soon as the hidden order parameter is larger than zero for $T < T_0$ the antiferromagnetic order parameter is automatically also different from zero. In this case the system is ordered homogeneously with two coexisting orders. This is the case, when the two phases in the phase diagram are not completely separated. ii) The second order phase is separated from the antiferromagnetic phase and the order parameters are not coupled. Here the volume is inhomogeneously divided between the two phases. This is now the predominant idea after the well established pressure phase diagram with a first order transition line between the HO and the AF phase. As the pressure measurements played an important role for the most recent theoretical propositions of the order parameter, I will explain in more detail these theories in the pressure section (paragraph 3.1.2).

In each of these theories the degree of localization of the $5f$ electrons and therefore their participation in the Fermi surface can be different. In the case, where the Fermi surface and the quantum oscillation frequencies are calculated, SdH measurements can decide if a theory is compatible. This question will be discussed after the presentation of the results which will be compared to existing band-structure calculations.

Suppression of the hidden order state in high magnetic fields

The reaction of the HO to a magnetic field depends on the direction in which the field is applied. The HO state is very stable for fields $H \parallel a$ but the transition temperature is suppressed for $H \parallel c$. As shown in figure 3.10c, the HO phase is completely suppressed at a field of 35 T (de Visser et al. 1986; Kim et al. 2003a). Around this field, a cascade of metamagnetic transitions (DeBoer et al. 1986; Sugiyama et al. 1999) occur leading to a rich phase diagram as seen in figure 3.10a (Kim et al. 2003b). Figure 3.10b shows the exponent n of a $\rho_0 + AT^n$ fit showing that a T^2 behavior is recovered in the polarized phase (IV). The transitions have also been detected by magnetoresistance (Kim et al. 2004), ultrasonic experiments and ac susceptibility (Suslov et al. 2003), specific heat (van Dijk et al. 1995) and thermoelectric power (Levallois et al. 2009). With the suppression of the HO phase the carrier number goes back to its value at zero field above T_0.

The behavior of gap energies of the magnetic excitations with magnetic fields applied $H \parallel c$ is shown in figure 3.11 (Bourdarot et al. 2003a). The gap of the excitation at Q_{inc} depends only very little on applied fields whereas the gap of the excitation at Q_{AF} increases with field. An extrapolation of the field dependence of the two gaps indicates a crossing point at $H \approx 35$ T near the critical field of suppression of the HO state. The gap

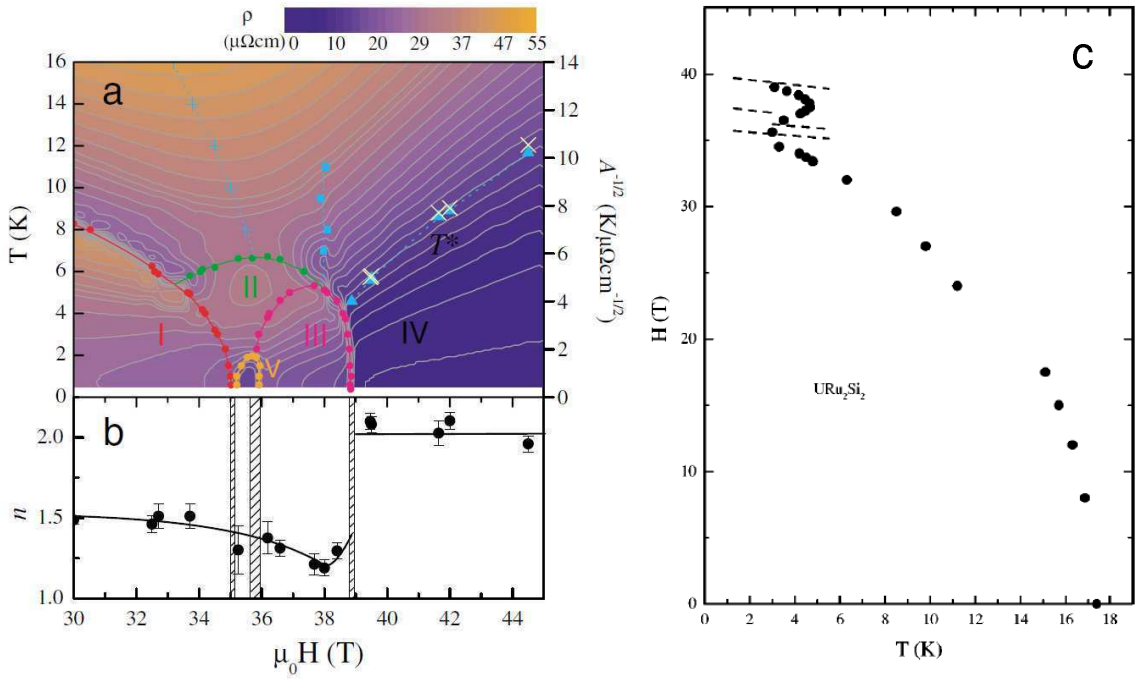

Fig. 3.10 : a) Phase diagram in field of URu_2Si_2 near the critical field (Kim et al. 2003b). Various phases can be distinguished. The precise explication of the points and lines can be found in reference (Kim et al. 2003b). b) The exponent n of the $\rho_0 + AT^n$ fit (Kim et al. 2003b). c) Phase diagram of URu_2Si_2 in field determined by specific heat (Kim et al. 2003a).

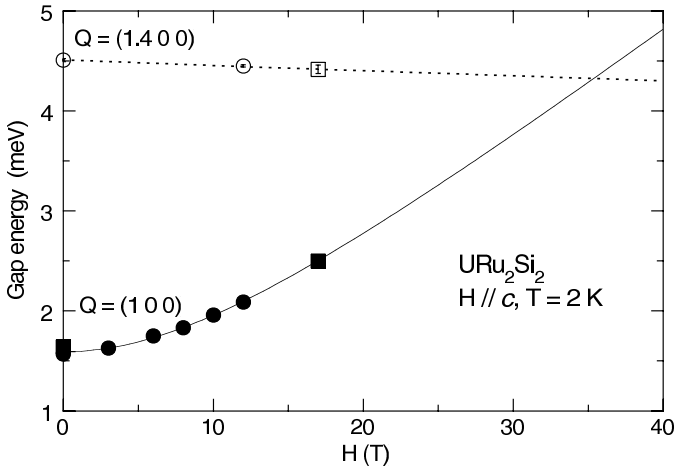

Fig. 3.11 : Field dependence of the energy gaps of the magnetic excitations in URu_2Si_2 (Bourdarot et al. 2003a).

	α band		β band		γ band			
field axis	freq. (kT)	$m^\star$ (m_e)	freq. (kT)	$m^\star$ (m_e)	freq. (kT)	$m^\star$ (m_e)	source	remark
c	1.09	12.1	0.41	20 ± 5			Bergemann	
c	1.05	13	0.42	25	0.19	8.2	Ohkuni	
c	1.05	13.4	0.45	26.3	0.2	13.3	Aoki	
c	1.0	13	0.5	25			Shishido	17-24 T
c	0.85	17.1	0.59		0.223	14.2 ± 0.4	Jo	25-29 T
a	1.26	9.2 ± 0.1	0.3	16 ± 3	0.15		Bergemann	γ in some directions
	1.2	8.3 ± 0.9	0.07	5.8 ± 0.6			Keller	10° from a

	δ band							
c	0.59						Jo	25-29 T

	ϵ band			$\gamma\prime$ band			
c	1.3	2.7		0.25	27	Shishido	17-24 T

Table 3.1: Oscillation frequencies and cyclotron masses of existing quantum oscillation measurements (Aoki et al. 2010; Bergemann et al. 1997; Jo et al. 2007; Keller et al. 1998; Ohkuni et al. 1999; Shishido et al. 2009).

seen in the exponential temperature behavior of the resistivity decreases in field $H \parallel c$ (Schmidt 1993).

To summarize, the application of a magnetic field $H \parallel c$ suppresses the HO transition and a polarized heavy fermion state is induced with a large carrier density.

Previous quantum oscillation results in the hidden order phase

As URu_2Si_2 is a compensated semimetal, SdH oscillations have a relatively high amplitude and can be easily observed (Shoenberg 1984). This is similar to bismuth, the first metal in which quantum oscillations have been observed.

In the following description of results of de Haas-van Alphen and Shubnikov-de Haas measurements, we take the notation for the Fermi surface branches by Ohkuni *et al.* (Ohkuni et al. 1999) even when the publications use a different notation.

All the measurements have in common that only small Fermi surface pockets are detected. A summary of the results by the different groups is given in table 3.1.1. The volume of the pocket α is smaller than 5 % of the volume of the antiferromagnetic BZ (Aoki et al. 2010; Keller et al. 1998). Its Fermi vector assuming a spherical Fermi surface $k_F = 0.18\,\text{Å}^{-1}$ agrees well with the ARPES results. All the other pockets detected at low fields are even smaller. The volume of these Fermi surface pockets corresponds to a carrier number of ≈ 0.03 per unit cell, the same value as found by Hall measurements assuming a single band. The angular dependence of all the detected pockets is weak (no divergence of the frequency) (Bergemann et al. 1997; Keller et al. 1998; Ohkuni et al. 1999; Shishido et al. 2009) and therefore it is concluded that there are no open orbits. Transverse magnetoresistance measurements for all angles in high fields confirm this point

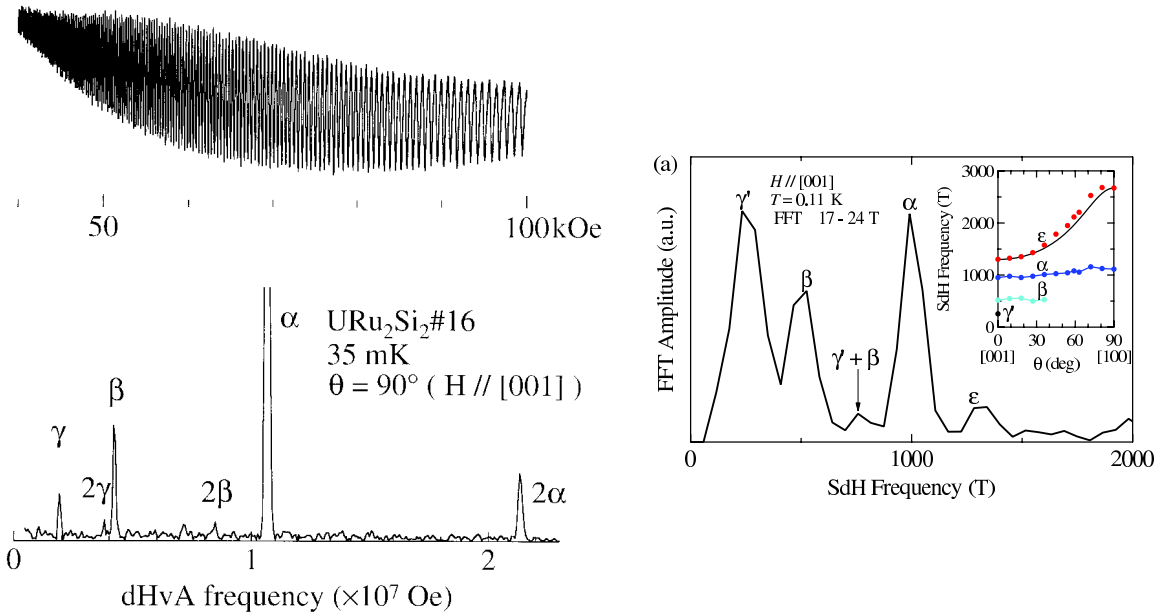

Fig. 3.12 : Left side: DHvA oscillation and the corresponding FFT spectrum for $H \parallel c$ (Ohkuni et al. 1999). 10 kOe= 1 T. Right side: FFT spectrum for high fields (Shishido et al. 2009). The resolution is much worse. The inlay shows the angular dependence of the detected branches.

(Ohkuni et al. 1997, 1999).

The measurements with the best resolution are achieved by Ohkuni et al. (1999). They performed measurements on very high quality crystals (RRR = 255). For $H \parallel c$ they report Dingle temperatures of 0.035 K, 0.045 K and 0.11 K for branches α, β and γ and mean free paths of 5500 Å, 1400 Å, 1200 Å for the same branches. Oscillations are detected for fields as low as 4 T. In low fields, the oscillations are faster than in high field (periodic in 1/H). The possibility to observe many oscillations leads to a good resolution in the FFT. The oscillations at 35 mK and the obtained FFT spectrum from their measurements for $H \parallel c$ is shown in the left figure 3.12. The branches α, β and γ are clearly resolved and even the second harmonic of each branch is visible. The α oscillation is predominant. For this branch they detect up to 6 harmonics. They are therefore sensitive to a branch with a mass of around $60\,m_e$. However, when calculating the γ value from these measurements, only a small percentage (15 %) of the value determined by specific heat is obtained. Therefore, there must be some missing bands which are not observed in the experiment. The amplitude of the α branch becomes zero 16 times when turning the field in the $a-c$ plane, due to the angular dependence of the mass m_α, which leads to zeros of the spin factor R_S. Taking this into account, the value of the purely Ising g_z-factor can be estimated to $g_z = 2.6$ (Silhanek et al. 2006).

The de Haas-van Alphen frequency is the same in the normal and the superconducting mixed state but the oscillations are damped and the cyclotron mass decreases in the superconducting state (Ohkuni et al. 1999).

Recent measurements on a new very high quality crystal (Shishido et al. 2009) ($RRR > 500$) down to ≈ 100 mK can only detect oscillations in fields far above 10 T. This might be due to the noise level in their high field measurements. The resolution of their FFT

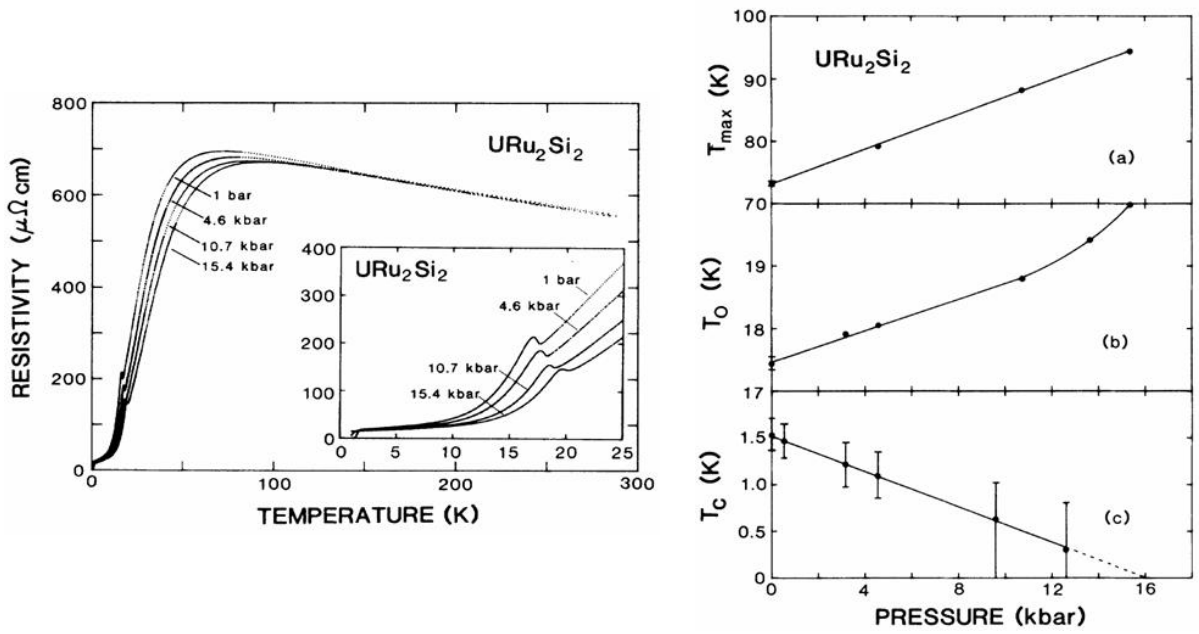

Fig. 3.13 : Left side: Temperature dependence of resistivity of URu_2Si_2 for the pressures 0.1 GPa, 0.46 GPa, 1.07 GPa and 1.54 GPa (McElfresh et al. 1987). Right side: Pressure phase diagram from these measurements(McElfresh et al. 1987).

spectra is consequently quite bad (see the right figure 3.12). For fields above 17 T, they are able to detect an additional elliptic branch ϵ with low mass. This branch cannot account for the missing electronic specific heat at low temperature. The authors link the appearance of this oscillation to a signature in the magnetoresistance and the Hall resistivity at 22 T, a sign of a new phase within the HO phase.

Other high field measurements above 25 T (Jo et al. 2007) report an additional frequency δ. However, their resolution is even worse than in reference (Shishido et al. 2009).

3.1.2 URu_2Si_2 under pressure

Hidden order versus antiferromagnetism

Measurements under pressure shed new light on the hidden order transition by comparing the HO with the pressure induced AF phase. The HO phase is stabilized under hydrostatic pressure which is manifested by an enhancement of the transition temperature T_0 (DeBoer et al. 1986; Iki et al. 1992; McElfresh et al. 1987). The temperature dependence of resistivity under different constant pressures and the pressure phase diagram established from these early measurements are shown in figure 3.13. T_0 slowly increases up to $p \sim 1.4$ GPa (= 14 kbar) and then quickly increases. The temperature of the maximum also increases with pressure, i.e. the coherence temperature increases with decreasing distance between the U atoms, and the superconducting transition temperature decreases until $\sim$ 1.2 GPa. When normalized to the maximum temperature and maximum resistivity, the different curves coincide accurately down to T_0. Hence the mechanisms responsible for the temperature dependence stay approximately the same under pressure. Remarkably the typical nesting shape of the resistivity anomaly at T_0 is

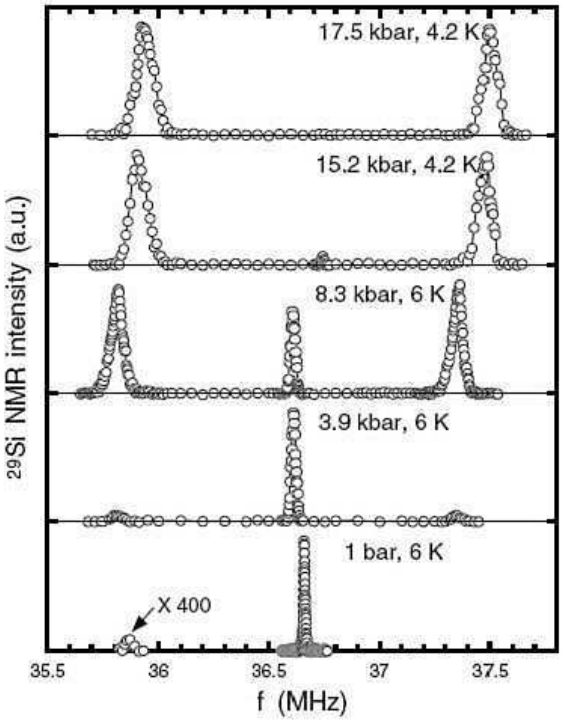

Fig. 3.14 : NMR spectra of URu_2Si_2 for different pressures (Matsuda et al. 2003) at low temperature. The frequency of the central resonance line is slightly shifted for different pressures because the field in which the spectra were taken varied between the measurements.

resistant to pressure.

Amitsuka *et al.* observed in 1999 a large moment antiferromagnetic phase emerging under hydrostatic pressure (Amitsuka et al. 1999). The neutron scattering intensity of the magnetic Bragg peak increased gradually up to a large saturated value for the moment of $m \approx 0.4\,\mu_B$ at $p \gtrsim 1.4\,\mathrm{GPa}$. This value would account for the entropy change at T_0 at zero pressure. From ac calorimetric measurements it is known that the entropy change stays approximately constant with pressure.

In later pressure experiments with better samples and pressure conditions, the intensity of the magnetic Bragg peak jumps steplike to the high pressure value (Amitsuka et al. 2007; Bourdarot et al. 2003a; Niklowitz et al. 2010) at a critical pressure of around 0.5 GPa.

High pressure ^{29}Si-NMR (Matsuda et al. 2001)(nuclear magnetic resonance) and μSR (Amato et al. 2004)(muon spin resonance) measurements indicate that it is not the magnetic moment but the volume fraction of the antiferromagnetic phase which increases with pressure at the expense of the hidden order phase. In contrast to neutron scattering, where a volume average is measured (scattering intensity $I \propto m^2 V_{af}$) these two methods can distinguish the volume fraction and the ordered moment. At low temperature with increasing pressure, the frequency of the antiferromagnetic resonance lines does not change. Only their intensity grows (see the two outer peaks in figure 3.14). This means that the local field at the Si sites created by the uranium moments is constant, only the number of Si atoms located in field and consequently the magnetically ordered volume grows. Over a wide pressure range (0.1 GPa - 1.52 GPa) the paramagnetic phase (seen as the line in the middle) is also present next to the antiferromagnetic phase but the two phases are locally separated.

From thermal expansion measurements Motoyama et al. (2003) found a sharp, steep transition line between the hidden order and the large moment antiferromagnetic phase (see figure 3.15). This is in contrast to the quite large pressure range, in which the vol-

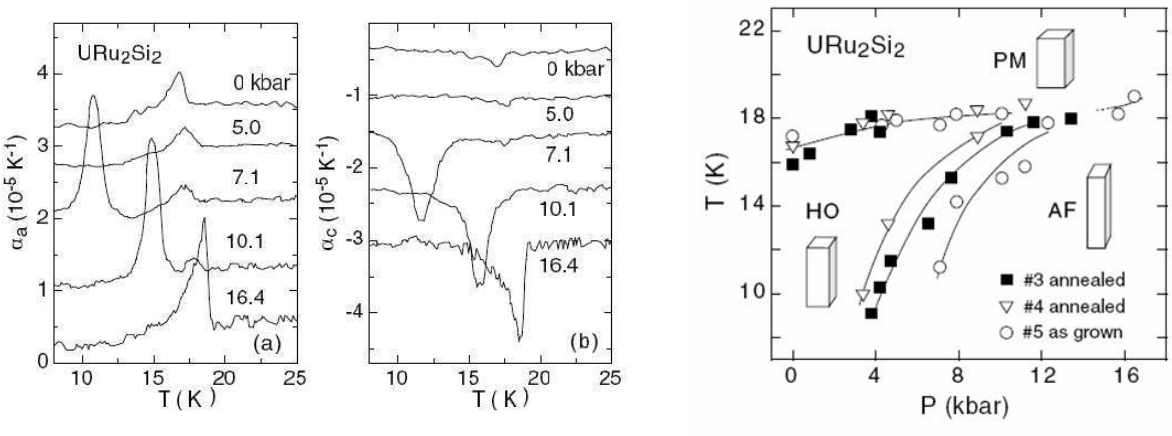

Fig. 3.15 : Left side: Temperature dependence of the thermal expansion coefficient of URu_2Si_2 in the two crystal directions for sample #5 at different pressures. Right side: Pressure phase diagram of URu_2Si_2 from thermal expansion from three different samples. The transition line between hidden order and antiferromagnetism is measured for three different samples. (Motoyama et al. 2003)

ume of the antiferromagnetic phase increases in first measurements by Amitsuka et al. (1999) and in NMR by Matsuda et al. (2003). Therefore, they suggested a first order phase transition in the pressure phase diagram and ascribed the large transition pressure ranges in the neutron and NMR measurements to inhomogeneous pressure in those measurements. They measured the thermal expansion with the strain gauge method. The data at zero pressure corresponds nicely to the data by de Visser et al. (1986) who used a capacitive method. In the data presented in figure 3.15 at 0 GPa and 0.5 GPa only the transition at T_0 is visible. With pressure it moves to higher temperatures. The second peak at T_x is very clearly coming up at $p \geq 0.71$ GPa and also shifts to higher temperatures. Whereas the transition at T_0 attenuates with pressure, the new transition seems to survive to higher pressures. Its shape seems to change from Gaussian like to a mean field like discontinuous jump for 1.64 GPa when only one transition is present. The c/a ratio increases at the transition to large moment AF. The authors remark that the critical pressure depends on the sample and measurement conditions. This has been confirmed by various measurements in different pressure media (Amitsuka et al. 2008; Aoki et al. 2009a; Butch et al. 2010; Motoyama et al. 2008; Niklowitz et al. 2010). The most hydrostatic conditions were recently achieved with liquid He and the critical pressure in these conditions seems to be a little higher $P_x \approx 0.8$ GPa (Butch et al. 2010).

The detailed investigation of the signature of the transition at T_0 in resistivity and specific heat up to pressures of 2.5 GPa helped to settle the question on the topology of the phase diagram of URu_2Si_2 (Hassinger et al. 2008). In these studies, the transition line between HO and AF could be detected in both resistivity and ac calorimetry, observed as a round anomaly in the curves at 1.1 GPa in figure 3.16 on the left. The phase diagram determined from these measurements is shown on the right side of the same figure. Even though the pressure steps are discrete, the HO and AF phases seem well separated, allowing a conclusion on the symmetry of the HO and AF order parameters. Earlier neutron experiments had left open the possibility that the transition line between HO and AF ends in a critical end point (Bourdarot et al. 2004). In this case, the order parameters

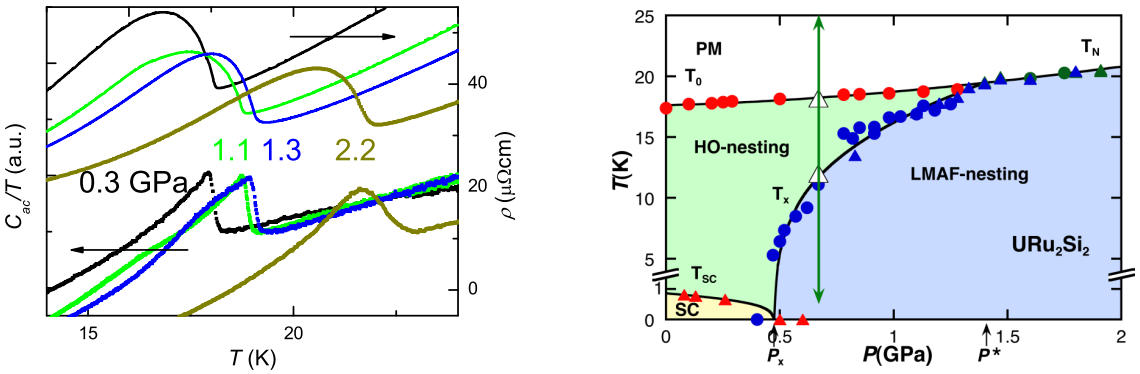

Fig. 3.16 : Left side: Temperature dependence of the resistivity and ac calorimetry of URu_2Si_2 for different pressures (Hassinger et al. 2008). Right side: Pressure phase diagram of URu_2Si_2 from these measurements. The green line indicates the pressure, where the neutron scattering measurements have been carried out (Villaume et al. 2008).

of both phases are linearly coupled and must have the same symmetry. However, it is now confirmed that the phase regions are separated. In this case completely independent symmetries for the order parameters in each phase are possible (Mineev and Zhitomirsky 2005), separated by a first order transition line. However, the anomalies at the transition temperature are very similar in both phases. In resistivity, the qualitative shape of the anomaly stays the same at 2.2 GPa far in the AF state. Therefore, the reconstruction of the Fermi surface stays the same in both phases. The specific heat anomaly is sharp when entering from the paramagnetic state into the HO state but round when entering into the AF state. This is an indication that the transition in the AF phase is more sensitive to pressure inhomogeneities. Even though these are only qualitative measurements, it is possible to claim that the size of the anomaly and therefore also the entropy change stay approximately the same in both phases.

Magnetization measurements under pressure reveal a decrease of dM/dT (Pfleiderer et al. 2006) and susceptibility (Motoyama et al. 2010) for $H \parallel c$ when going from the HO to the AF state.

Subsequently, our group carried out elastic and inelastic neutron scattering experiments at a fixed pressure of $P = 0.67$ GPa as a function of temperature, in order to measure the Bragg peak and the magnetic excitations in the three phases (paramagnetic at high temperature, HO at intermediate temperatures and AF at low temperatures). The pressure is shown as a green line in the phase diagram in figure 3.16. Simultaneous thermal expansion measurement helped us to determine the phase boundaries in the present sample and pressure condition as the critical pressure can change from one measurement to another. Figure 3.17 shows the two excitations in the three phases. As at ambient pressure, the excitations become very clear below T_0, but when entering into the AF phase, they behave differently: The excitation at Q_{AF} disappears completely whereas the gap energy of the excitation at Q_{inc} jumps to a higher value. Therefore, Q_{AF} is a signature of the HO phase, it only exists in this phase. The integrated intensity of the excitation decreases when lowering the temperature in the AF phase in the same way as the intensity of the AF Bragg peak increases. Hence, one interpretation is that the spectral weight is shifted to zero energy. We also proved that the temperature dependence of the integrated intensity of this excitation follows a mean-field like behavior, supporting

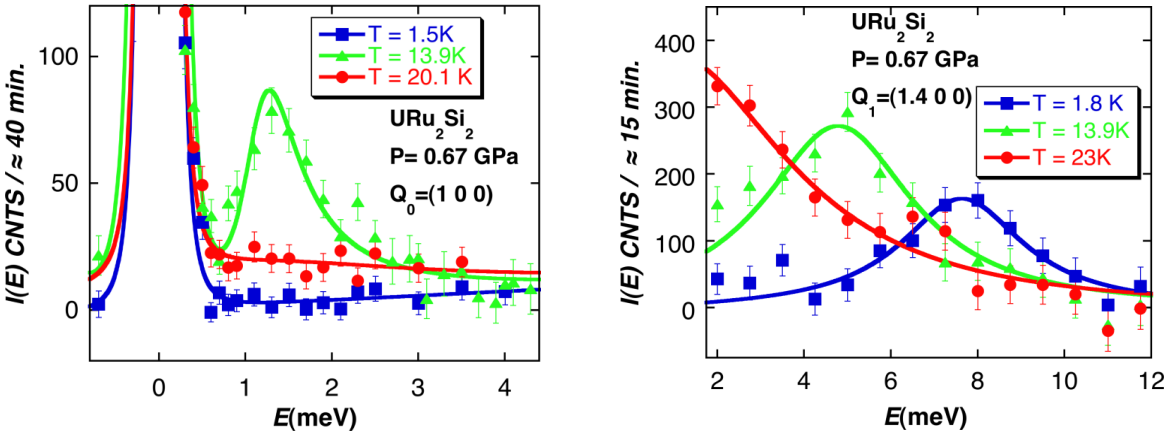

Fig. 3.17 : Temperature dependence of the energy spectra at Q_{AF} (left) and Q_{inc} (right) at 0.67 GPa (Villaume et al. 2008).

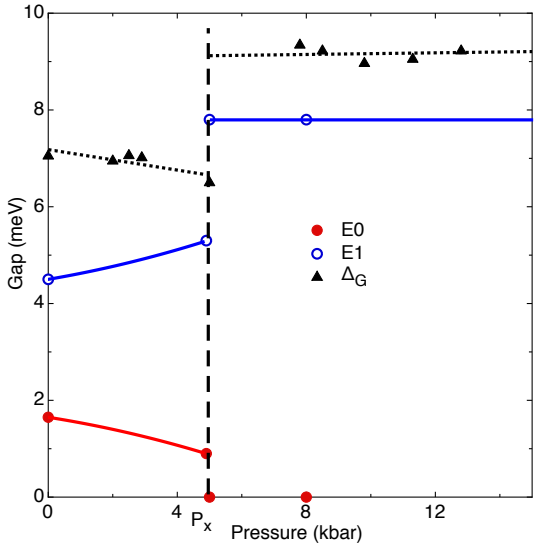

Fig. 3.18 : Pressure dependence of the gaps of the excitations and the charge gap determined by resistivity (Bourdarot et al. 2010b).

the idea that it reflects the order parameter in the HO phase (Bourdarot et al. 2010b).

Figure 3.18 shows the pressure dependence of the energy gaps of the two excitations. Additionally, the gap energy Δ_G obtained from the exponential behavior of the resistivity is also plotted. Δ_G increases by around 20 % in the AF phase (Hassinger et al. 2008; Motoyama et al. 2008) which is the same as Δ_{inc}.

Yokoyama *et al.* carried out neutron scattering measurements under uniaxial stress (Yokoyama et al. 2005). The ordered moment is very sensitively for pressure and increases for pressure applied along $(1, 0, 0)$ and $(1, 1, 0)$ but not for pressure along $(0, 0, 1)$. Bakker *et al.* also proved that T_0 increases only under uniaxial stress $\sigma \parallel$a and decreased for $\sigma \parallel c$ (Bakker et al. 1992). The ratio $\frac{c}{a} \equiv \eta$ is the key parameter which drives the transition from hidden order to antiferromagnetism. Its critical value η_c is very small. This is proposed to be the mechanism to explain why the antiferromagnetic phase can appear locally where lattice defaults cause internal strains with values of $\eta > \eta_c$ even at ambient pressure. In this case the antiferromagnetism measured by neutron scattering at ambient pressure would be parasitic and have a very small volume fraction ($\sim 0.6\,\%$) in the non-magnetic hidden order phase. In the same way, small volume fractions of the

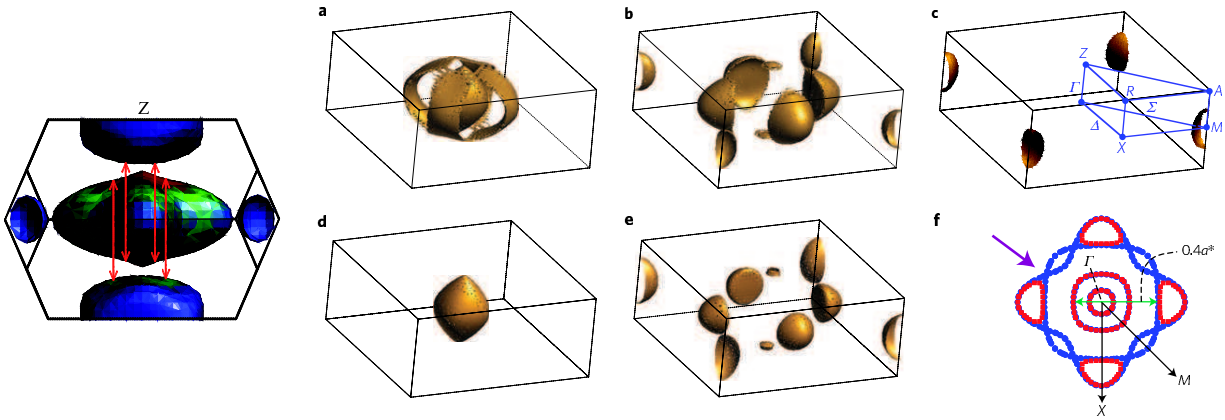

Fig. 3.19 : Left: The Fermi surface in the paramagnetic state of URu_2Si_2 (Oppeneer et al. 2010). The red arrows indicate a possible nesting vector $Q = (0\ 0\ 1)$. Right: a-c) The same Fermi surface, but folded in the simple tetragonal BZ. c-e) Fermi surface in the AF phase f) cut through the main Fermi surface sheets in the Γ plane, blue for paramagnetic and red for AF Fermi surface (Elgazzar et al. 2009). Here, the green arrow shows a possible nesting vector $Q = (1 \pm 0.4\ 0\ 0)$ and the violet arrow indicates a "hot spot".

HO phase would survive in the AF phase.

By Larmor diffraction measurements, the distribution of the lattice parameter of the sample has been determined (Niklowitz et al. 2010). The measurements confirm that the distribution of the ratio of the lattice parameter η can explain the small moment appearing at low pressure in the HO phase.

Recent electronic structure calculations in HO phase and AF phase

So far, experiments under pressure support a theory with two order parameters: the HO parameter and the AF order parameter. Possibilities for the HO parameter are given in the end of paragraph 3.1.1. Two recent theories take into account the similarities of the HO phase and the AF phase and will be explained a little more detailed here.

Elgazzar *et al.* calculate the band structure of the paramagnetic state and the pressure induced AF state (Elgazzar et al. 2009; Oppeneer et al. 2010) by different LDA methods. The paramagnetic Fermi surface is given in the body centered tetragonal BZ (left side of figure 3.19) and also in the simple tetragonal BZ (figure 3.19a-c, a cut in the Γ plane in f(blue)). In figure 3.19d,e,c (and again a cut in the Γ plane in f(red)) the FS of the AF phase is shown. They find possible nesting vectors $Q = (0\ 0\ 1)$ in the paramagnetic state (see the red arrows in the left side of figure 3.19) and $Q = (1 \pm 0.4\ 0\ 0)$ in the AF state (see the green arrow in figure 3.19f). The specific feature of URu_2Si_2 is that in the paramagnetic band structure drawn in the AF BZ, there are "hot spots" (see the violet arrow in figure 3.19f), i.e. spots where two bands cross each other precisely at the Fermi energy, which leads to a substantial gap opening at the Fermi surface in the ordered state. The occupation number of the $5f$ level is 2.7, an indication of rather itinerant $5f$ electrons in agreement with recent spectroscopic measurements (Jeffries 2010). In this model, the proposal for the HO parameter is a fluctuating dipole moment. The time average of the measured moment is zero however it predicts an order parameter-like temperature dependence of the Q_{AF} excitation which has been confirmed experimentally

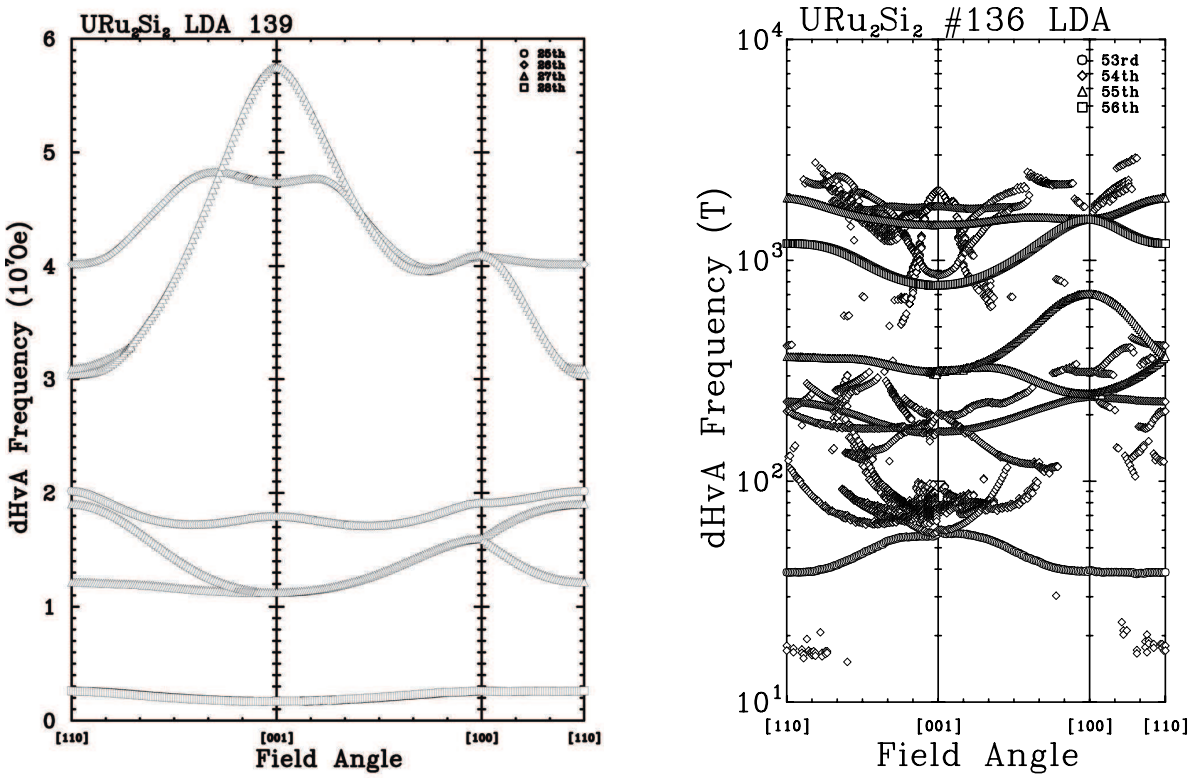

Fig. 3.20 : Angular dependence of the quantum oscillation frequencies in the paramagnetic state (group 139, left) and the same, but folded (group 136, right) without taking into account their proposed quadrupolar ordering, which is suspected to stabilize the 136 symmetry. Note that 10^7 Oe = 10^3 T (Harima 2010).

(Bourdarot et al. 2010b). Another prediction was an increase of the gap by $\approx 40\,\%$ when going from the HO state to the AF state and $\Delta \propto |M_z|$ and $\Delta(t) \approx \Delta_0\,|\cos(\omega t)|$. The Fermi surface in the two phases is almost the same. In both phases, the body-centered tetragonal symmetry of the paramagnetic state and the time reversal symmetry are broken (symmetry group 129).

Calculations by Harima (2010) using LDA give very similar results to these calculations in the paramagnetic state (symmetry group 139) in the itinerant case and also for the localized FS. Following group symmetry considerations for the HO state, he calculates the folded paramagnetic itinerant FS in the tetragonal symmetry group 136 without taking into account an order parameter. He finds a similar folded FS as in figure 3.19a-c, however slightly more complicated. Hence, in the angular dependence of the oscillation frequencies (right side of figure 3.20) there are several additional frequencies which are not observed in experiments.

In the angular dependence in the paramagnetic state (left side of figure 3.20) most of the frequencies are much higher and do not correspond to the observed frequencies.

A calculation method treating relativistic effects better but less the interactions (muffin potential) by Yamagami et al. (2010) results in a completely different Fermi surface in the AF state (see figure 3.21). Only three frequencies exist in this calculation but their angular dependence is in reasonable agreement with the frequencies observed by Ohkuni et al. (1999).

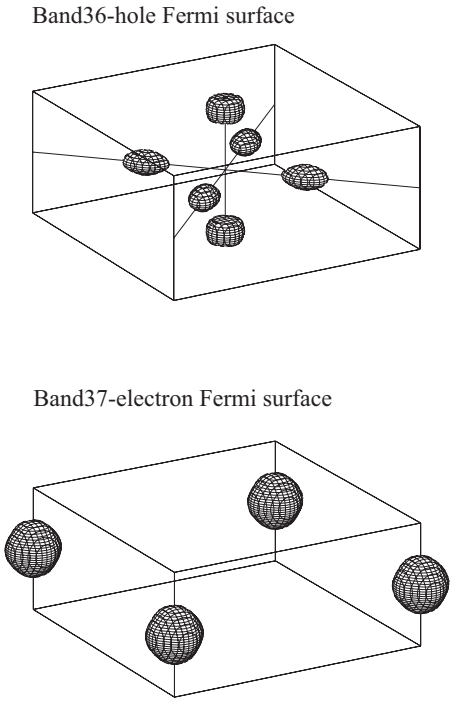

Fig. 3.21 : Fermi surface in the AF state of URu_2Si_2 (Yamagami et al. 2010). Only three bands exist in this calculation.

Very different DMFT calculations by Haule and Kotliar (2009) find a ground state of the system with $5f^2$ configuration with a total angular momentum of $j = 4$ and two low lying crystal field levels separated by $\Delta = 35\,\mathrm{K}$. Below a coherence temperature $T^\star$, the two low lying levels of the ground state seem degenerate and the Kondo effect develops, leading to a hybridization of the f and conduction electrons. For $T < \Delta$ the Kondo effect is partially arrested because the crystal field splitting induces a partial gapping at the Fermi surface. Only a small fraction of f spectral weight is left at the Fermi surface. Nevertheless an effective mass of over $200\,m_e$ is calculated at $T = 19\,\mathrm{K}$. The U $5f$ occupation is near 2 in this case, meaning that the f electrons are almost localized. The Fermi surface is also the same in both ordered phases. Figure 3.22 shows a cut through the calculated FS in the Γ plane in the paramagnetic state (b) and the folded FS in the AF state (c). The FS in the paramagnetic state of this DMFT calculation is similar to the FS obtained from DFT band structure calculations in the paramagnetic state with localized $5f$ electrons (shown in figure 3.22a) (Harima 2010; Haule and Kotliar 2009). The similarity can easily be seen when comparing the FS cut in the Γ plane of the presented Brillouin zone in (a) with the cut with (b). The order parameter Ψ is then the Hubbard operator which measures the excitonic mixing between the two lowest lying U-$5f$ singlets. This order parameter has a unique property. It is a complex order parameter and the idea is that in each ordered state at low energy (HO or AF state) either the real or the imaginary part is zero. For the HO state, $\Im(\Psi) = 0$, the order parameter is a hexadecapole order parameter without time reversal symmetry breaking, in the AF state $\Re(\Psi) = 0$ the order parameter is the magnetization along the z axis with time reversal symmetry breaking. In both phases, the body centered tetragonal symmetry is broken and the ordering vector is Q_{AF}.

The Fermi surface in these proposals for the HO parameter is different, and measurements of the Fermi surface can give evidence in favor of one theory.

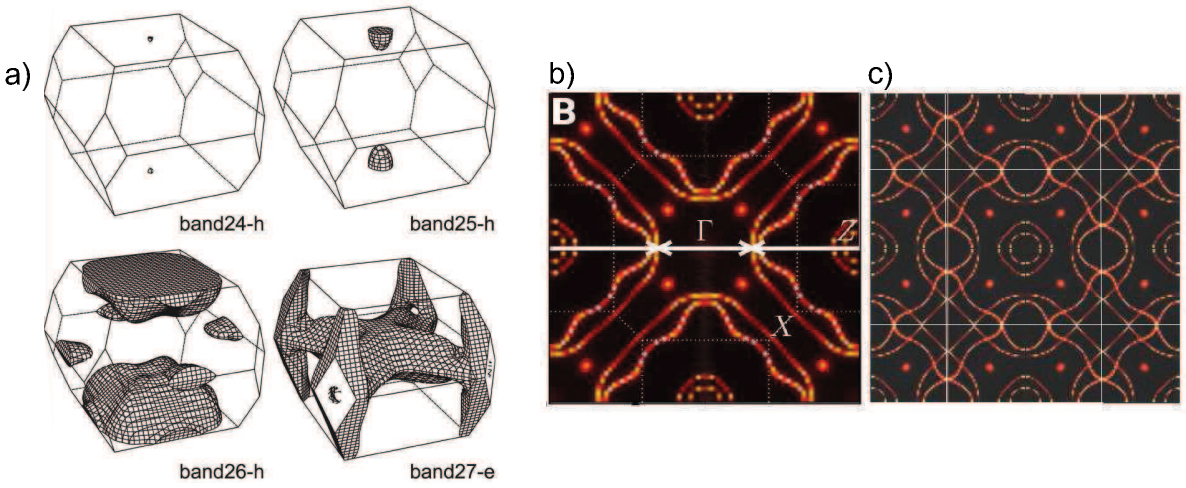

Fig. 3.22 : a) The Fermi surface of URu_2Si_2 with $5f^2$ configuration in the paramagnetic state (Harima 2010). Here, the $5f$ electrons are localized and do not take part in the Fermi surface. b) A cut through the Fermi surface calculated by DMFT in the Γ-plane in the bct BZ and c) in the tetragonal (folded) BZ (Haule and Kotliar 2010).

Pressure and magnetic field

Neutron scattering and thermal expansion measurements under pressure and in magnetic field, carried out by our group reveal the three dimensional phase diagram presented on the left side of figure 3.23. At a pressure above the critical pressure, where the ground state is the AF state, this phase is suppressed with an applied magnetic field and the HO state is restored (Aoki et al. 2009a). The HO phase itself is destroyed at much higher fields, similar to ambient pressure (Jo et al. 2007, 2008). The critical field for suppression of the AF phase increases strongly with pressure (Aoki et al. 2009a), whereas the critical field for suppression of the HO increases slightly with pressure (Jo et al. 2007, 2008). With the re-entrance of the HO state under pressure in field, the magnetic Bragg peak is suppressed (see the right side of figure 3.23) and the magnetic excitation at Q_{AF} is recovered, a microscopic proof that the HO state is recovered (Aoki et al. 2009a). Previous magnetization measurements under pressure in high magnetic fields already showed a splitting of the transition temperature when T_x is suppressed and T_N (Pfleiderer et al. 2006).

Doping with small amounts of Rh for Ru has a similar effect as pressure on URu_2Si_2 (Bourdarot et al. 2005b; Yokoyama et al. 2005, 2007). A doping of 2 % Rh shrinks the lattice and induces a bulk AF phase at low temperature $T_N = 8\,\mathrm{K}$. The change of electron contribution however leads to a decrease of T_0 to 14 K and a strong decrease in the strength of the specific heat anomaly (Baek et al. 2010; Bourdarot et al. 2003b). Also, the behavior of the magnetic excitations is similar as under pressure (Yokoyama et al. 2005, 2007). This aspect will not be discussed further here.

Superconductivity under pressure

As a last point in our description of previous experimental results we examine the pressure dependence of the superconducting transition. Concerning this question, different

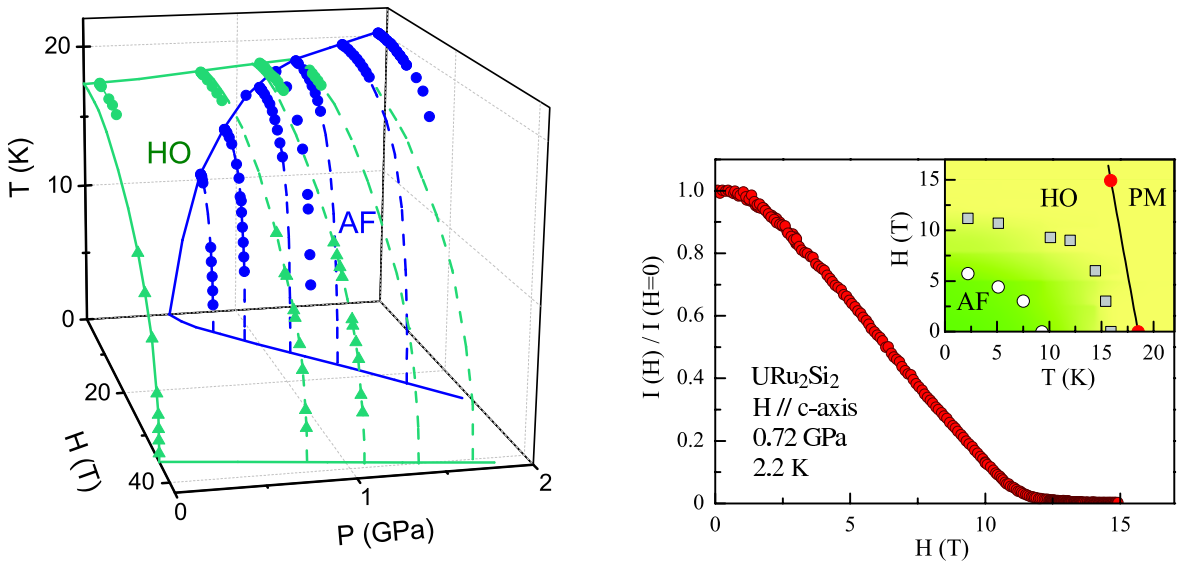

Fig. 3.23 : Left: The three dimensional phase diagram in pressure and magnetic field of URu_2Si_2. At a fixed pressure $P = 0.72\,\mathrm{GPa}$ the intensity of the magnetic Bragg peak as a function of field. Inlay: the phase diagram in field at this pressure. (Aoki et al. 2009a)

measurement techniques give different results. Uemura *et al.* show that superconducting transition measured with ac-susceptibility is abruptly suppressed at $p \sim 0.5\,\mathrm{GPa}$ (Uemura et al. 2005). Because this is the pressure where antiferromagnetism sets in they claim that superconductivity competes with the large moment antiferromagnetism. On the other hand resistivity measurements (Hassinger et al. 2008; Jeffries et al. 2008; McElfresh et al. 1987; Schmidt 1993) show that the superconducting transition is indeed slowly suppressed with pressure but observed up to $\sim 1.2\,\mathrm{GPa}$ (see figure 3.13), a pressure far in the antiferromagnetic phase. This question could be finally settled by specific heat measurements (Hassinger et al. 2008). They imply a suppression of the superconducting state at the same pressure, where the AF phase is induced. The explanation is again the distribution of the lattice parameters in the sample, inducing HO droplets in the AF phase Niklowitz et al. (2010). Therefore superconductivity exists only on inhomogeneous paths through the sample in the antiferromagnetic phase, inducing a short through the sample.

Possible doubling of the unit cell in both HO and AF

The doubling of the unit cell which occurs upon entering the AF phase could explain the reconstruction of the Fermi surface: The BZ becomes smaller by a factor of two and this leads to band folding. Three experimental observations indicate that a band folding also happens in the HO state:

- The reconstruction of the Fermi surface observed in resistivity is the same for all pressures.
- The significant wave vector of both HO and AF phases is Q_{AF}.

- De Haas-van Alphen experiments under pressure, where only the α light branch could be followed, don't show any abrupt changes of the Fermi surface at low temperature up to $p \approx 1.8\,\mathrm{GPa}$ (Nakashima et al. 2003).

As only very small parts of the Fermi surface have been observed under pressure, our aim is to compare all the Fermi surface branches in the HO phase and the AF phase.

3.2 Fermi surface studies at ambient pressure

We have measured the magnetoresistance of two samples of URu_2Si_2 (sample 1 and sample 2) at very low temperature in a dilution cryostat. In the first run, the two samples were

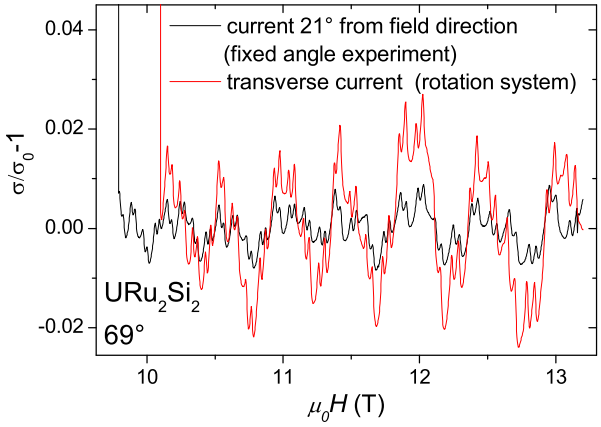

Fig. 3.24 : SdH oscillations for two different configurations in different setups. The relative size of the oscillations is higher in the transverse configuration.

measured at four fixed angles $(0°, 22°, 45°, 69°)$, determined geometrically outside the cryostat (error $< 1°$). In this run, both samples were in a transverse field configuration for $H \parallel c$, but by turning the field in the $c-a$ plane, sample one was turned approaching the longitudinal configuration (approaching $H \parallel j$) whereas sample 2 stayed in the transverse configuration (field always perpendicular to the current). The results for the oscillation frequencies and the effective cyclotron masses from the two samples agree well. However, as sample 1 showed clearly stronger SdH oscillations, we only measured this sample with the rotation system and will only show results from this sample. The results for the effective masses of the two experiments are included in the angular dependence of the effective cyclotron masses. As clearly shown in figure 3.24 the relative size of the SdH oscillations of sample 1 is much higher in the transverse configuration. Therefore it was measured in the transverse configuration with the rotation system. In this experiment, the angles were determined via the well known H_{c2} curve according to formula 3.4. The absolute error for $H \parallel c$ is $\pm 0.5°$ and $\pm 3°$ for small angles where the slope of the H_{c2} curve is small. The relative errors are much lower. However, figure 3.24 shows that the higher angles are very precise as the shape of the oscillations is very similar when compared to the fixed angle experiment.

Figure 3.25 shows the magnetoresistance of sample 1 of URu_2Si_2 with a current along the a axis and different field directions in the $c-a$ plane going from $H \parallel c = 0°$ to $H \parallel a = 90°$ measured with the rotation system. The Shubnikov-de Haas oscillations can be seen very clearly for angles smaller than 80° but they change very sensitively with the angle. For higher angles, they appear even in the relatively broad superconducting

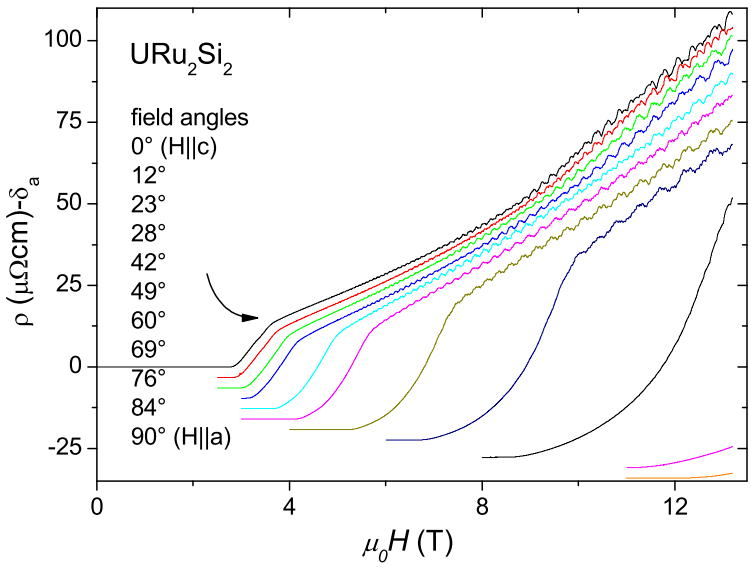

Fig. 3.25 : The magnetoresistance of URu_2Si_2 for different angles for a field in the $c-a$ plane.

transition. For $H \parallel c$ a kink appears in the magnetoresistance at approximately $H_{kink} \approx 8\,\mathrm{T}$. We will see below that this changes the quantum oscillations which occur above this field.

In the following paragraphs, we will first analyze the spectrum for $H \parallel c$. We will show the temperature dependence of the oscillatory signal and the field effects analyzed via the FFT transforms. The angular dependence of the oscillation frequencies and the effective cyclotron masses are shown and the consequences for the Fermi surface are discussed.

3.2.1 Shubnikov-de Haas oscillations for $H \parallel c$

Figure 3.26 shows the FFT spectrum for $H \parallel c = 0°$ for three different field ranges. Firstly, I examine the spectrum with the highest resolution, i.e. with the largest field range from 4 - 13.2 T. In agreement with Ohkuni *et al.* (Ohkuni et al. 1999) (see figure 3.12) I find the α, β and γ branches with frequencies $F_\alpha = 1065\,\mathrm{T}$, $F_\beta = 425\,\mathrm{T}$, $F_\gamma = 200\,\mathrm{T}$. In my measurements, the signal to noise ratio is much better and the intensity of the β peak much higher compared to (Ohkuni et al. 1999). I could also detect a band η with small frequency $F_\eta = 93\,\mathrm{T}$. The signal in the spectrum for the lowest frequencies comes partly from the imperfect subtraction of the background. From the FFT, it is not possible to tell if there are oscillations with even lower frequency. As shown in figure 3.27 we see up to 9 harmonics for the α branch, four harmonics for β and three for γ (frequencies too small to be resolved in this graph) and various combinations of different branches due to quantum interference. The amplitude of the harmonics does not follow the Lifshitz Kosevich formula for high harmonics (indicated by straight lines for α and β branches), indicating that magnetic interactions play an important role.

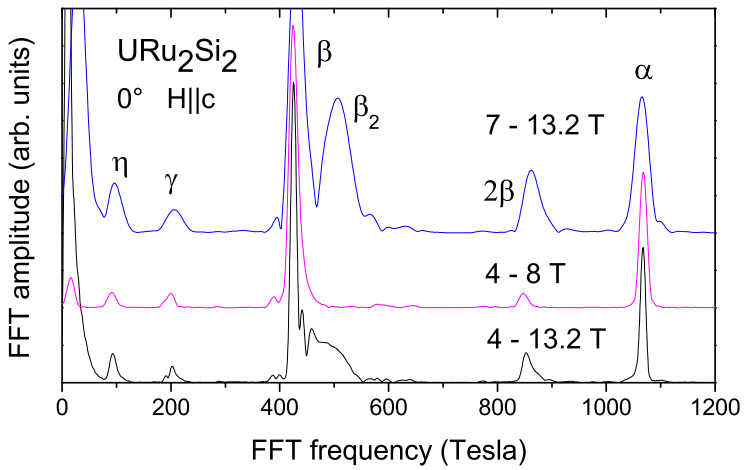

Fig. 3.26 : FFT spectrum obtained for three different field ranges for $H \parallel c$ normalized to the amplitude of the α peak.

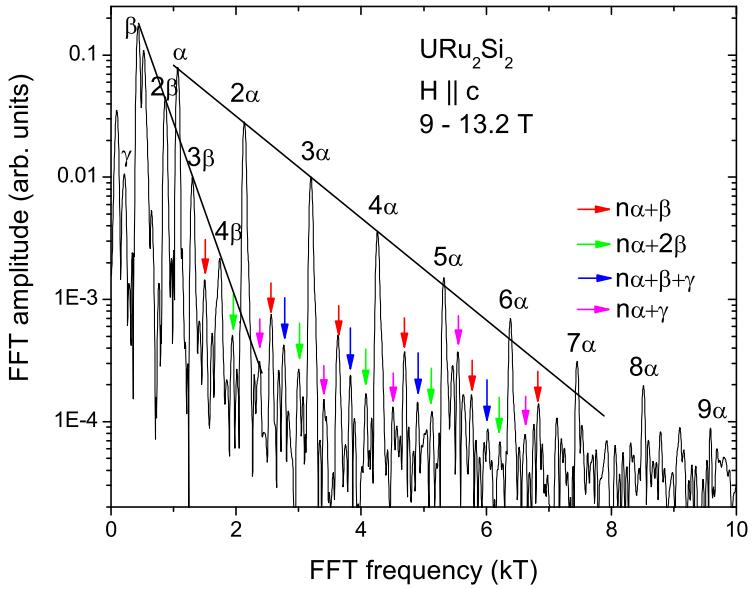

Fig. 3.27 : The FFT amplitude up to high frequencies. The FFT was taken in the field range 9 - 13.2 T. Various harmonics and combinations of the α, β and γ frequencies are seen. The amplitude of the harmonics does not follow the Lifshitz Kosevich formula for high harmonics (indicated by straight lines for α and β branches), indicating that magnetic interactions play an important role.

Field dependence

In the FFT spectrum over the whole field range a broad signal appears just above the β branch. To illustrate the effect of field on these "side peaks", figure 3.26 shows the FFT spectrum for two other field ranges. For low fields only one β peak appears, but the beating of the signal shows that it is split into two very close frequencies. Correspondingly the spectrum with the higher resolution shows a small peak on the high frequency side next to the β peak. One possible origin for this is that the spin up and spin down branches are split non-linearly with magnetic field as discussed in paragraph 1.8.2. For higher fields (blue curve), another strong peak β_2 appears.

In order to follow the field dependence of the spectrum more precisely, the whole field range was divided into smaller windows of equal size in $1/H$, each half the total inverse field range. Figure 3.28 shows the FFTs of these windows. The FFT frequency of α, β,

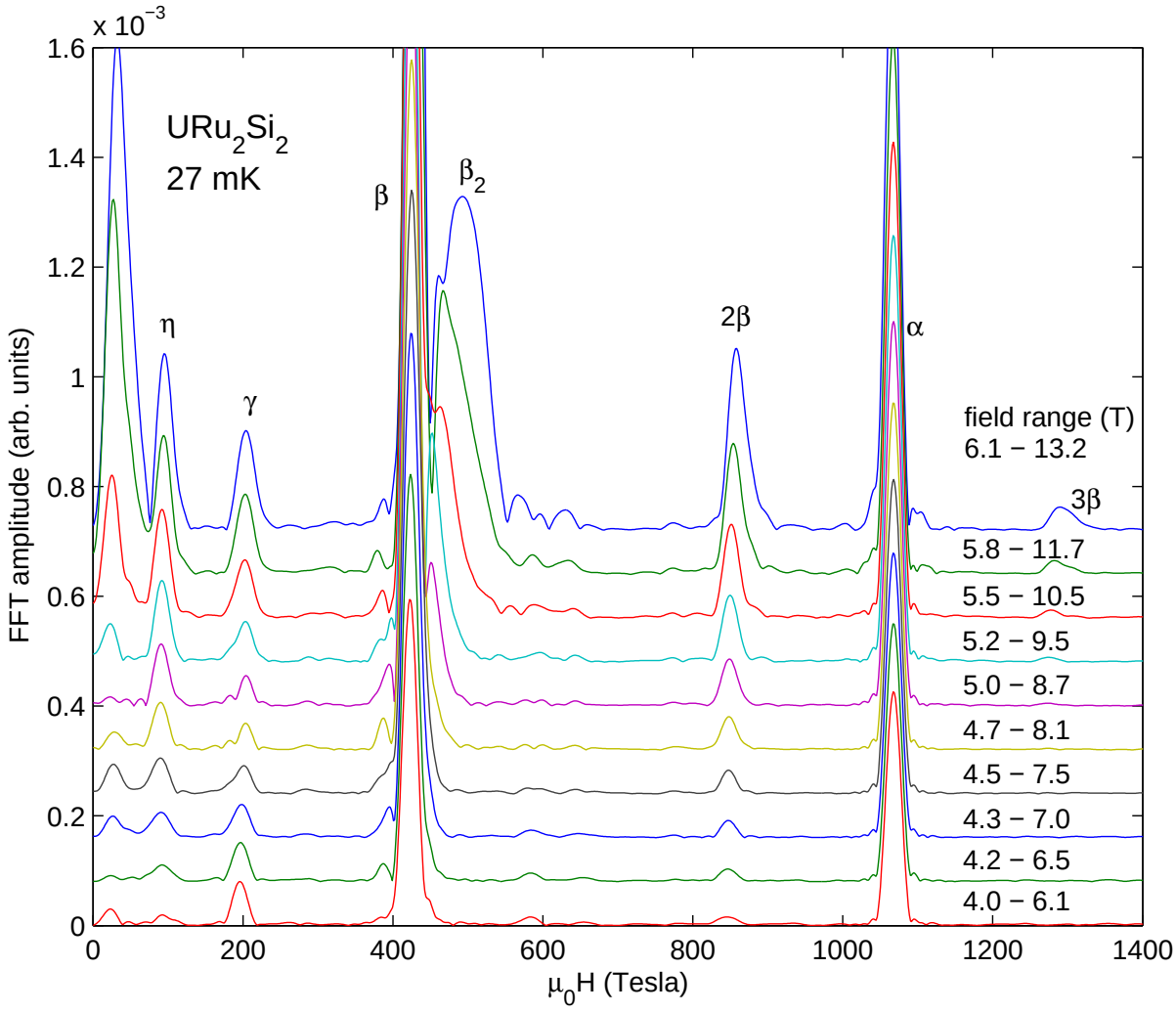

Fig. 3.28 : Field dependence of the FFT for $H \parallel c$.

γ and η branches are independent of field. At the higher frequency side of the β branch, one sharp peak (first visible in the curve 5 - 8.7 T) and a broad peak seems to appear with increasing field. However, the analysis of the higher harmonics at higher pressures (see

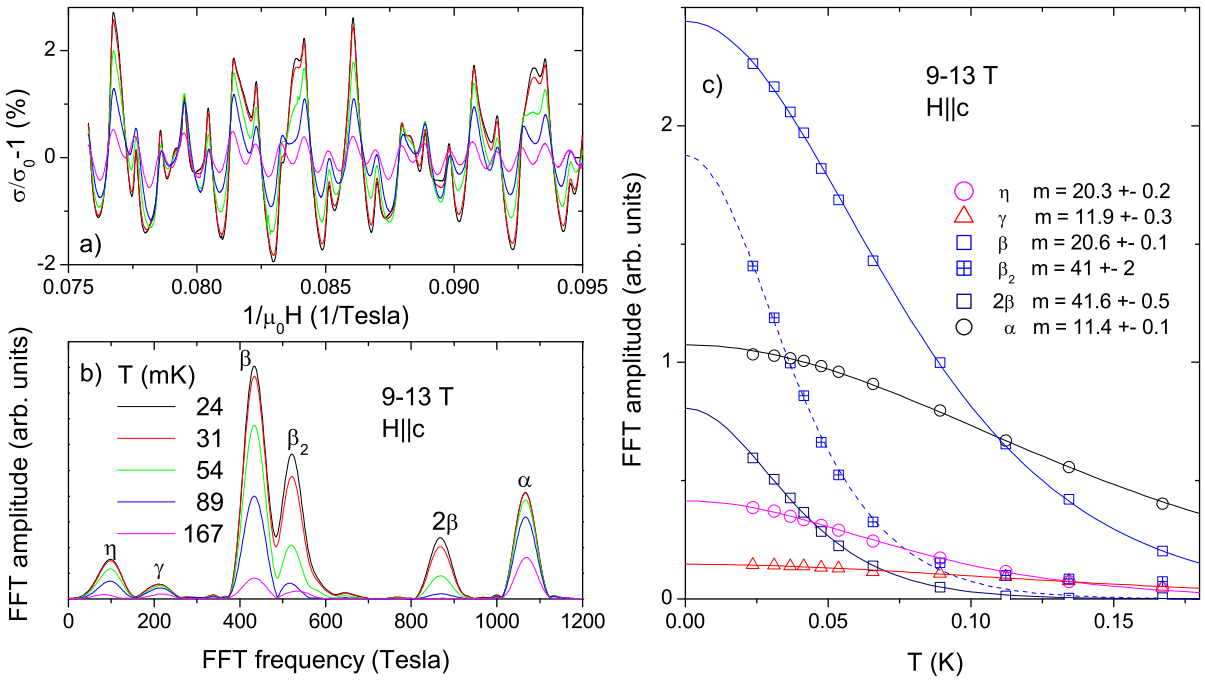

Fig. 3.29 : a) SdH oscillations and b) the FFT for different temperatures. c) Temperature dependence of the peak amplitudes. The lines are the corresponding fits with formula 1.18 giving the effective cyclotron masses.

below) shows that even the broad peak probably consists of several very close frequencies, which change their reciprocal amplitudes in field. As the β peak and its "side peaks" are very close, they interfere in the FFT. In the case of two very close frequencies depending on the field region, the FFT shows sometimes one large peak and sometimes two smaller peaks and the amplitudes are more influenced by this interference than by the field value itself. Therefore, in this measurement, it is impossible to follow the peak amplitude of the side peaks with increasing field, in order to know whether they appear suddenly at, for example, H_{kink} or if they follow the normal Lifshitz-Kosevitch formula with a high effective mass. Measurements with higher resolution, i.e. to higher field, are necessary to answer this question. The origin of these side peaks is not clear. It is possible that new orbitals appear with increasing field by magnetic breakdown. Another possibility is that a Lifshitz transition occurs at H_{kink} which leads to a reorganization of the Fermi surface with new bands and effects on the existing bands.

Remarkably, the amplitude of the γ branch first decreases with increasing field and then increases. This is due to an interference with the second harmonic of the η peak, when the resolution is too low to resolve each peak. Therefore, we were able to analyze the Dingle factor and the mean free path for the α branch only. The results will be presented later.

The effective cyclotron masses were analyzed from the temperature dependence of the oscillations shown in figure 3.29 for $H \parallel c$. Figure 3.29a shows a close up of the SdH oscillations in high field for different temperatures (the temperatures are the same as in b). For low temperatures, the oscillations are sharply peaked on the top (non sinusoidal),

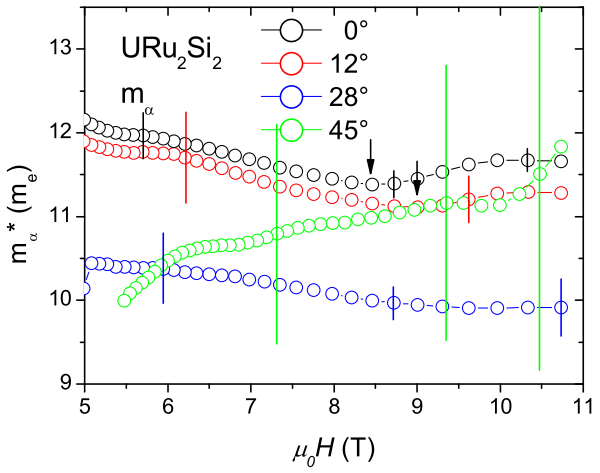

Fig. 3.30 : The field dependence of m_α for different angles. The error bars are given for a few points.

another indication for strong magnetic interaction. With increasing field this property is suppressed. The oscillations are damped and at the highest temperature shown here, mostly the α oscillations survive. In figure 3.29b, the FFT of this signal in the field range 9 - 13 T is shown. The field range was chosen to be quite high in order to be able to compare the masses for different angles as H_{c2} grows strongly with increasing angle. The peak amplitude for each branch as a function of temperature is shown in figure 3.29c. By fitting with the temperature dependent part of the Lifshitz- Kosevitch equation 1.18 (lines), we obtain the effective cyclotron masses given in the plot. The agreement with the results by Ohkuni *et al.* is good. The newly observed band η is heavy. The branch β_2, which is seen only in the high field range, is also very heavy.

The field dependence of the mass m_α is shown in figure 3.30 for several angles. For $H \parallel c$, it decreases with field initially, and then shows an upturn at approximately the kink field H_{kink}. With increasing angle H_{kink} seems to increase, just as the kink in the magnetoresistance in figure 3.25 seems to shift to higher fields. However, it is difficult to define the position of H_{kink}.

3.2.2 Angular dependence

As the oscillation frequency is proportional to the cross sectional area of the Fermi surface, we can determine the shape of the Fermi surface by measuring the angular dependence of the SdH frequencies. Figure 3.31 shows the FFT for the measured angles up to 65°. The field range is adapted to the normal state in order to have the best possible resolution for each spectrum.

All the branches and many harmonics can be followed very well. For higher angles up to six harmonics of the γ branch can be detected, as its mass is strongly decreased. The side peaks of the β branch are clearly visible in the whole angular range especially at low angles where many peaks can be resolved. They follow the angular dependence of the β branch. The field dependence of these peaks does not change considerably with the angle, but with increasing H_{c2} the resolution becomes very low. The origin of the side peaks is still not understood and this issue requires experiments at higher magnetic fields and/or lower temperatures.

The side peaks of the β branch appear only at high fields. As we want to determine

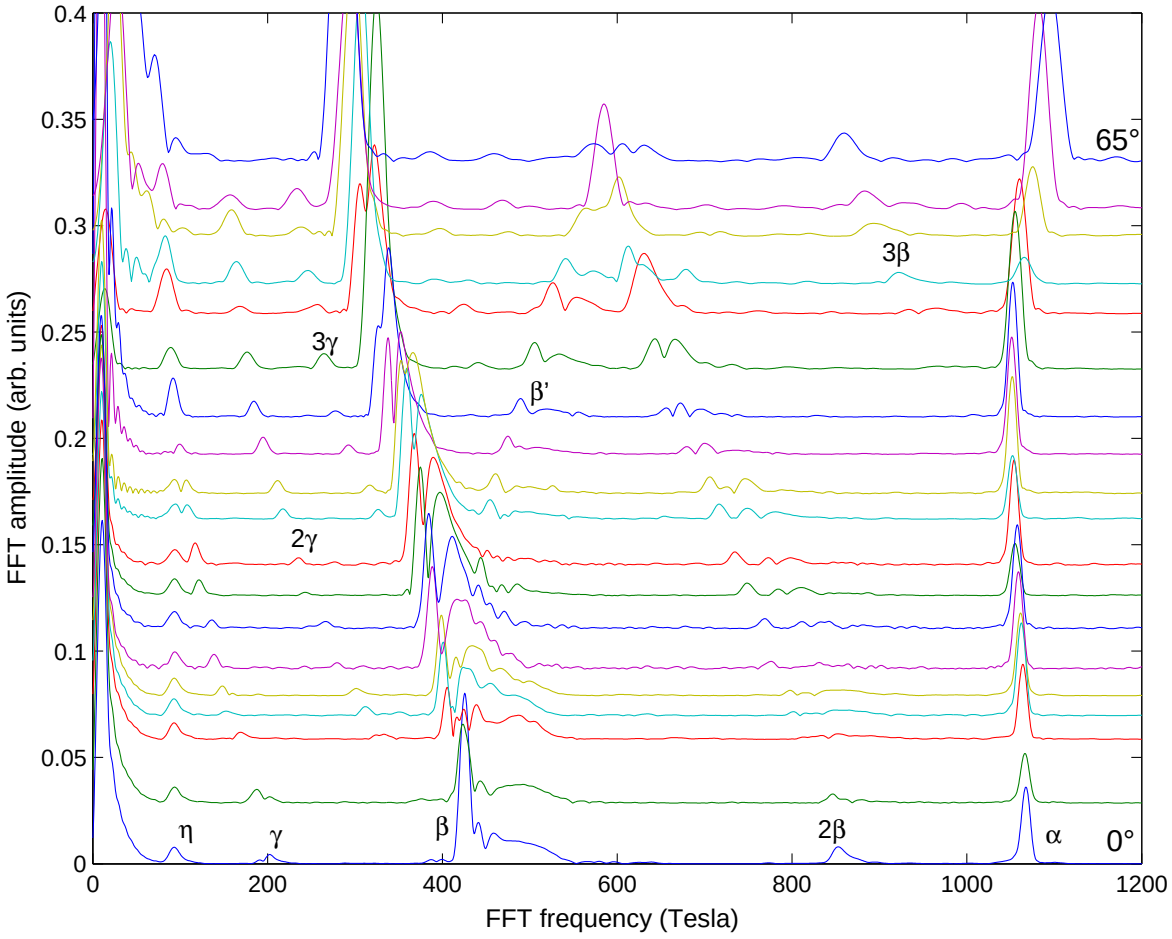

Fig. 3.31 : FFT spectra for the measured angles up to 65°. The zero is shifted for each spectrum by an offset proportional to the angle.

the Fermi surface closest to the zero field state, we only analyze the spectra in the low field range 5 - 8 T. The angular dependence of the oscillation frequencies from this field range is shown in Fig. 3.32a. Only the fundamental branches are plotted. Contrary to previously published results (Ohkuni et al. 1999) (black empty dots) additional branches are observed. Most importantly the β branch splits into two branches β and β' when rotating from $H \parallel c$ to $H \parallel a$. The previously unobserved branch β' has been observed in three different samples. We believe that both branches stem from one Fermi surface because the side peaks appear for higher fields for both branches. Measurements in the plane confirm that the two frequencies merge for $H \parallel (1\,1\,0)$, implying that they are stem from the same branch.

The splitting of a branch with angle means that the corresponding Fermi surface has different pockets with the same extremal cross sectional area for $H \parallel c$ and different areas for $H \parallel a$. For symmetry reasons such a splitting can only correspond to a Fermi surface with four non-central flattened pockets along the main axes of the Brillouin zone (BZ). Such a Fermi surface appears in band structure calculations for the small moment AF phase (Yamagami and Hamada 2000)(an obsolete idea for the HO phase), for the pressure induced large moment AF phase (Elgazzar et al. 2009) (see e) on the right side of figure

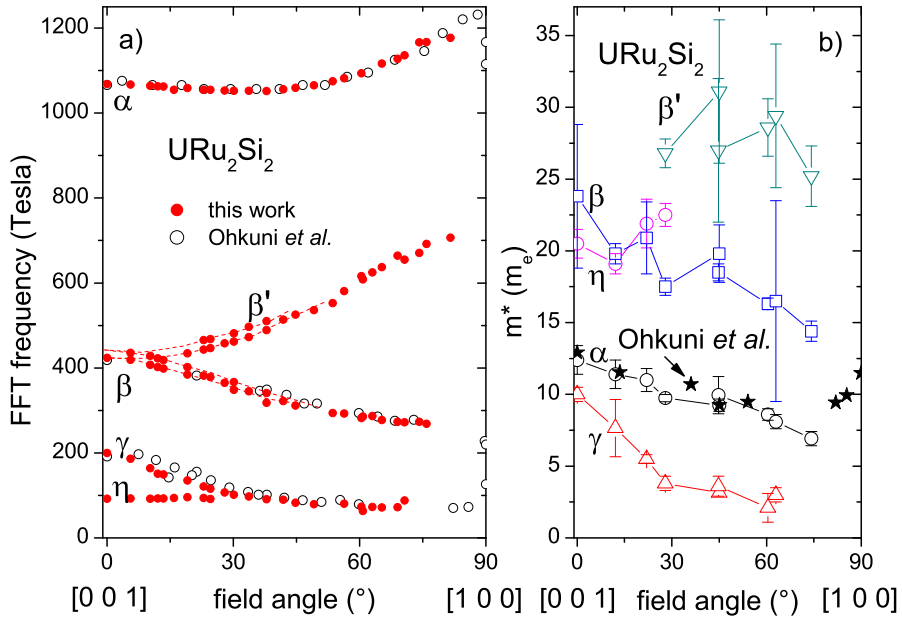

Fig. 3.32 : a) Angular dependence of the FFT frequencies obtained from SdH measurements in URu_2Si_2. The field range is 5 - 8 T as long as H_{c2} is low enough, then adapted to the available field range. b) Angular dependence of the effective masses. Earlier results by Ohkuni et al. (Ohkuni et al. 1999) are also plotted and are in excellent agreement.

3.19) but also in calculations for space group $P4_2/mmm$ (No. 136) (Harima 2010) in the paramagnetic state. In the latter calculations, the flattened pockets are a product of the overlap of two large pockets at the Γ and Z point of the body centered tetragonal BZ (see the left side of fig 3.19) which are folded on top of each other in the simple tetragonal BZ, when the unit cell doubles with ordering vector $Q_{AF} = (0\ 0\ 1)$. Therefore these pockets would not exist without ordering with Q_{AF} in the calculations. The fact that the folded Fermi surface in the AF state describes the Fermi surface in the HO state is a strong indication that the same folding occurs in both phases.

Note that even for the low fields each of the β and β' branches is split into two frequencies. As mentioned before, a possible origin of this effect is either that the spin up and spin down branches are split non-linearly with magnetic field or a warping of the corresponding Fermi surface pocket. Because the frequencies lie very close, two separated peaks appear only in the FFT for some angles. But the beating in the raw data (see figure 2.9b) is clear evidence that even the peak for $H \parallel c$ must inhibit a second peak with small amplitude and very close frequency. The approximate position of this peak is schematically plotted as a dashed line in figure 3.32a. For higher angles and increasing H_{c2}, the resolution of the FFT becomes too low to decide whether two frequencies exist but the decreased beat frequency at 42° implies that the splitting must have decreased.

The frequency of the new heavy band η appears to be independent of the angle. It could only be observed for small angles. For higher angles above 30°, where F_γ is close to F_η only one peak with a light mass in agreement with the γ branch is observed. Our results confirm that there are no open orbits as no jumps in the frequencies and no divergences are observed.

In Fig. 3.32b we show the angular dependence of the cyclotron masses. All masses besides $m_\eta^\star$ decrease with increasing angle. As we are not able to measure close to $H \parallel a$, we cannot exclude that the masses rise strongly in this direction due to the interaction of the electrons with the Ising-like longitudinal excitations. An increase for $H \parallel a$ has been observed for the α branch (black stars in Fig. 3.32b) (Ohkuni et al. 1999). From the angular dependence of H_{c2} it is expected to see higher masses for $H \parallel a$ than for $H \parallel c$. This discrepancy is not understood yet.

Assuming spherical isotropic Fermi surfaces with extremal cross sectional area $S_\mathrm{F} = \frac{2\pi e}{\hbar} F = \pi k_\mathrm{F}^2$ where F is the oscillation frequency, we can estimate the Sommerfeld coefficient γ with the determined cyclotron masses $\gamma \approx \sum_i \frac{k_\mathrm{B}^2 V m_i^* k_{\mathrm{F}i}}{3\hbar^2}$, where $V = 49\,\mathrm{cm}^3/\mathrm{mol}$ is the molar volume of URu_2Si_2. Counting the heaviest branch β four times and the other bands once, we obtain $\gamma \approx 37.5\,\mathrm{mJ/molK}^2$. β_2, which appears only in high fields is not taken into account here. With its heavy mass, it would give a sizable contribution to γ. From specific heat a Sommerfeld term of $\gamma \approx 65\,\mathrm{mJ/molK}^2$ has been measured (Maple et al. 1986).

Figure 3.33 shows a comparison of the angular dependence of the SdH frequencies determined experimentally (different colored dots) and theoretically (blue lines from reference (Oppeneer et al. 2010)). The same number of bands are observed in calculations and experiments. However, the ϵ branch appears in experiments only at very high fields. In this calculation, all FS branches besides the ϵ branch are electron-like. The ϵ branch is therefore required for compensation. The absolute frequency values from theory have a sizable error but the same order of magnitude. The calculated angular dependence of the α branch agrees quite well with experiments, but the angular dependence of the calculated ϵ branch agrees even better with the experimental angular dependence of the α branch. The splitting of β is qualitatively well described by theory even though the lower branch is too high. The flattening of the β pockets must be more pronounced than in the calculation. The angular dependence of the calculated γ and η branches are exactly the same, that is the reason why only one line is traced. In contrast to experiment, the frequencies increase with increasing angle. The γ and η ellipsoids from the calculation are elongated in the c direction, whereas experiments imply they are flattened in the c direction. The angular dependence of the calculated ϵ branch is quite flat whereas the angular dependence of the ϵ branch determined at high fields is strong. We have not detected the ϵ branch even though the observed ones do not account for γ, if the β side peaks are neglected. There are several possible reasons for this. One reason could be a very high effective cyclotron mass. In this case, the oscillations become observable only at high magnetic fields. With a missing Sommerfeld term $\gamma \approx 27\,\mathrm{mJ/molK}^2$ and an expected cyclotron frequency of around 1400 T from the calculation, we expect an effective cyclotron mass of $m_\epsilon^\star \approx 50 m_e$. From the number of harmonics observed for α and β branches, we can estimate the sensitivity of our experiment to masses of $m^\star > 70 m_e$, assuming that the mean free path is not much lower than in detected branches. Taking into accound the error of the predicted frequencies, these values agree. At high fields, a spin splitting of the majority and minority ϵ branches into a heavy and a light band as in $CeCoIn_5$ (McCollam et al. 2005) could explain why the ϵ branch observed at high fields had a low effective cyclotron mass. The last possibility is that the ϵ branch observed at high fields is a magnetic break down orbit and that the branch needed to complete the Sommerfeld term γ remains unobserved.

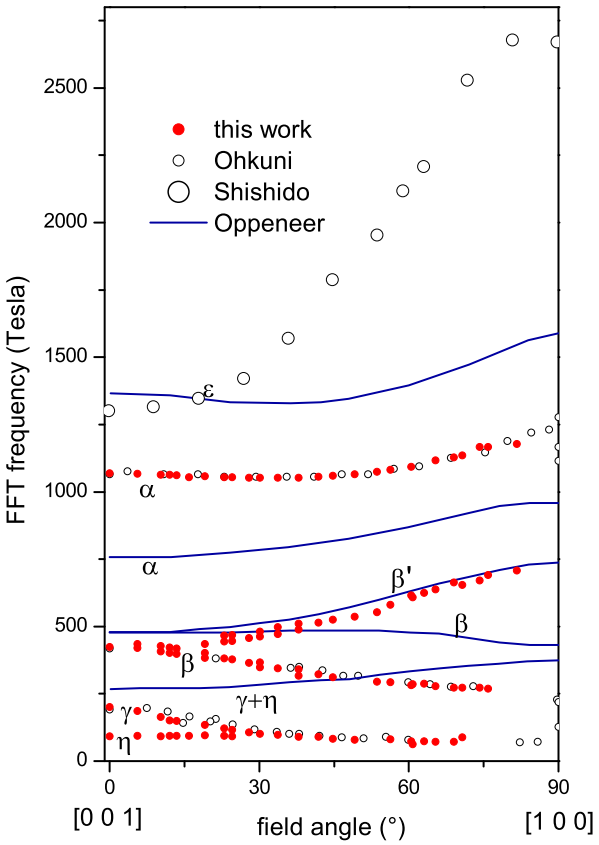

Fig. 3.33 : Angular dependence of the SdH frequencies from different experiments ((Ohkuni et al. 1999; Shishido et al. 2009), this work) compared to the calculated angular dependence of the Fermi surface by Elgazzar et al. (2009) and Oppeneer et al. (2010) (figure 3.19d,e,c).

3.3 Fermi surface under pressure

3.3.1 Magnetoresistance under pressure

By applying pressure, the system switches from the HO phase to the AF phase. The Fermi surface properties in both phases were measured. Figure 3.34a shows the magnetoresistance of URu_2Si_2 for different pressures. Up to $P = 0.85\,\mathrm{GPa}$, we see a clear kink at around $H_{kink} \approx 8\,\mathrm{T}$. The kink was also observed in the two high quality samples we measured at ambient pressure in the same geometry (see figure 3.25a). The kink is smeared out very quickly with temperature and disappears above $\approx 200\,\mathrm{mK}$ (see figure 3.36). Above H_{kink}, an oscillation with very low frequency $f < 10\,\mathrm{T}$ appears (see Figure 3.34b). In measurements of the thermoelectric power a maximum in amplitude appears at approximately the same field (Malone et al. 2010). It is an indication of a reordering of the Fermi surface possibly due to the polarization of a band for $H > H_{kink}$ as schematically presented in the upper part of Fig. 3.34c and thus possibly entering into the framework of a Lifshitz transition. The kink disappears for the highest two pressures in the AF phase. This could result from the higher charge gap and therefore lower lying band in the AF phase as in the lower part of Fig. 3.34c. Additionally, the decreased mass under pressure (see below) leads to a decreased magnetic susceptibility and a decreased polarization with magnetic field. It also disappears with increasing angle, when the η branch is not observed any more (see Fig. 3.25a the 42° curve).

The magnetoresistance in both HO and AF state will be studied in more detail. It is interesting to look at the temperature dependence of the resistivity in different magnetic

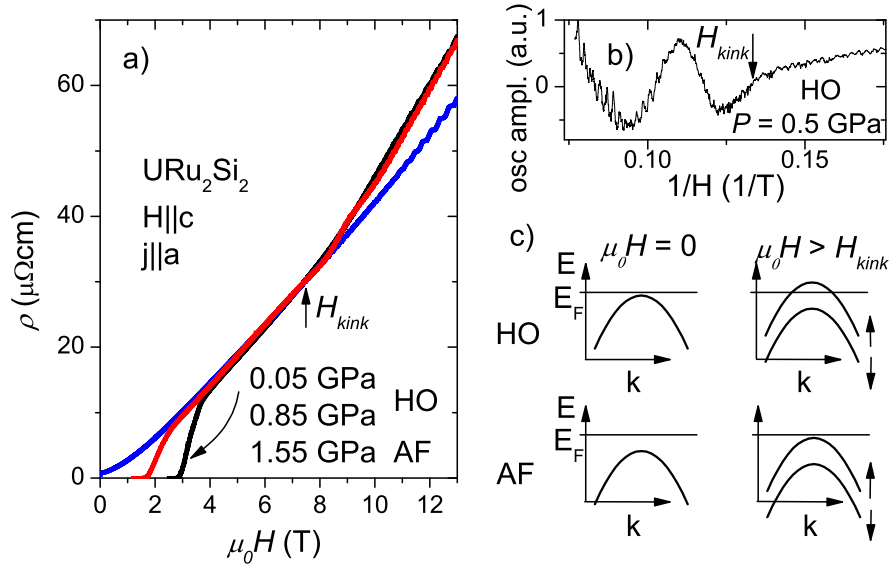

Fig. 3.34 : a) Pressure dependence of the magnetoresistance of URu_2Si_2 for three pressures in the whole measured field range at $T = 30\,\mathrm{mK}$. b) Low frequency oscillation appearing above the kink field H_{kink}. c) Schematic field dependence of a band in the HO and AF phases.

fields in the HO state and in the AF state. Figure 3.35 shows the temperature dependence of the resistivity in different constant fields in the HO state (0.5 GPa) and in the AF state (1.55 GPa). It is well known that the resistivity in zero field for a constant temperature

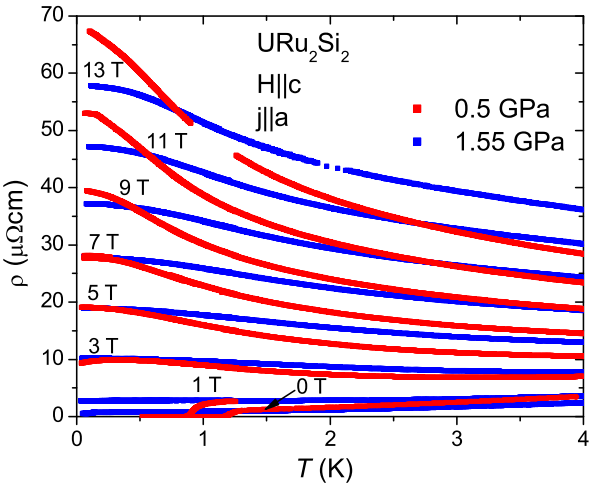

Fig. 3.35 : Temperature dependence in different constant fields in the HO state (0.5 GPa) and in the AF state (1.55 GPa).

is suppressed with pressure (by around 30 % at 2 K for between 0.5 GPa and 1.55 GPa) because the transition temperature T_0 increases and the A-term decreases (see also figure 3.42). However, as the field is increased, the resistance at 4 K for example shows a larger increase in field at higher pressure. This can be understood by looking at the magnetoresistance from the orbital effect, which is roughly proportional to

$$\omega_c \tau = \frac{B}{ne} \frac{1}{\rho} \tag{3.5}$$

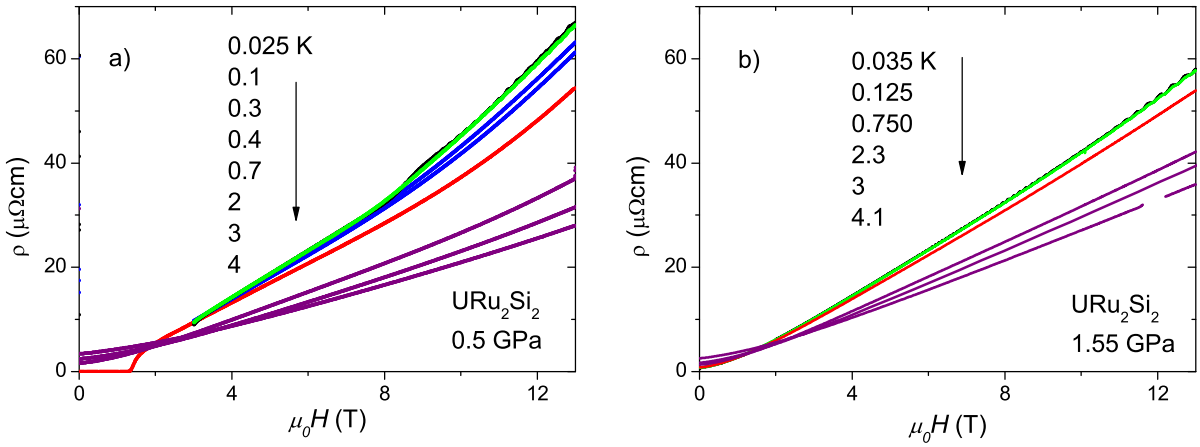

Fig. 3.36 : Magnetoresistance at different constant temperatures a) in the HO state (0.5 GPa) and b) in the AF state (1.55 GPa). Comparable temperatures have the same colors.

using equations 2.1 and 1.11. Assuming a carrier density of 0.03 carriers per uranium, independent of pressure which is equivalent to $n = 3.7 \cdot 10^{26} m^{-3}$, we find a higher magnetoresistance by roughly 30 % at 2 K for 1.55 GPa compared to 0.5 GPa, in good agreement with experiment (see figure 3.36). Nevertheless, the magnetoresistance in the zero temperature limit does not depend on the pressure up to the kink field H_{kink}. The magnetoresistance curves at the lowest temperature for all pressures are the same (see figure 3.34a) below H_{kink}. In our crude approximation, this would mean that the residual resistivity ρ_0 does not depend on pressure. However, ρ_0 is difficult to determine from fits of the temperature dependence as explained in paragraph 2.2. Above H_{kink} a change in the electronic structure leads to a higher magnetoresistance at low pressure as explained above.

The magnetoresistance at different temperatures for the same pressures is presented in figure 3.36. As expected from the temperature dependent resistivity, the magnetoresistance is higher at higher temperature for the higher pressure. The strong upturn of the magnetoresistance at 0.5 GPa at H_{kink} is rapidly smeared out (no real kink visible at 0.3 K). However, the change of slope for higher fields is clearly observable below 1 K and still traceable up to 2 K.

From these results we can conclude that the low field electronic properties in the $T = 0$ limit are very similar for all pressures i.e. for the HO and AF state.

3.3.2 Shubnikov-de Haas oscillations under pressure

As quantum oscillations appear only at low temperature, we cannot detect the change of the Fermi surface at T_0 unlike ARPES (angular resolved photo emission spectroscopy (Santander-Syro et al. 2009) or STM (scanning tunneling microscopy) (Schmidt et al. 2010). However, pressure is a good way to tune the system to the AF phase. A previous pressure study of quantum oscillations could only follow the α branch with a light mass (Nakashima et al. 2003). However, in the pressure experiment presented here, all the known branches besides the η branch could be detected.

The pressure measurements were performed on a single crystal with $RRR = 160$.

Figure 3.37 shows the SdH oscillations between 10 T and 13 T for $H \parallel c$ at the lowest temperature $T = 30$ mK for the five measured pressures. The absolute amplitude is much smaller than in the sample used in the rotation system (see figure 3.29), confirming the smaller sample quality reflected in the RRR. The oscillations are sharply peaked on the top for the lowest three pressures, i.e. in the HO phase, a signature of magnetic interactions. For the two higher pressure, i.e. in the AF phase, the oscillations are rather sinusoidal. The explanation for this is that the susceptibility decreases strongly in the AF phase decreasing the feedback of the magnetization on the oscillations (Motoyama et al. 2010). The beating of the signal observable for all pressures, has a higher frequency for

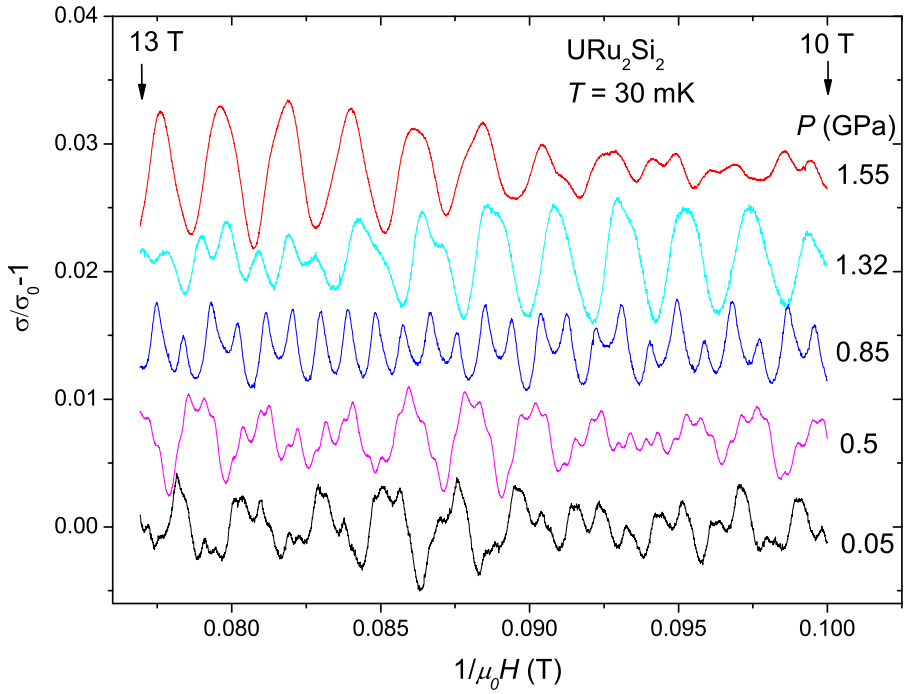

Fig. 3.37 : SdH oscillations between 10 T and 13 T at low temperature at different pressures in URu_2Si_2.

the lower pressures. The frequency difference of the two lines responsible for the beating increases therefore with pressure. This will be seen later also in the FFT.

Figure 3.38 shows the FFT spectra for three pressures in three different field ranges at the lowest temperature. We will look in more detail to the behavior of the β peak and its side-peaks in the different field ranges. In the total field range (bottom panel), the lower pressures (in the HO state), the side peaks of the β peak appear, similar to ambient pressure (see figure 3.26). At 1.55 GPa however, two well resolved peaks appear. In the low field range, two peaks seem to exist in all pressures around the β frequency. In the lowest pressure, the peaks are not separated, but the beat in the raw data is a clear sign that there are two frequencies. The splitting of these two peaks seems to increase with pressure. However, taking into account all measured pressures, the splitting increases step-like at the critical pressure. In the high field range for all pressures, the additional side peaks become strongly enhanced. This poorly understood behavior therefore does not change when entering in the AF phase.

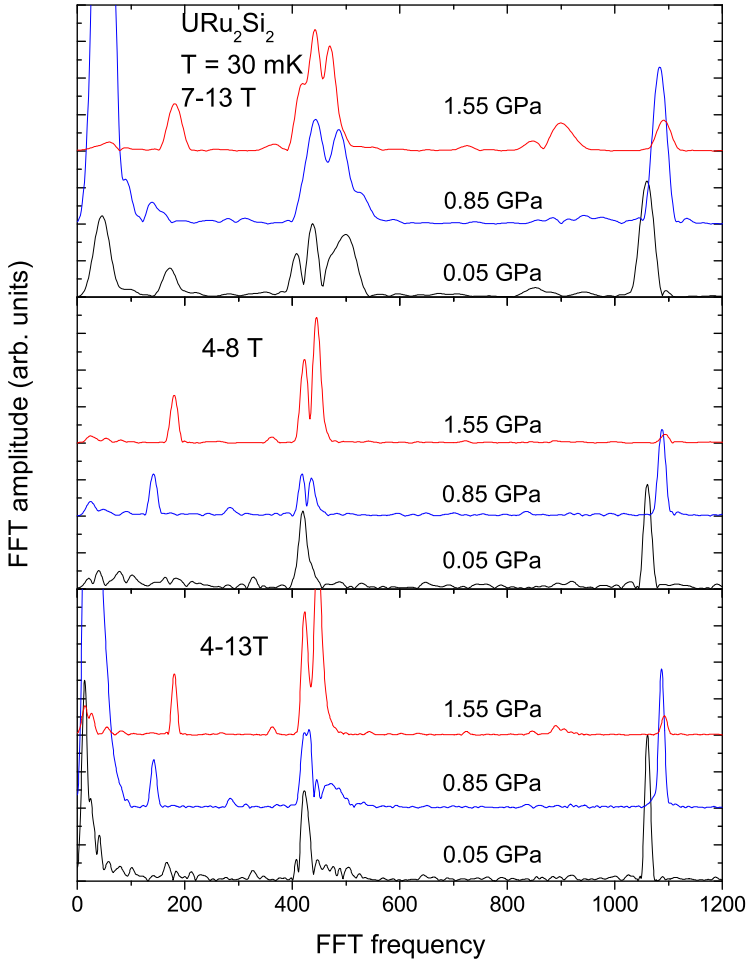

Fig. 3.38 : FFT spectra for three pressures in different field ranges.

At the highest pressure, superconductivity is suppressed. Therefore SdH oscillations appear already at very low field. Due to the higher total field range, it is easier to determine the field dependence at this pressure than at low pressure. Figure 3.39a presents the field dependence of the β peak and its side peaks at 1.55 GPa, where the total inverse field range is chosen from 1/13 T to 1/2 T, divided into equal windows of half the total inverse field range ("FFT range" = 0.5). Figure 3.39a shows a zoom of the FFT spectra for the high fields (the field ranges are given next to the figure). The width of the higher β peak increases with field and the position of the peak seems to shift to higher fields with increasing field. By looking at the second harmonic (figure 3.39b, the frequency axis is scaled by 2, because all the frequencies of the second harmonics are doubled) a better resolution is found. It is clearly seen that the second peak consists of several very close peaks and that their amplitude grows with field. In figure 3.39d, the ratio of the amplitudes of the second divided by the first peak ($(A_2)/A_1$) is drawn as a function of the effective field. The increase of this ratio gives an explanation for the shift of the first harmonic with field. Furthermore, the increase of the side peaks explains why the peak in the first harmonic becomes wider with increasing magnetic field. With a smaller window in the inverse field range, much higher maximum effective fields can be reached. In figure

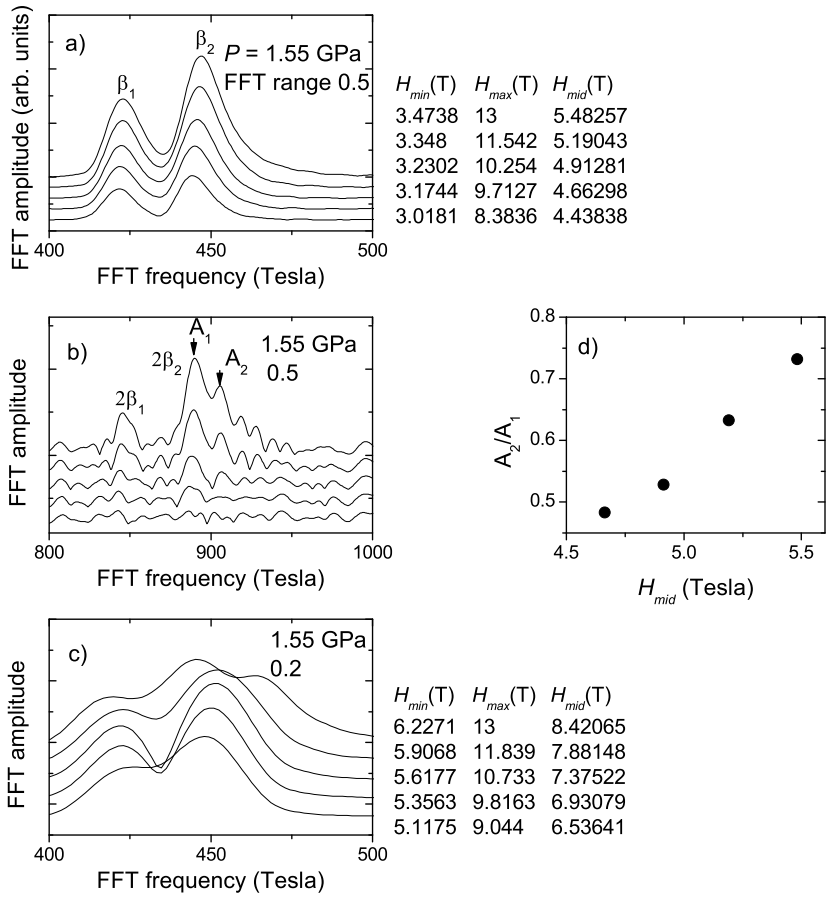

Fig. 3.39 : Field dependence of the FFT spectrum around the β peak and its side peaks at $T = 30\,\mathrm{mK}$ at 1.55 GPa. In a) and b) a zoom on the first and second harmonic of the β peak is shown with a large FFT range, i.e. a large inverse field window and good resolution of the FFT spectrum. c) shows the β peak for a smaller FFT range. In d) is plotted the field evolution of the ratio of the amplitudes of the second and the first β peaks from b).

3.39c the FFT spectra with an FFT range of 0.2 are plotted. For the highest field, clearly one side peak is resolved but with a very bad resolution. To summarize, figure 3.40 shows the peak positions of the β peaks as a function of the field for different FFT ranges. For the highest FFT range, i.e. the highest resolution, one sees that the side peaks in the second harmonic appear subsequently with increasing field. With the lower resolution, the position of the second peak seems to shift to higher fields but the second harmonic does not shift in the same way. My conclusion is that the peaks do not shift with field, only the amplitude of the side peaks increases. As the field behavior does not depend on the pressure, this should be the case also in the HO phase. However, the origin of these side peaks is unclear.

The amplitude of the α peak is strongly decreased at the highest pressure in the AF phase (see figure 3.38). An analysis of the field dependence of the peak amplitude of the α branch reveals that the mean free path decreases by a factor of 2 between the lowest and the highest pressure. Table 3.2 shows the pressure dependence of the Dingle temperature

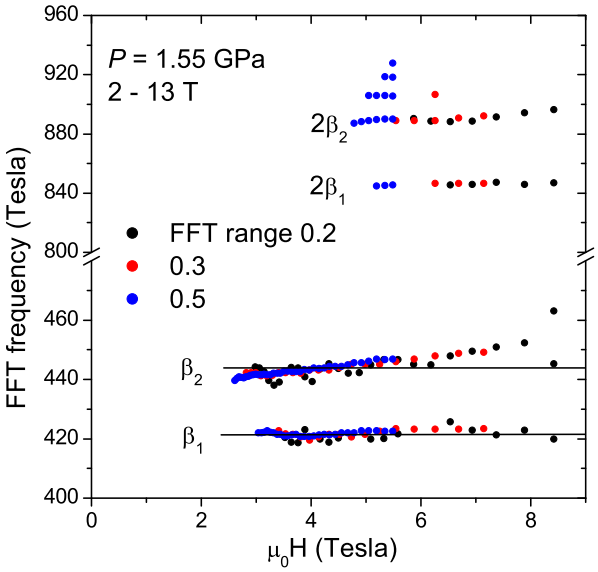

Fig. 3.40 : Field dependence of the peak positions of the β peak and its side peaks and the second harmonics at $T = 30\,\mathrm{mK}$ for different FFT ranges. The peak positions are determined from the FFT spectra shown in figure 3.39.

P(GPa)	T_D(K)	l_0(Å)
0.05	0.08	3100
0.85	0.16	1900
1.55	0.26	1600

Table 3.2: Pressure dependence of the Dingle temperature T_D and the mean free path l_0 for the α branch.

T_D and the mean free path l_0 for the α branch. It is interesting to note that the mean free path decreases a lot under pressure whereas the resistivity in the zero temperature limit ρ_0 is approximately constant. As we observe the decrease of l_0 only for one band, this effect may be explained by the ensemble of the bands.

Figure 3.41a presents the FFT spectra for the lowest and the highest pressure. A small change in the spectra is seen for the β branch at high pressure deep inside the AF phase. It is clearly split into two separate peaks with nearly the same masses. Recalling that at low pressure there is a second small peak within the β peak, the analysis shows that the splitting increases at P_x and the amplitude of the second peak increases strongly.

Even though the resolution in these measurements is extremely good, we cannot resolve the second peak at low pressures. The side peaks just above the β branch which are clearly seen in the spectrum at the low pressures still exist for the upper peak, but their effect is much smaller and appears at higher fields. This could again result from the higher charge gap in the AF phase.

The reason for the increased splitting in the AF phase may be a stronger non-linear field dependence of the SdH frequencies or a stronger warping of the corresponding Fermi

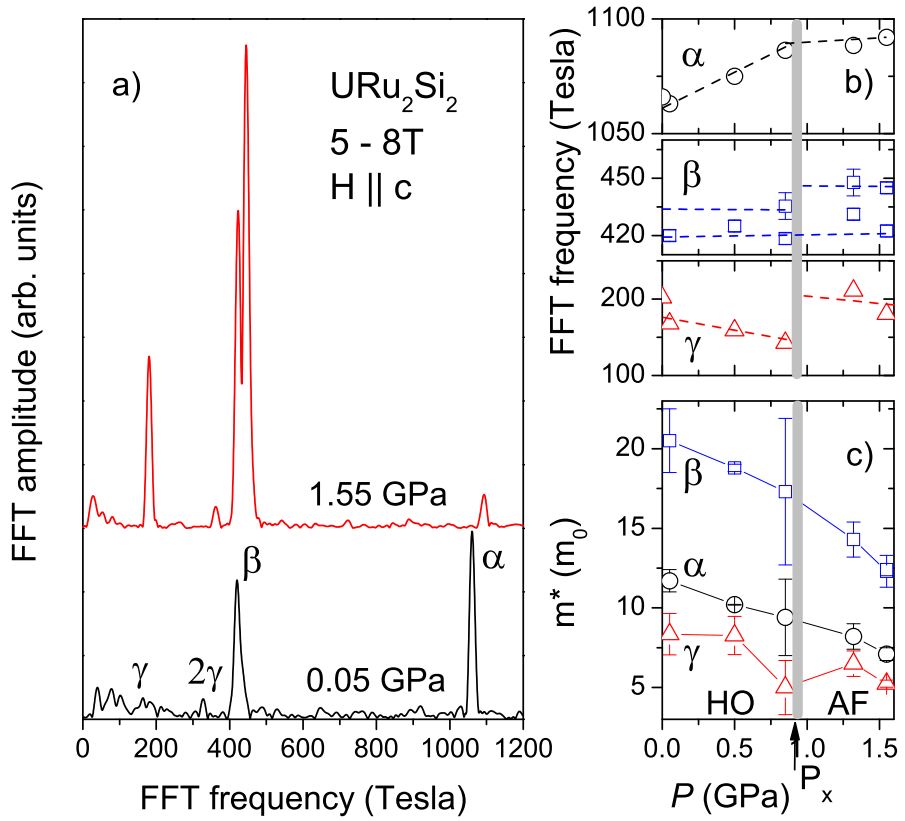

Fig. 3.41 : a) FFT spectra of SdH measurements in URu_2Si_2 for $H \parallel c$ at the lowest temperature of $T \approx 35\,\mathrm{mK}$ for $P = 0.05\,\mathrm{GPa}$ and $T \approx 25\,\mathrm{mK}$ for $P = 1.55\,\mathrm{GPa}$. b) Pressure dependence of the FFT frequencies. The β peak is split as explained in the text, indicated by the dashed lines. c) Pressure dependence of the effective masses determined in a field range of 8 - 13 T.

surface pocket. But this needs further experimental investigations i.e. the angular dependence under pressure. The pressure dependence of the FFT frequencies is shown in Fig. 3.41b. F_α increases slightly with pressure and then has a plateau in the AF phase, in agreement with Ref. (Nakashima et al. 2003). F_β is, apart from the increased splitting (position of the second peak indicated by the dashed line), independent of pressure. F_γ decreases with pressure and then jumps to a higher value at P_x. Pockets of this size are very sensitive to small changes of the band structure.

These measurements indicate no significant change in the FS between the HO phase and the AF phase. In three recent theoretical proposals the order parameter has an ordering vector $Q = (0\,0\,1)$ (Elgazzar et al. 2009; Harima et al. 2010; Haule and Kotliar 2009) and the Fermi surface in the AF and HO states are similar or the same within each model. All the masses decrease with pressure as seen in Fig. 3.41c. The decrease agrees with the decrease of the A coefficient of the T^2 behavior of $\rho - \rho_0$ with pressure (see below).

3.4 Hidden Fermi liquid behavior in URu_2Si_2

In the hidden order of URu_2Si_2 the resistivity at very low temperature shows no T^2 behavior above the transition to superconductivity. However, when entering the antiferromagnetic phase the Fermi liquid behavior is recovered. We discuss the change of the inelastic term when entering the AF phase with pressure by considering the temperature dependence of the Grüneisen parameter at ambient pressure and the influence of superconductivity by an extrapolation of high field data.

Already McElfresh *et al.* (McElfresh et al. 1987) have remarked that at low temperature one never finds a T^2 behavior, even for a very small temperature range just above the superconducting transition. Recently, an anisotropic inelastic term of the resistivity in the HO state was found (Zhu et al. 2009) which could indicate an anisotropic scattering mechanism due to the order parameter in this phase. In Ref.(Miyake and Flouquet 2010) it has been shown that a quadrupolar charge order and its excitation can cause this anisotropy. However, a detailed study on crystals with different quality should clarify the influence of sample quality (Matsuda et al. 2010). If this anisotropy is a signature of the order parameter of the HO state then the temperature behavior of the resistivity should change under pressure when entering the antiferromagnetic state. Here we present high pressure resistivity measurements to address this question.

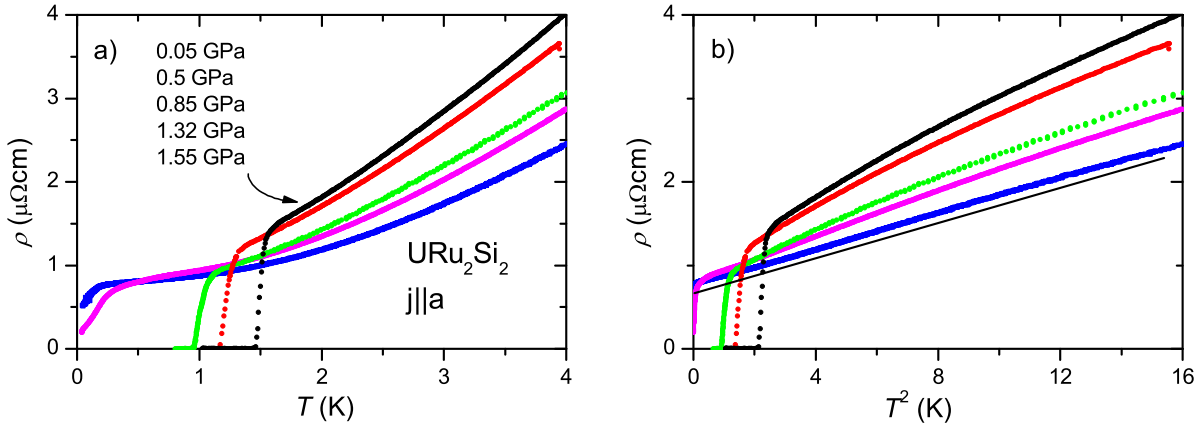

Fig. 3.42 : a) Resistivity as a function of temperature in zero magnetic field for several pressures. (b) The same data as a function of T^2. The straight line is a guide to the eye.

The temperature dependence of the resistivity for the measured pressures is shown in figure 3.42 as a function of T (a) and T^2 (b). One clearly sees that the resistivity does not show a T^2 dependence over an extended temperature range for the low pressures whereas for $P = 1.55\,\mathrm{GPa}$ a T^2 dependence is observed up to 3.5 K. For the three lowest pressures $P < 0.85\,\mathrm{GPa}$ a complete superconducting transition with zero resistivity appears whereas only an onset of the superconducting transition is observed for the highest pressures.

In figure 3.44 we plot the pressure dependence of superconducting parameters and fit parameters one can extract from these data. One striking feature in almost all of them is the discontinuous pressure dependence between 0.85 GPa and 1.32 GPa. It evidently shows that the transition between the HO and the pressure induced AF state appears

between these two pressures, i.e. 0.85 GPa $< P_x <$ 1.32 GPa. Magnetoresistance measurements on the same sample also show a clear change between the lower three and the higher two pressures (see paragraph 3.3.1). It is well known that the critical pressure between HO and AF depends on the sample and pressure conditions. In figure 3.44a, we show the A coefficient of a forced $\rho = \rho_0 + AT^2$ fit at $H = 0$ between 1.8 K and 2.5 K. It decreases strongly with pressure. However, in the present measurements, the pressure steps were too large to detect a discontinuity of A at the critical pressure P_x (Hassinger et al. 2008). As $A \propto (m^\star)^2$ we have plotted the normalized square of the effective band mass of the β branch determined in recent Shubnikov-de Haas measurements (Hassinger et al. 2010) (blue stars) as well as the normalized square of the initial slope of the upper critical field H_{c2} near T_{sc} (small triangles) (which are both proportional to the effective mass) as a function of pressure. The pressure dependence of all these parameters is consistent.

As expected from a visual inspection of the data, this T^2 fit does not reproduce the data well at low pressures. Therefore, I fitted the data also with a $\rho = \rho_0 + AT^x$ fit for temperatures between 1.8 K and 3.5 K (figure 3.44b). The exponent is around 1.5 in the HO state and a clear T^2 behavior is found only deep inside the AF phase. These results have been confirmed by Tateiwa et al. (2010). Previous measurements on single crystals with lower quality with the current in an arbitrary direction showed a similar behavior (Hassinger et al. 2008). From these data and field sweeps at constant temperatures the

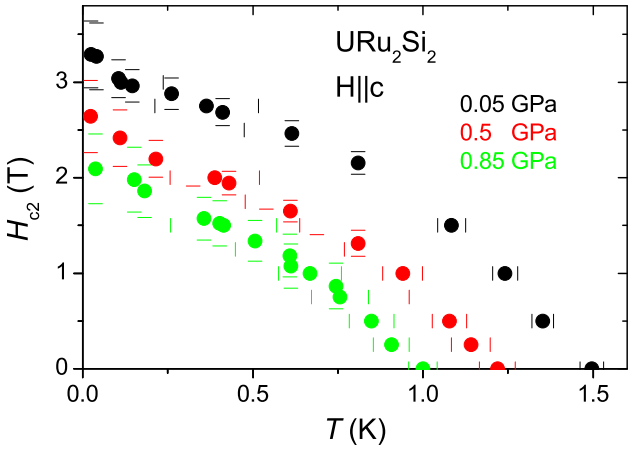

Fig. 3.43 : H_{c2} in URu_2Si_2 for field along the c axis for several pressures.

H_{c2} curve was determined for all pressures as shown in figure 3.43.

The superconducting parameters T_{sc} and H_{c2} (figure 3.44c and d) decrease linearly with pressure and then disappear abruptly above P_x. The critical pressure where superconductivity would disappear extrapolated from the low pressure data is at around 2 GPa. In earlier pressure studies of the resistivity on samples with lower quality, the decrease $T_c(P)$ was linear (Hassinger et al. 2008; Jeffries et al. 2008; McElfresh et al. 1987) up to the pressure where the superconducting phase disappeared. The superconducting transition was observed up to quite high pressures (far above 1 GPa for the above mentioned references). In contrast, in magnetic susceptibility and especially specific heat measurements, which are sensitive to bulk transitions, the superconducting state disappeared at the critical pressure (Amitsuka et al. 2007; Hassinger et al. 2008).

The non-Fermi liquid behavior in resistivity is observed only in the HO phase and disappears in the AF phase. The same happens with superconductivity. It is tempting to

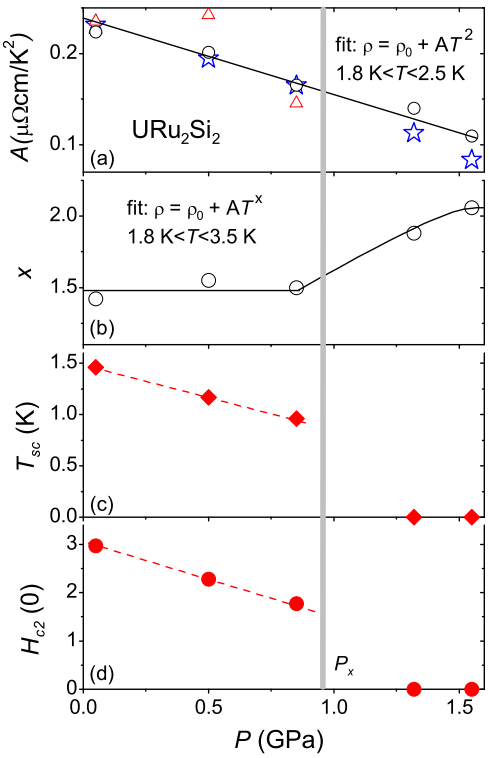

Fig. 3.44 : Pressure dependence of several parameters determined from resistivity measurements at zero field (a-c) and with $H \parallel c$. In (a) we further show the pressure dependence of the normalized square of the effective mass of the heavy β branch (blue stars) and the normalized square of the initial slope of the upper critical field (triangles). The critical pressure P_x is indicated by the gray line. Lines are to guide the eye, indicating a T^2 dependence.

claim that a component of linear temperature behavior is a signature of the HO state or even stronger that superconductivity is linked to a linear resistivity term as was claimed in high temperature and organic superconductors (Doiron-Leyraud et al. 2009). However, in URu_2Si_2 one should be careful. A recent study of the Grüneisen parameter gives a saturation only at very low temperature (Hardy 2010). Accordingly, the Fermi liquid behavior in resistivity may be hidden by the onset of superconductivity. Zhu et al. (2009) have studied the temperature behavior of the resistivity in field with a longitudinal configuration ($H \parallel I$) to avoid transverse magnetoresistance. If the resistivity is expressed as $\rho_0 + AT^x$, they report $x < 2$ for the zero field measurements in both crystal directions. With field, a Fermi liquid behavior is recovered above $H_{c2} = 3\,\mathrm{T}$ for a current and field along the c axis whereas a linear temperature dependence for current and field along a remains up to the maximum field of $H = 12\,\mathrm{T}$. However this field is not high enough to suppress superconductivity along the a axis completely. To overcome this problem for $H \parallel a$ we have performed magnetoresistance measurements as function of field for different constant temperatures (Matsuda et al. 2010). Extrapolating the magnetoresistance from the normal state at high fields above H_{c2} to zero field at constant temperatures $T < T_{sc}$, the resistivity in the normal state in the absence of superconductivity has been extrapolated. From these extrapolations, a T^2 behavior (Matsuda et al. 2010) with a coefficient A in good agreement with our result at zero pressure is observed.

Knowing the Grüneisen parameter $\Gamma = 40$ (Hardy 2010) and the compressibility $\kappa \approx 0.5 \cdot 10^{-6}\,\mathrm{bar}^{-1}$ (Jeffries 2010) allows a prediction for the relative change of A with pressure: As $A \propto (m^\star)^2$ with the characteristic temperature $T^\star \propto 1/m^\star$, then $dT^\star/T^\star = dm^\star/m^\star = 1/2dA/A$. With the definition of the Grüneisen parameter

$$\Gamma = -d\ln T^\star / d\ln V = \kappa^{-1} d\ln T^\star / dp$$

we find for a pressure difference of $\Delta p = 0.5\,\mathrm{GPa}$ a relative change of $\Delta A/A \approx 0.2$ in agreement with our data. To summarize, we show the change of the temperature dependence of the electrical resistivity in URu_2Si_2 with pressure. As expected from the Grüneisen parameter, Fermi liquid behavior appears at very low temperatures $T < T_{sc}$ only. Superconductivity has to be suppressed to be able to observe a T^2 temperature dependence. However, we cannot exclude peculiar scattering in the HO state but it is difficult to prove conclusively.

3.5 Conclusion

I present results of the electronic properties of URu_2Si_2 by means of resistivity measurements at ambient pressure and under pressure up to magnetic fields of 13.2 T.

By Shubnikov-de Haas measurements at ambient pressure in the HO state, previously unobserved Fermi surface branches are detected which allow several conclusions about the Fermi surface. Firstly, a nearly spherical band η at low frequencies is observed. Secondly, the branch β splits into two branches when the field direction is changed from $H \parallel c$ to $H \parallel a$, a proof that it is a non-central fourfold Fermi surface pocket. By including this information into the estimation of the Sommerfeld term assuming spherical Fermi surface pockets we obtain 55 % of the value determined by specific heat.

The angular dependence of the frequencies in the plane by measurements up to higher field will give complementary information about the Fermi surface shape. Higher fields are also necessary to understand the side peaks of the β branch appearing in high fields in my measurements.

Under pressure, the low field spectrum of SdH oscillations does not change when entering the pressure induced AF state. Hence, the observed Fermi surface pockets are the same in the HO phase and the AF phase.

It is evident that the Brillouin zone is folded at high pressure when going from the paramagnetic state at high temperature to the AF state. Independent of calculations SdH results are difficult to interpret. There are two possible cases: The first one is that the detected Fermi surface pockets are so small that they are not affected by a change of the Brillouin zone. It is possible that only the unobserved branch is affected by the folding. However, it is probable that the folding affects all the branches because of the strong changes detected at the transition temperature from paramagnetic state to both HO or AF state by resistivity and specific heat. The other possibility is that the Fermi surface changes drastically by folding, especially the four fold β Fermi surface is a product of two larger pockets in the paramagnetic state. In this case, the similarity of the detected Fermi surface pockets in the HO state and in the AF state imply that already in the HO, the Brillouin zone is cut into half by an ordering vector $Q_{AF} = (0\,0\,1)$ and that the unit cell is doubled. In both cases, our results are a good test for theoretical predictions for the order parameter.

The magnetoresistance shows a kink in the HO phase which disappears in the AF state. Additionally for 0.5 GPa and 0.85 GPa a very low frequency oscillations appears above this kink. This points to a polarization effect and eventually to a Lifshitz transition in field. Also side peaks appear just above the β branch. These field effects are not well understood and measurements with higher resolution are necessary. One conclusion

is nevertheless possible: The Fermi surface in the AF state is a little less sensitive to magnetic fields than the Fermi surface in the HO state. This is supported by the fact that the signs of magnetic interaction (sharply peaked SdH oscillations) appear at high field only in the HO state.

The angular dependence of the effective masses has been determined. The electron or hole-like nature of the Fermi surface pockets cannot be determined via SdH measurements. However, different measurements (Hall effect, resistivity, Seebeck and Nernst effect, H_{c2}) detect opposing anisotropies and signs. The multiband nature of URu_2Si_2 is the explanation for this. As all the detected bands from the SdH measurements presented here show the same angular anisotropies the unobserved bands should have an inverse angular dependence of the effective mass, because of the anisotropy of H_{c2}.

As a last point it was shown that the temperature dependence of the zero field resistivity does not follow a Fermi liquid behavior in the HO state but such a behavior is recovered in the AF state with pressure. There are again two different possible interpretations. In one, special scattering mechanisms in the HO state provoke NFL resistivity. In the other one, the Fermi liquid behavior appears only at very low temperature but is hidden by the onset of superconductivity. This is supported by the increasing Grüneisen parameter down to very low temperatures. Further pressure studies with the current along the c axis and theoretical calculations for the resistivity are necessary to settle this point.

Chapter 4

Pressure-temperature phase diagram of UCoGe

UCoGe is the most recently discovered ferromagnetic superconductor. In this chapter, after an introduction to the compound, I will present measurements of the pressure phase diagram of this compound. The phase diagram found by first resistivity measurements on a polycrystal is different to the well studied compound UGe_2 because the superconducting phase extends into the paramagnetic phase induced by pressure. This was highly surprising and in the discussion of these results I express a certain doubt about the bulk nature of superconductivity in the high pressure phase.

However, the phase diagram was confirmed by measurements on a single crystal (resistivity and ac susceptibility) and the bulk nature of the superconducting phase was definitely confirmed by ac calorimetric measurements. These measurements are presented in the second part of the chapter.

4.1 Introduction to UCoGe

UCoGe was discovered in 2007 during doping studies of URhGe with cobalt on the rhodium site (Huy and de Visser 2009; Huy et al. 2007). In this study the aim was to find the critical doping, where the ferromagnetic phase is suppressed as UCoGe was reported to be non-magnetic (Buschow et al. 1990; Troc and Tran 1988). UCoGe has an orthorhombic TiNiSi crystal structure (space group P_{nma}) with uranium zigzag chains along the a axis. However, Huy *et al.* found on good polycrystals with $RRR = 25$ a T_{Curie} of 3 K (see the left side of figure 4.1) and superconductivity at around 0.8 K (right side of the same figure) by resistivity, ac-susceptibility, thermal expansion and specific heat. The Sommerfeld coefficient is $\gamma \approx 50\,\mathrm{mJ/molK^2}$. Using the Ehrenfest-relation T_{Curie} is expected to decrease with pressure and a simple extrapolation gives a critical pressure of around 1 GPa. UCoGe is therefore closer to the quantum critical point than UGe_2.

Magnetization measurements on a single crystal with $RRR = 30$ are shown in figure 4.2 (Huy et al. 2008). The moments are ordered along the c axis with a value of $m = 0.07\,\mu_B$/U. This moment is much smaller than the effective moments at high temperature responsible for the Curie-Weiss behavior $m_{eff} = 1.7\,\mu_B$/U. This indicates that the ferromagnetism has weak itinerant character. It might correspond better to existing the-

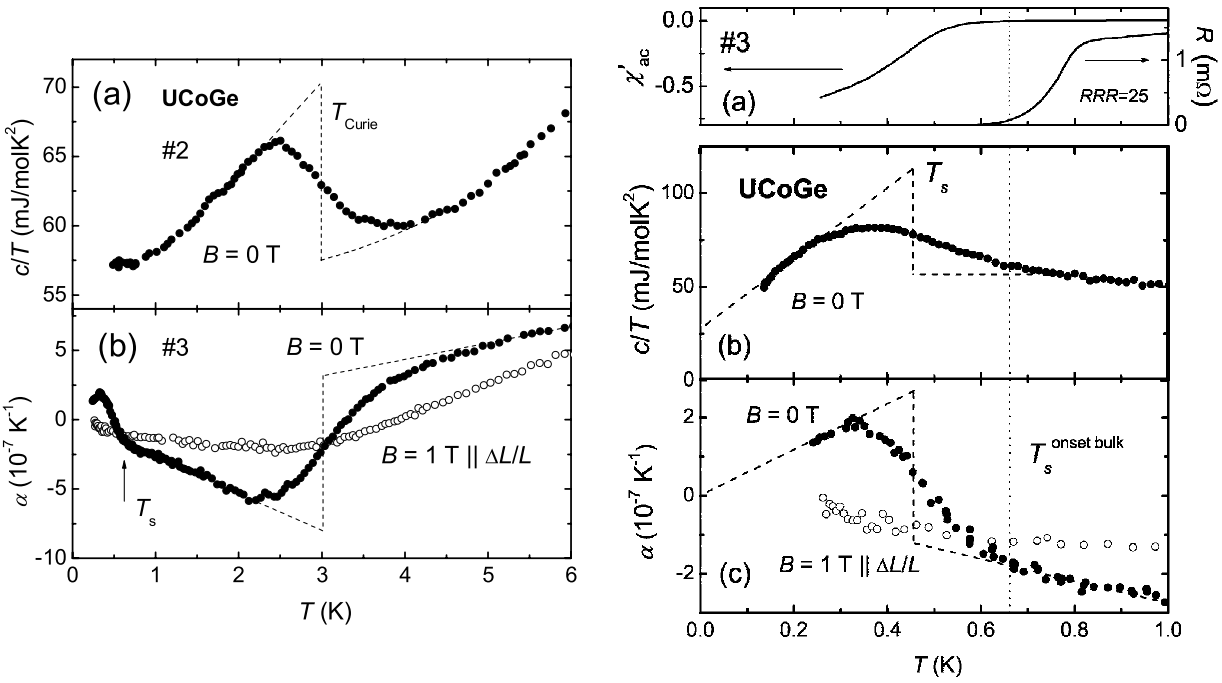

Fig. 4.1 : Left: Specific heat and thermal expansion at low temperature of UCoGe. The transition to ferromagnetism at $T_{Curie} = 3\,\mathrm{K}$ is clearly seen proving that it is a bulk phase. Right: The superconducting transition detected in transport and thermodynamic properties.

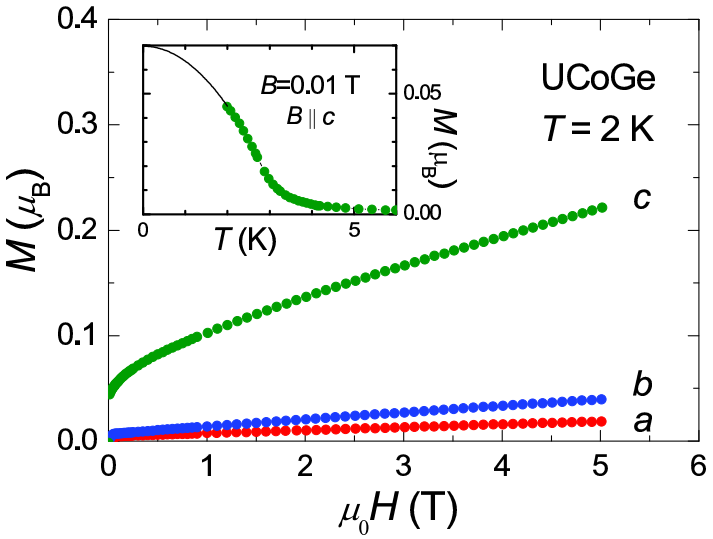

Fig. 4.2 : The magnetization of UCoGe along the three crystallographic axes and in the inlay the temperature dependence of the magnetization at 0.01 T for $H \parallel c$.

ories than UGe_2 (Fay and Appel 1980; Kirkpatrick and Belitz 2003; Roussev and Millis 2001) (see paragraph 1.7) where the moment stays constant up to the critical pressure and jumps clearly at a first order ferromagnetic transition.

In references (Prokleska et al. 2010; Troc et al. 2010), it is reported that not all single crystals show ferromagnetic order but superconductivity is reported in every case if a large RRR is achieved. However, all single crystals grown in Grenoble and Amsterdam clearly show itinerant ferromagnetism.

The first measurements of H_{c2} showed a strong anisotropy of H_{c2} with a small value for $H \parallel c$ which can be explained by Pauli limiting, and values exceeding the Pauli limit for $H \parallel a$ and $H \parallel b$ (Huy et al. 2008). Apparently unconventional spin triplet superconductivity is realized (Huy et al. 2007) for which the absence of paramagnetic limiting was predicted (Klemm and Scharnberg 1985). Additionally, the sensitivity of T_{sc} to the sample quality and hence to impurities is another indication for unconventional superconductivity (Huy et al. 2007).

Aoki *et al.* report measurements on single crystals with similar RRR(Aoki et al. 2009b). However, they find smaller $T_{Curie} = 2.6 - 2.8\,\mathrm{K}$ and $T_{sc} = 0.6\,\mathrm{K}$. They succeeded to determine the H_{c2} curves with very precise alignment shown on the left side of figure 4.3. The H_{c2} curve for $H \parallel a$ has an upturn and the extrapolation to $T = 0$ gives a very high value of $H^a_{c2} = 30\,\mathrm{T}$. The shape of the curve and the extrapolated value are very sensitive to the angle as shown on the right side of figure 4.3. The H_{c2} curves for different angles between $H \parallel a$ and $H \parallel c$ are shown. The inlay gives the angular dependence of the $T = 0$ extrapolated value for H_{c2}. It is clear that a small misalignment of only 3° decreases the H_{c2} value by more than a half.

The curve for $H \parallel b$ shows an interesting S shape. Superconductivity is enhanced at around 11 T. This behavior is an analog to URhGe. In this compound, superconductivity is suppressed in field (Hardy and Huxley 2005). A second superconducting dome appears at fields of around 12 T applied along the b axis, the same field where a reorientation transition occurs (Levy et al. 2005). In UCoGe, the two superconducting regions seem to touch. Figure 4.4 again shows the field dependence of T_{sc} but also T_{Curie} for $H \parallel b$. T_{Curie} is suppressed with field and seems to go to zero near the maximum of T_{sc}. In both compounds the coefficient A of the T^2 term of the resistivity increases near the field (Miyake et al. 2008, 2009) where the superconductivity is enhanced implying that superconductivity is mediated by magnetic fluctuations.

Microscopic probes like NMR (Ohta et al. 2008, 2010) and μSR in zero external field (de Visser et al. 2009) prove the microscopic coexistence of ferromagnetism and superconductivity. Neutron scattering shows that at low field, the magnetic moment is located at the uranium atoms.

As mentioned above, from thermal expansion and heat capacity measurements on polycrystalline UCoGe it was predicted that $\frac{dT_{Curie}}{dP} = -2.5\,\mathrm{K/GPa}$ and $\frac{dT_{sc}}{dP} = +0.48\,\mathrm{K/GPa}$ by applying the Ehrenfest relation (Huy et al. 2007). Assuming a linear P variation for $T_{Curie}(P)$, a critical pressure of $P_c \approx 1.2$ GPa is expected. From measurements on single crystals, the slopes are much higher ($\frac{dT_{Curie}}{dP} = -7.9$ K/GPa and $\frac{dT_{sc}}{dP} = +0.98$ K/GPa (Gasparini et al. 2010)) and the critical pressure is below 1 GPa. In any case UCoGe is a weak ferromagnet close to the critical point at ambient pressure and therefore meets important requirements to correspond to the theoretical model of a weak ferromagnet near a second order critical point. Our main aim was to determine the pressure dependence

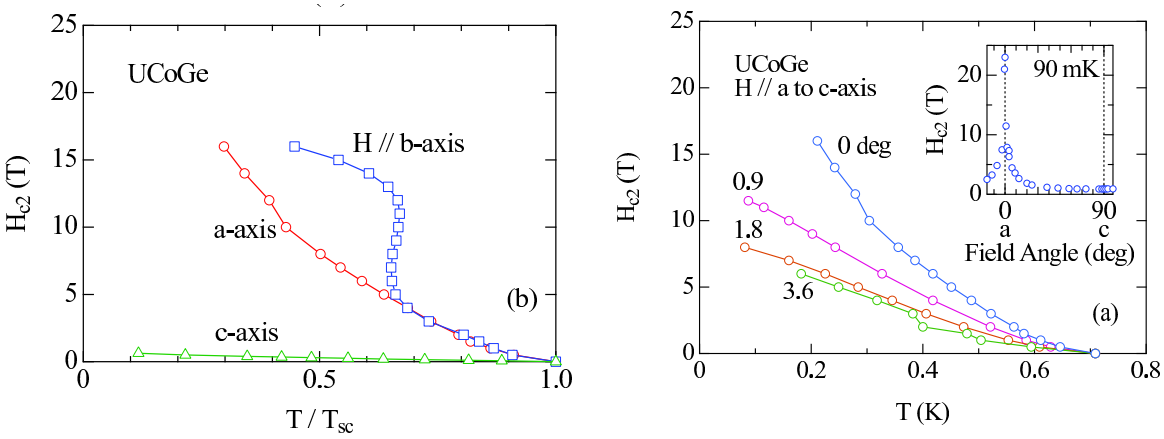

Fig. 4.3 : Left: H_{c2} curves along the three crystallographic axes. As the data stem from different samples with different T_{sc}, the temperature is normalized to the zero field value for clarity. Right: H_{c2} curves for different angles near the a axis. The inlay shows the angular dependence of the extrapolated value of H_{c2} for $T = 0.09\,\mathrm{K}$. (Aoki et al. 2009b)

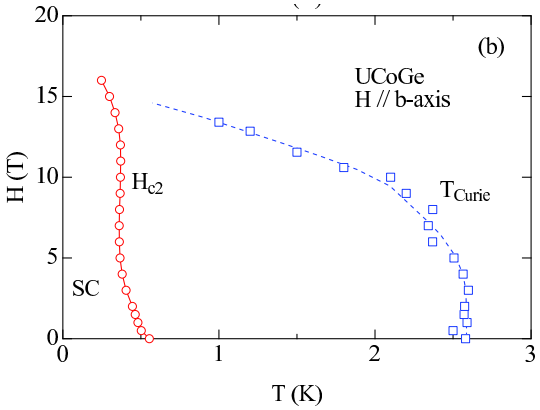

Fig. 4.4 : The phase diagram of UCoGe for a magnetic field $H \parallel b$ (Aoki et al. 2009b). Similar as in URhGe at the field where T_{Curie} is suppressed, the superconductivity is enhanced.

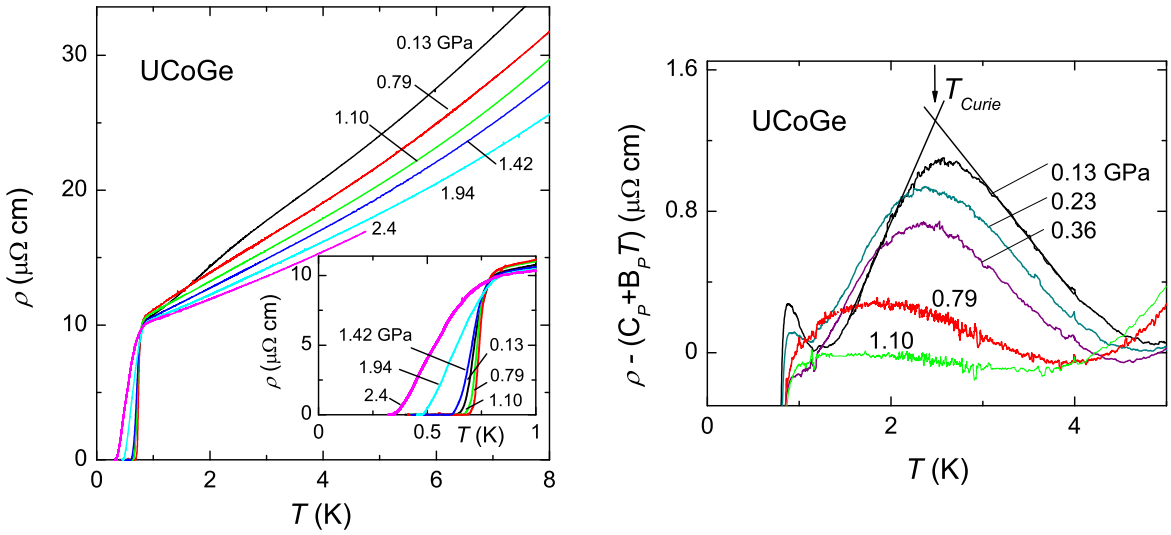

Fig. 4.5 : Left: Resistivity (T, P) of UCoGe for different pressures between 0.13 GPa and 2.4 GPa. The inset shows a zoom into the low temperature region with the superconducting transition, which is seen for all measured pressures. Right: Determination of the Curie temperature T_{Curie} in UCoGe: A straight line (resistivity linear in T) has been subtracted from the resistivity data for each pressure to see clearly the transition temperature which has been determined by the crossing point of the two tangents here presented for $P = 0.13$ GPa.

of T_{sc} in the proximity to this pressure.

4.2 Results

4.2.1 Phase diagram by resistivity of a polycrystal

The first measurements of the pressure phase diagram of UCoGe were performed on polycrystalline samples. With an $RRR \approx 28$, the quality is comparable with the quality of the samples reported in (Huy et al. 2007).

In figure 4.5 on the left the resistivity as a function of temperature for different pressures is shown. The absolute value of the resistivity of this polycrystalline sample is normalized to $\rho = 250$ $\mu\Omega$cm at room temperature, which was estimated from the resistivity of URhGe. At the lowest pressure, the anomaly at $T_{Curie}(\rho)$ is visible as a very small broad anomaly, which becomes even less pronounced for higher pressures. Therefore the ferromagnetic transition temperature is difficult to define. The maximum in the temperature derivative of the resistivity curves does not provide a reasonable criterion to locate $T_{Curie}(\rho)$. The preferable method we found was to subtract a straight line $(C_P + B_P T)$ from each resistivity curve. The obtained curves up to 1.1 GPa are shown on the right side of figure 4.5. In that way, the transition is clearly visible and can be defined by a tangential method as presented for $P = 0.13$ GPa. For 1.1 GPa, the behavior is rather flat and no transition temperature can be defined. Nevertheless there may be some residual fraction of the FM transition. The initial broadness of the anomaly and this special behavior give strong indications that there may be a distribution of Curie temperatures within the sample.

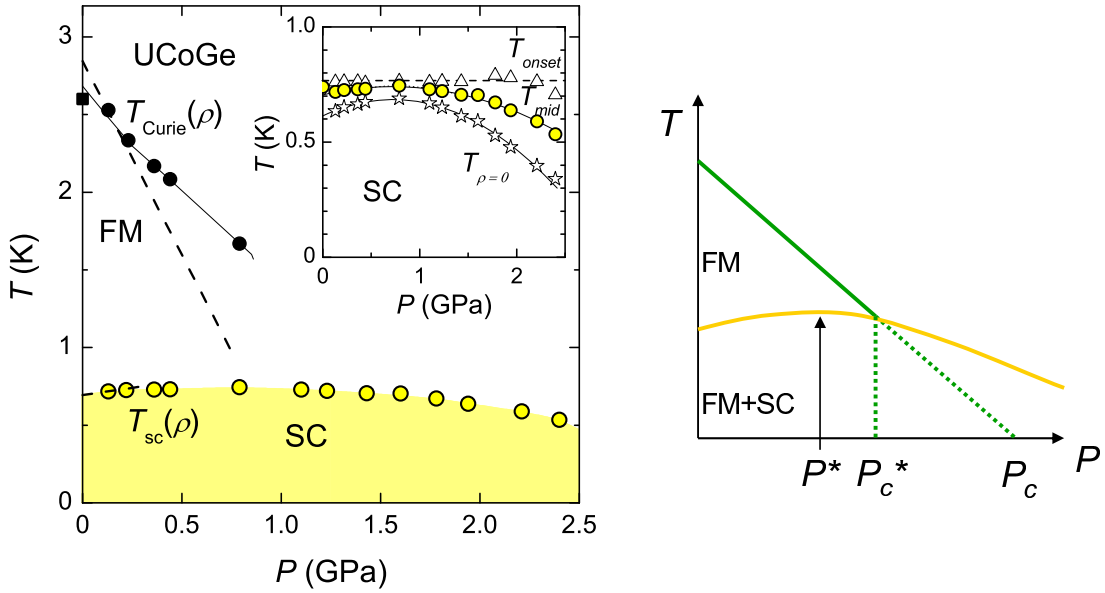

Fig. 4.6 : Left: Phase diagram (T, P) of UCoGe from resistivity measurements with the ferromagnetic (FM) phase and the superconducting (SC) phase. The dashed lines indicate the slopes of the transition lines calculated from Ehrenfest relation at ambient pressure (Huy et al. 2007). In the insert the onset-, midpoint- and zero-resistivity temperatures of the superconducting transition are shown. Lines are guides to the eye. Right: Schematic presentation of the phase diagram to visualize the definitions of the characteristic pressures appearing in the text.

The insert on the left side of figure 4.5 gives a close up of the superconducting transition from resistivity measurements for different pressures. Superconductivity has been observed up to the highest measured pressure of $P = 2.4$ GPa. The superconducting transition temperature $T_{sc}(\rho)$ is defined by the midpoint of the transition in the resistivity.

The phase diagram obtained from these measurements is shown on the left side of figure 4.6. The dashed lines indicate the slopes of $\frac{dT_{Curie}(\alpha)}{dP} = -2.5$ K/GPa and $\frac{dT_{sc}(\alpha)}{dP} = 0.48$ K/GPa as determined from the Ehrenfest relation by the specific heat and thermal dilatation (α) anomaly (Huy et al. 2007) of a polycrystal. The obtained slopes from this high pressure study are different, $\frac{dT_{Curie}(\rho)}{dP} = -1.4$ K/GPa and $\frac{dT_{sc}(\rho)}{dP} = (0.1 \pm 0.05)$ K/GPa but agree in sign. Later measurements on single crystalline samples at ambient pressure now indicate even higher slopes (Gasparini et al. 2010). An interpolation of the higher $T_{Curie}(\rho)$ data to ambient pressure gives a $T_{Curie}(\rho)$ of 2.7 K. The insert of figure 4.6 shows the temperature of the onset (T_{onset}), midpoint (T_{mid}), and zero resistivity ($T_{\rho=0}$) of the superconducting transition in an enlarged scale as a function of pressure. Under pressure T_{mid} and $T_{\rho=0}$ first increase and then decrease with a maximum of $T_{sc}(\rho) = T_{mid} = 0.75$ K at $P = 0.8$ GPa. The onset temperature T_{onset} however depends weakly on pressure (see figure 4.2.1d).

The phase diagram of UCoGe obtained from these measurements appears different from the ones of UGe_2 and URhGe (see paragraph 1.7). In contrast to UGe_2 and URhGe, the SC temperature appears to be almost independent of P and insensitive to the transition at P_c (definition of characteristic pressures see the scheme on the right side of figure 4.6). In the first approximation P_c may be respectively expected at 2.1 GPa from a lin-

ear extrapolation of the low pressure data of $T_{Curie}(\rho)$. However, as the transition from the ferromagnetic to the paramagnetic state may be of first order, as generally expected for ferromagnetic quantum phase transitions (Belitz et al. 1999; Chubukov et al. 2004), the real critical pressure P_c is probably below 2.1 GPa. This is in agreement with the statement that when T_{Curie} becomes lower than T_{sc} above $P_c^\star$, FM will not survive as the SC gap opening precludes the establishment of long range order. The critical pressure for FM $P_c^\star$ can therefore be estimated from the crossing point between the transition lines from resistivity and thermal dilatation with the superconducting transition $T_{sc}(P)$ as $P_c^\star(\rho) \approx 1.2$ GPa. It is interesting to note that $P^\star \sim P_c^\star$ ($P^\star$ is the pressure, where T_{sc} is maximum).

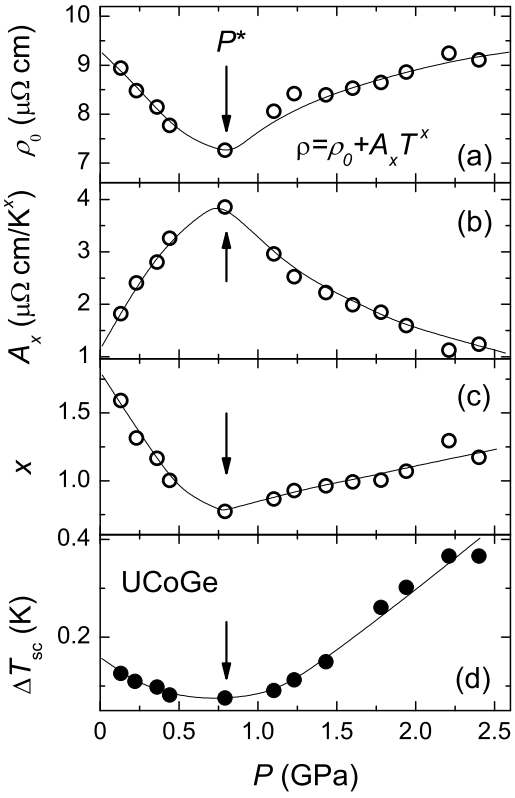

Fig. 4.7 : (a-c) Pressure dependence of the fit parameters of a $\rho = \rho_0 + A_x T^x$ fit in the normal state for T <1.7 K in UCoGe. The clear anomaly at $P^\star \sim 0.8$ GPa reflects the pressure where the broad transition passes through this temperature region. It corresponds to the pressure where the superconducting transition is the narrowest (d). The lines are guides to the eye.

Another mark of unusual behavior appears in the analysis of the resistivity data according to the equation $\rho = \rho_0 + A_x T^x$ in the normal state for $T < 1.7$ K as shown in figure 4.2.1. The T^2 Fermi-liquid law is only found at low pressure. From the P variation of the residual resistivity ρ_0, the A_x coefficient and the derived exponent x of these fits as well as from the apparent estimated SC broadening, clearly a characteristic pressure of $P^\star \sim 0.8$ GPa emerges. A quite unusual result is the quasi-invariance of $x \sim 1$ above $P^\star$. The difficulty to recover T^2 Fermi liquid law on both sides of of the first order quantum critical point has now been established in many systems, notably for MnSi (Doiron-Leyraud et al. 2003) and $ZrZn_2$ (Takashima et al. 2007). However, x is often very near to 1.5 while here it is more close to 1. Of course, we cannot exclude that a Fermi liquid state with a clear T^2 temperature dependence of the resistivity appears only at a temperature lower than T_{sc}. The coincidence under pressure between a maximum of T_{sc} and a minimum in the width of the SC transition is a common feature in pressure experiments. The fast increase of the broadening of the SC transition above $P^\star$ may

indicate a rapid pressure dependence of the SC volume fraction. This suggests that $P_c^\star$ may be not so far above $P^\star$ and the critical pressure for the collapse of SC will coincide with $P_c^\star$ as in UGe_2 in high purity crystals.

Due to the long range nature of FM, the sample purity may play a key role in the electronic properties close to the ferromagnetic instability. This question becomes critical for a weak first order transition as expected for UCoGe. UGe_2 may be rather "clean" as Δm_0 =1 μ_B/U, while in UCoGe Δm_0 may be near 10^{-2} μ_B/U.

Even the previous reports point out the heterogeneity of the phase transition at T_{sc} but also at T_{Curie}. For example in the first publication about UCoGe the resistivity onset of superconductivity at $T_{sc} = 0.8$ K is far above the maximum of the SC specific heat anomaly at $T_{sc} \sim 0.45$ K (Huy et al. 2007). The difficulty to achieve a homogeneous state may also be indicated in NMR and NQR results (weak fraction of SC volume, no exponential behavior of magnetization recovery) (Ohta et al. 2008).

If we assume that the superconducting phase exists only within the ferromagnetic state as in UGe_2 and if there is heterogeneity in the FM then the resistivity is not suitable to test the boundary of bulk superconductivity because a remaining fraction of FM may lead to partial superconductivity in the sample and hence the apparent weak pressure dependence of T_{sc} detected by resistivity. As recently demonstrated for the uranium-based heavy fermion superconductor URu_2Si_2, the SC phase boundary obtained by resistivity measurements can be very different from that measured by specific heat (Hassinger et al. 2008). Furthermore in URu_2Si_2 the collapse of bulk SC is at $P_x = 0.5$ GPa, when the hidden order phase switches to the antiferromagnetic ground state, while resistivity data indicate the suppression of SC between 1.3 GPa and 2 GPa.

Experimentally the surprising observation was the difficulty to modify SC under pressure. However our feeling is that this unexpected behavior is linked to the simultaneous high sensitivity of FM and SC anomalies to imperfections. The measurements presented here show that even for a RRR near 30, large smearings occur in FM and SC transitions. In heavy fermion systems with an antiferromagnetic instability, the smearing appears mainly for the SC transition. Furthermore, it is interesting to note that in contrast to antiferromagnetically ordered systems like $CeRhIn_5$ (Knebel et al. 2006) or $CeIrSi_3$ (Tateiwa et al. 2007), in UCoGe the SC transition is sharper in the ordered regime than in the paramagnetic state.

There are strong indications for a critical behavior at $P^\star \sim 0.8$ GPa. The apparent strong deviations from Fermi liquid behavior above $P^\star$ is a remarkable fact which may be due to a surviving FM cluster.

4.2.2 Phase diagram of a single crystal

Ac susceptibility and resistivity

The first available "almost" single crystals (polycrystals with very large single crystalline grains) which were used for this study had an $RRR = 6$.

Figure 4.8 shows the results of ac-susceptibility and resistivity measurements at different pressures. The setup is shown in figure 2.4. In the susceptibility (figure 4.8a), the ferromagnetic transition is clearly visible as a maximum. The transition temperature T_{Curie} was defined as the temperature of the maximum. With pressure, the maximum

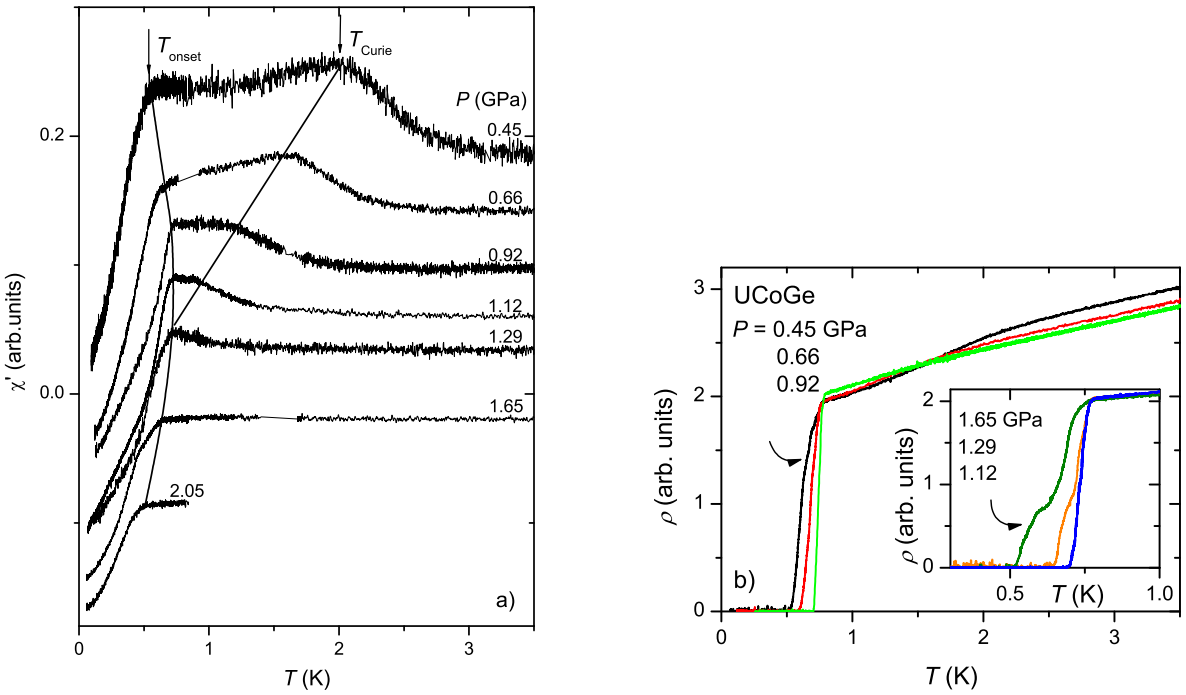

Fig. 4.8 : a) Real part of ac-susceptibility at different pressures. b) Resistivity at the same pressures.

shifts to lower temperatures and is strongly attenuated. The superconducting temperature T_{sc}, defined as the onset temperature of the shielding signal, increases with pressure up to around 1.1 GPa and then decreases again. At 1.65 GPa, there is no sign of a ferromagnetic transition, i.e. a completely flat behavior characteristic of a material far from a FM instability is restored above T_{sc}. The signal of the diamagnetic shielding seems to decrease with pressure. This could be interpreted as a decreasing volume of the superconducting phase in the sample. In the pressure study by Slooten *et al.* (Slooten et al. 2009) the diamagnetic signal is independent of pressure. Their better sample quality could be an explanation for this behavior.

In the resistivity (figure 4.8b) the anomaly at T_{Curie} is rather broad and we do not observe a well defined feature. This is similar as in the polycrystal. It may be due to the rather low sample quality ($RRR \approx 6$). The broad anomaly shifts to lower temperatures and is also attenuated. The superconducting transition width goes through a clear sharp minimum at ≈ 1.1 GPa. The onset temperature of the superconducting transition does not change with pressure, only $T_{sc}(\rho = 0)$ changes. Below $P = 1.2$ GPa $T_{sc}(\rho = 0)$ corresponds exactly to the T_{sc} defined as above from susceptibility. Therefore we chose this criterion to define T_{sc} from resistivity in the phase diagram. Above this pressure, $T_{sc}(\rho = 0)$ is slightly lower. Interestingly, above this pressure also a double step behavior develops which is not seen at low pressures.

Ac calorimetry

Ac calorimetric measurements have been carried out on a small single crystal. The pressure cell was set up to have $H \parallel a$ (see figure 2.3). As resistivity and ac susceptibility can

show zero resistivity and a diamagnetic signal even though the superconducting phase is not bulk, the aim of this study was to prove that the superconducting state above the critical pressure is bulk. We measured in zero field at ambient pressure, without a pressure transmitting medium in order to have a reference signal, and at high pressure $P = 1.65\,\mathrm{GPa}$, which is above the critical pressure, if T_{Curie} from ac susceptibility is extrapolated linearly (see the phase diagram figure 4.11). The detected superconducting anomalies at these two pressures are shown in figure 4.9. The anomalies are rather broad

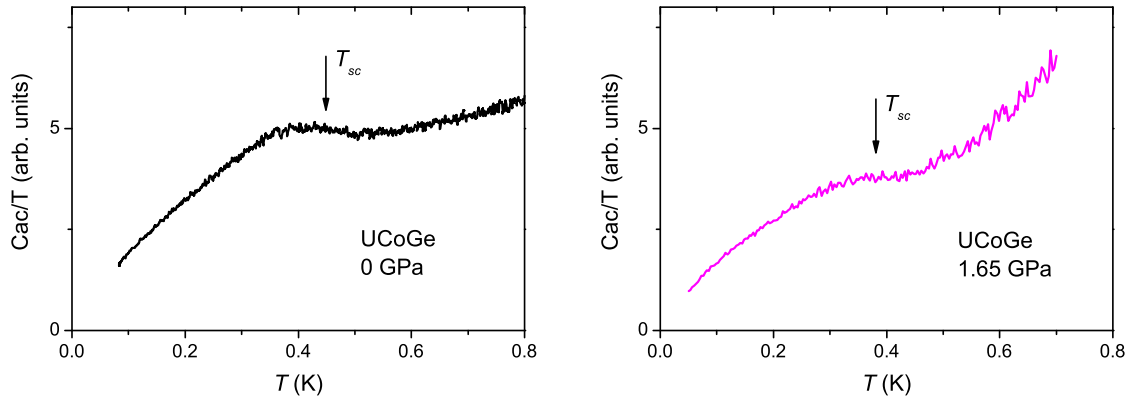

Fig. 4.9 : Ac specific heat at low temperature of UCoGe for the lowest and the highest measured pressures. The transition is clear on both sides of the critical point proving that the bulk superconducting phase extends into the paramagnetic state.

and the background signal is different with or without pressure medium (both measurements are taken at different frequencies), but both anomalies have a similar amplitude and transition temperature. Knowing that the superconducting phase is bulk at ambient pressure, this proves that the superconductivity is also bulk at high pressure in the paramagnetic phase.

By decreasing the pressure, I tried to establish the total pressure phase diagram in order to know if the ferromagnetic transition survives inside the superconducting phase. Unfortunately, just above the pressure, where T_{Curie} and T_{sc} cross each other, there were problems with the pressure cell. However, in the measurement at 1.3 GPa, just above the pressure where $T_{sc} = T_{Curie}$, only one transition was found. This implies that the transition line T_{Curie} is very steep in the superconducting phase.

The H_{c2} curves were established for the measured pressures and are shown in figure 4.10. As H_{c2} is very angular dependent especially for H close to $H \parallel a$ (Aoki et al. 2009b), it is unclear whether the effect of an increase of H_{c2} observed here is due to a change in the sample position in the pressure chamber (for example during loading) or due to pressure. Similarly, pressure measurements by Slooten *et al.* (Slooten et al. 2009) also report an increase of H_{c2} with pressure, but the pressure dependence is not continuous and the $P = 0$ value does not agree with the H_{c2} curve for a well aligned sample (Aoki et al. 2009a). Nevertheless, it is important to note that H_{c2} does not decrease significantly in the paramagnetic state. This leads to the suggestion that even in the paramagnetic state spin triplet superconductivity is realized.

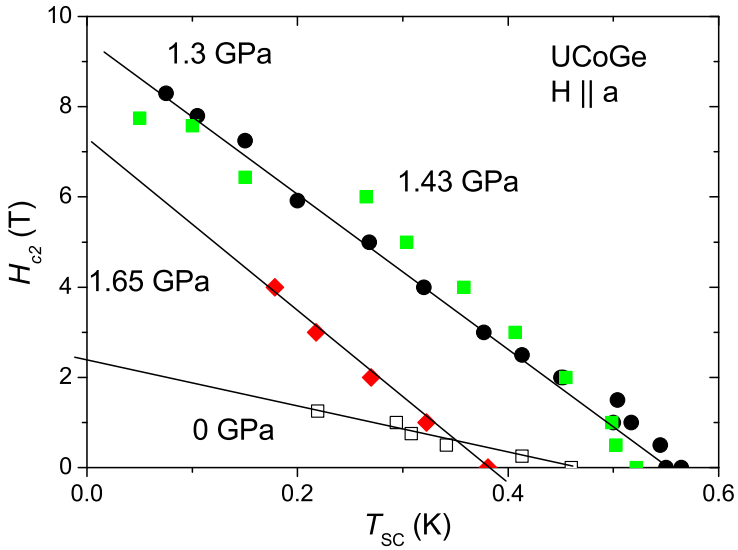

Fig. 4.10 : H_{c2} curves for different pressures in UCoGe with $H \approx\| a$. As H_{c2} depends very sensitively on the angle and the precise alignment of the sample in the cell changes during loading or pressure changes, the effects observed here are probably due to a misalignment of the sample in the field.

Pressure phase diagram

Figure 4.11 shows the pressure-temperature phase diagram established from these and previous measurements. The qualitative behavior of the phase transitions is the same as from the polycrystal. Above 0.5 GPa the Curie temperature T_{Curie} decreases linearly with pressure but the slope is steeper than in the previous phase diagram. The superconducting phase is dome-like with the maximum T_{sc} at the pressure where the ferromagnetic transition line meets the superconducting phase boundary $P_c^\star = 1.25\,\mathrm{GPa}$. It extends up to the highest measured pressure $P = 2.4\,\mathrm{GPa}$.

The phase diagram presented here corresponds to scenario b) in figure 1.9. It is different from theoretical predictions, where a minimum in T_{sc} is expected at the critical pressure (Fay and Appel 1980; Roussev and Millis 2001). It is also different to the phase diagrams of other ferromagnetic superconductors, namely UGe_2, where the superconducting phase lies entirely within the ferromagnetic region and no superconducting phase appears in the paramagnetic (PM) regime (Saxena et al. 2000). But in UGe_2, SC is directly linked to the transition between its two competing ferromagnetic states (FM1 and FM2) (Pfleiderer and Huxley 2002). From the presented data however, it is clear that in UCoGe SC appears also in the PM state. An extrapolation of T_{Curie} to 0 K would give a quantum critical point (QCP) close to $P_c = 1.6\,\mathrm{GPa}$. Up to now, the real behavior of the ferromagnetic transition in the pressure region from $P_c^\star$ up to P_c is not clear. Compared with the phase diagram from measurements on a polycrystal, the pressure where T_{sc} is maximum is slightly enhanced (before $P^\star \approx 0.8\,\mathrm{GPa}$, now it is the pressure where the two transition lines meet $P_c^\star = P^\star \approx 1.2\,\mathrm{GPa}$) as predicted before. Below this pressure, the transition temperatures T_{sc} determined from the onset of the diamagnetic signal in ac susceptibility and zero resistivity are the same, above this pressure they differ slightly.

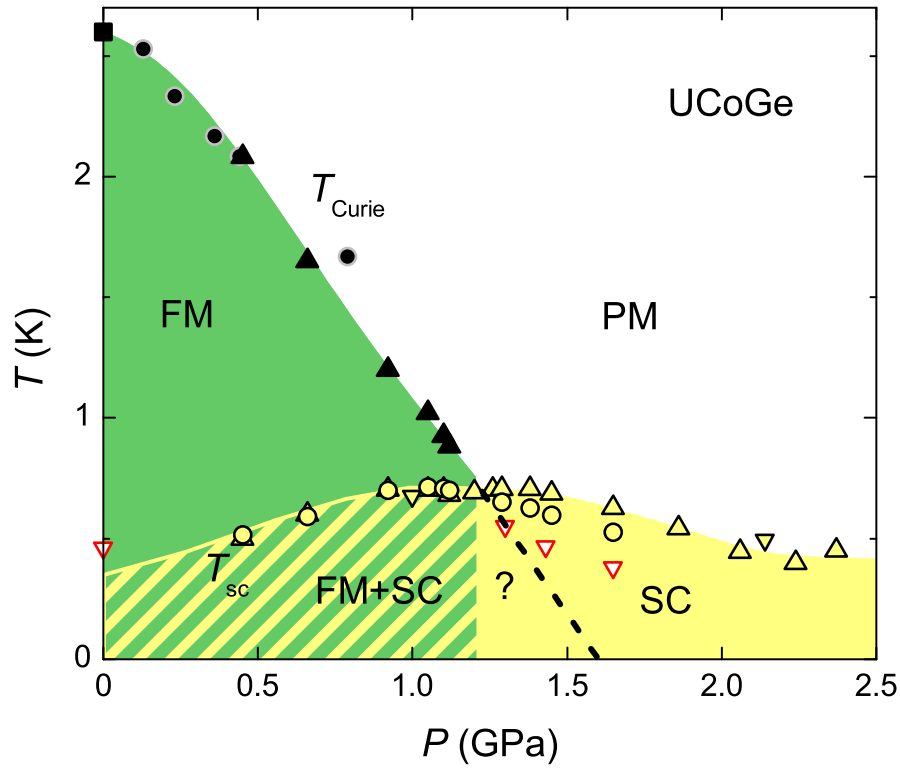

Fig. 4.11 : Pressure-temperature phase diagram of an almost single crystalline sample of UCoGe by susceptibility (upward triangles: ac-susceptibility, round black dots: previous results on polycrystal, downward triangles: ac calorimetry) and empty dots resistivity. The gray circles are from previous measurements on a polycrystal.

T_{sc} from ac calorimetry at high pressure is lower than T_{sc} from the other methods, but the pressure dependence seems very similar to the pressure dependence of T_{sc} from resistivity.

A very similar phase diagram has been published at the same time as our phase diagram (Slooten et al. 2009). It is shown in figure 4.12. Even the non-linear behavior of T_{Curie} at low pressures is also present in their paper and the pressure, where $T_{Curie} = T_{sc}$ is $P_c^\star = 1.16\,\mathrm{GPa}$, very similar to the pressure determined in this study. The pressure phase diagram established here can therefore be seen as well established.

In the ferromagnetic state, the superconducting order parameter breaks gauge symmetry, the crystal symmetry and time reversal symmetry, whereas in the paramagnetic state, time reversal symmetry is not broken (Mineev 2009). Hence, it is in principle possible to have different order parameters in the two states with a transition line in between. This transition can be of second order (Mineev 2009). The fact that $T_{sc}(P)$ is a smooth curve through the critical point is therefore interesting.

Let us discuss possible scenarios of the phase diagram of a ferromagnetic superconductor in the two cases of a first order or a second order ferromagnetic transition. Figure 4.13a represents the hypothetical variation of FM in a first order quantum transition (FOQT) (Belitz et al. 1999) neglecting any feedback of SC (filled area); the dashed line is the hypothetical extrapolation of a second order quantum critical point (QCP). For clarity, the difference between the FOQT and the QCP has been exaggerated. In figure

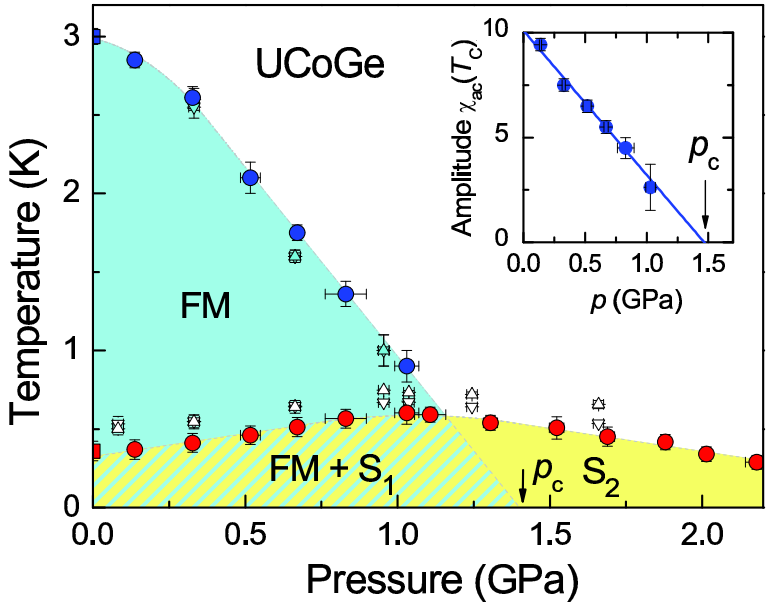

Fig. 4.12 : Pressure-temperature phase diagram on a single crystal by reference (Slooten et al. 2009).

4.13b the superconducting dome centered near the FOQT is shown (filled area), assuming that the first order nature of FM wipes out the SC minimum at the QCP (dashed line (Fay and Appel 1980; Roussev and Millis 2001)) as experimentally observed. Figure 4.13c represents what may be the result of the interplay between FM and SC including a feedback between the two phases. In a narrow regime one may go from the PM to the simple SC phase and then to the FM+SC coexisting phase. The situation will be rather similar to the one found in the antiferromagnetic (1,1,5) Ce compound $CeRhIn_5$ under pressure (Knebel et al. 2006; Yashima et al. 2007). However, this pressure region is very small as it is extracted from the specific heat measurement just above the pressure where the two transition lines meet, which only shows the superconducting anomaly.

4.3 Conclusion

The pressure-temperature phase diagram of UCoGe has been established first on a polycrystal by resistivity measurements and then by simultaneous ac-susceptibility and resistivity measurements on an almost single crystal and by ac calorimetry on a single crystal.

The ferromagnetic transition seen in a maximum of the susceptibility is suppressed with pressure. The superconducting temperature increases slightly and has a maximum at $P_c^\star = 1.25\,\mathrm{GPa}$ where $T_{Curie} = T_{sc}$. The phase diagram is different from the one of UGe_2 in that the superconducting state continuously extends from the ferromagnetic state into the paramagnetic state up to the highest measured pressure $P = 2.4\,\mathrm{GPa}$. No minimum in T_{sc} is detected at the critical pressure.

The sample quality is still a problem in UCoGe. The anomalies detected in specific heat are broad, in resistivity, a two step behavior appears for high pressures. Measure-

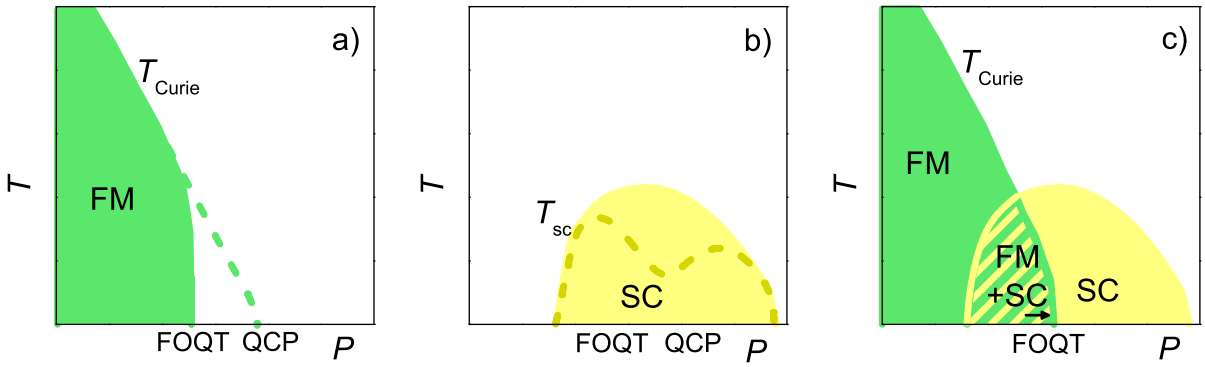

Fig. 4.13 : Behavior of superconductivity and ferromagnetic phases at a first order (solid line) or second order (dashed line) phase transition.

ments on better samples will show if this is an intrinsic property or not.

With increasing sample quality, quantum oscillation measurements will be possible. Existing electronic band structure calculations (de la Mora and Navarro 2008; Divis 2008; Samsel-Czekala et al. 2010) can then be tested.

Conclusion

This thesis presents results on two very different uranium based heavy fermion compounds, the "hidden order compound" URu_2Si_2 and the ferromagnetic superconductor UCoGe.

Various measurement techniques under pressure and in high magnetic fields were used to explore the ground states of these materials in a wide parameter space. Resistivity, ac susceptibility and ac calorimetry measurements were carried out in a diamond anvil cell and in a piston cylinder pressure cell. The extreme measurement conditions were pressures up to 2.4 GPa, temperatures down to 20 mK and magnetic fields up to 13 T.

The pressure phase diagram of URu_2Si_2 is nowadays well established. The approach of comparing the electronic and magnetic properties in the hidden order (HO) phase and the pressure induced antiferomagnetic (AF) phase has contributed to the understanding of the HO parameter. An important result was the identification of the significant magnetic excitation in the HO state by inelastic neutron scattering spectroscopy. It was the first hint that the ordering vector of the HO could be the same as the AF ordering vector which is supported by the order-parameter like temperature dependence of the intensity of the excitation. It is a natural explanation for the similarity of the resistivity or specific heat anomalies at the phase transition in both phases.

Until the HO parameter is observed directly it is unclear which symmetries are broken. However, when a crystal symmetry is broken it has usually an influence on the Fermi surface. The Fermi surface study on URu_2Si_2 at ambient pressure and under pressure by Shubnikov-de Haas measurements presented in this work is an important experimental result[1] and a step in the elucidation of the HO parameter. These measurements, where more than 50 % of the Fermi surface was detected, enable the comparison of theory with experiment i.e. of the calculated Fermi surface for a proposed HO parameter with the measured Fermi surface .

The angular dependence of the SdH frequencies, their small absolute values and their insensitivity to pressure are in good agreement with a change of symmetry from body centered tetragonal in the paramagnetic state to simple tetragonal in both the HO and AF states. This can be explained by the fact that the crystal symmetry is the same in both HO and AF state due to the same ordering vector.

Up to now, the only band structure calculation to compare with the results is by Elgazzar et al. (2009) and Oppeneer et al. (2010) in the antiferromagnetic state. The agreement is quite good. There are two other recent proposals for the HO parameter (quadrupolar order by Harima (2010) and hexadecapolar order by Haule and Kotliar (2009)) with the same ordering vector. However, in both cases the order parameter

[1] A detailed summary of the results is found in the conclusion of chapter 3.

has not been included in band structure calculations with the three dimensional FS and the angular dependence of the frequencies. It will be interesting to see whether their calculations describe the experimental data even better or whether it is still too difficult to take into account the important electronic correlations and magnetic fluctuations in this compound.

The experimental challenge is now to detect the missing orbit and to find experimentally an orbit with a larger effective mass for $H \parallel a$. Up to now, it is difficult to calculate the effective masses in band structure calculations. Surprisingly, there is no microscopic model which links the strong magnetic fluctuations along c with the anisotropy of the effective masses.

For the second part of this work, the pressure phase diagram of the ferromagnetic superconductor UCoGe was established by resistivity and susceptibility measurements. The ferromagnetic transition is suppressed with pressure and can be followed up to the pressure where its transition temperature becomes as low as the superconducting transition temperature $P_c^\star = 1.2\,\mathrm{GPa}$. The superconducting phase extends into the paramagnetic state up to the highest pressure measured of 2.4 GPa. The bulk nature of superconductivity in the paramagnetic state was confirmed by ac calorimetric measurements at 1.6 GPa. The superconducting phase forms a dome with a maximum transition temperature at $P_c^\star$ where $T_{Curie} = T_{sc}$. In contrast to theoretical predictions no minimum is observed at this pressure.

Still open questions are the behavior of T_{Curie} when it becomes smaller than T_{sc} and the order of the ferromagnetic transition. To answer these questions a complete ac calorimetric study of the phase diagram is necessary.

This compound seems to have properties in common with the other ferromagnetic superconductors such as a reentrant superconducting phase linked either to metamagnetism as in UGe_2 or to a reorientation transition in field as in URhGe. However, there are many open questions left. It would be interesting to see if the ferromagnetic phase transition ends at a theoretically predicted tricritical point and if a "wing diagram" is observed as in UGe_2. Ferromagnetic superconductors present a new and open field of study. Two key points for further progress are the crystal quality and the discovery of an ideal system such as the 1,1,5 Ce systems which are ideal cases to study the interplay of antiferromagnetism and superconductivity in heavy fermion compounds.

Appendix

4.4 Résumé

Dans cette thèse, deux systèmes de fermions lourds à base d'uranium sont étudiés sous pression.

L'état fondamental en dessous de $T_0 = 17.5\,\mathrm{K}$ dans URu_2Si_2 est appelé "ordre caché" (HO, de l'anglais hidden order), parce que le paramètre d'ordre n'a pas encore été trouvé. Le système devient de plus supraconducteur à basse température. Sous pression, le système devient antiferromagnétique (AF) au dessus d'une pression critique. Des mesures Shubnikov-de Haas sous pression montrent que la surface de Fermi ne change pas entre les deux phases. Dans la phase AF, le doublement de la maille implique une reconstruction de la surface de Fermi. Étant donné que celle-ci ne change pas sous pression, ce doublement doit déjà avoir lieu dans la phase HO. Nos mesures de la dépendance angulaire des fréquences d'oscillations supportent des calculs de bandes récents traitant les électrons $5f$ des atomes d'uranium comme itinérants.

Dans la deuxième partie de ma thèse, j'ai étudié le diagramme de phase sous pression du supraconducteur (SC) ferromagnétique (FM) UCoGe ($T_{Curie} = 2.8\,\mathrm{K}$, $T_{sc} = 0.6\,\mathrm{K}$). Les mesures de résistivité, ac calorimétrie et ac susceptibilité montrent que la phase FM est supprimée à 1 GPa mais que la phase SC subsiste aussi dans la phase paramagnétique induite par la pression. Ce diagramme de phase est unique dans la classe des supraconducteurs ferromagnétiques.

Mots-Clés

systèmes à fermions lourds
URu_2Si_2, hidden order
UCoGe, supraconducteurs ferromagnétiques
diagramme de phase sous pression
oscillations quantiques

4.5 Introduction française

La variation des paramètres de maille d'un cristal change les interactions électroniques et magnétiques. Si deux états fondamentaux ont une énergie proche, le changement de l'énergie d'échange peut changer l'état fondamental du système. La pression hydro-

statique est alors un paramètre de contrôle propre pour varier l'état fondamental d'un système à électrons corrélés proche d'une instabilité quantique. Les diagrammes de phase sous pression des systèmes à fermions lourds sont souvent riches et dévoilent des nouveaux phénomènes physiques comme le comportement non liquide de Fermi, l'interaction entre magnétisme et supraconductivité, la coexistence du ferromagnétisme et de la supraconductivité ou des phénomènes de criticalité quantique. Dans cette thèse, deux systèmes à Fermions lourds à base d'uranium avec des diagrammes de phases intéressants ont été étudiés.

Le composé URu_2Si_2 a un état fondamental mystérieux qui apparaît en dessous de la température critique $T_0 = 17.5\,\mathrm{K}$ à pression ambiante. Malgré 25 années de recherche, le paramètre d'ordre de cette phase n'a pas été identifié, si bien qu'on lui donne le nom d'ordre caché (HO, de l'anglais hidden order). Le problème fondamental est qu'à la transition, beaucoup d'entropie (0.2Rln2) est relâché, mais la phase est non-magnétique. Le système passe à l'état supraconducteur à basse température. Une panoplie de théories existe pour un paramètre d'ordre qui fournit une telle perte d'entropie; par exemple différents types d'ordres orbital, des ondes de densité de spin dynamiques, l'ordre hélicoïdal, des ondes d'hybridisation... En revanche, il n'a pas été possible de détecter le paramètre d'ordre expérimentalement.

Sous pression, l'état fondamental devient antiferromagnétique (AF) et la supraconductivité est supprimée à la même pression. Même si la phase HO et la phase AF sont séparées par une ligne de transition de phase de premier ordre, beaucoup de propriétés physiques ont un comportement similaire en fonction de la température dans les deux phases. Par exemple, l'anomalie en résistivité évoquant la modification de la surface de Fermi est la même pour toutes les pressions.
Par des mesures de diffusion neutronique notre groupe a identifié l'excitation propre de la phase HO au même vecteur de propagation que le vecteur d'ordre de la phase AF Q_{AF}. C'est jusqu'à présent la seule signature microscopique de l'état HO. La dépendance en température de son intensité a le comportement d'un paramètre d'ordre en dessous de T_0. Ceci nous indique que Q_{AF} est aussi le vecteur d'ordre de la phase HO. Dans ce cas, la surface de Fermi, qui est reconstruite à la température d'ordre, va être la même dans la phase HO et dans la phase AF.
Pour voir si la surface de Fermi change, cette étude présente des mesures de l'effet Shubnikov-de Haas à plusieurs pressions sur des nouveaux cristaux de très bonne qualité. Les mesures montrent que la surface de Fermi ne change pas entre les deux phases. De nouvelles propositions pour le paramètre d'ordre de la phase HO ont été publiées avec de très différents degrés de localisation des électrons $5f$ et ainsi de très différentes structures électroniques. Mes mesures de la dépendance angulaire des fréquences d'oscillation permettent de tester la structure électronique ainsi que les nouvelles propositions théoriques du paramètre d'ordre caché toujours inconnu.

La deuxième partie de mon travail se concentre sur un autre composé d'uranium, UCoGe. C'est un des peu nombreux matériaux à la fois ferromagnétique ($T_{Curie} = 2.8\,\mathrm{K}$) et supraconducteur ($T_{sc} = 0.6\,\mathrm{K}$). La compréhension théorique du diagramme de phase d'un supraconducteur ferromagnétique proche de la pression critique est encore incomplète. Tous les composés ferromagnétiques connus ont une transition de premier ordre mais des théories incluant la supraconductivité existent seulement pour une transition de deuxième ordre. Le but de cette expérience est d'établir le diagramme de phase sous pres-

sion de UCoGe, qui est le troisième composé ferromagnétique supraconducteur après UGe_2 et UIr où le point critique peut être atteint par l'application d'une pression. Des mesures précises du diagramme de phase par résistivité, susceptibilité alternative et calorimétrie alternative montrent que la phase ferromagnétique est supprimée à une pression d'environ 1 GPa et que UCoGe est le seul supraconducteur ferromagnétique où la phase supraconductrice s'étend profondément dans la phase paramagnétique du matériau induite par la pression. Le ferromagnétisme est rapidement supprimé lorsque la phase supraconductrice apparait en premier en refroidissant. Le diagramme de phase de UCoGe est alors différent des diagrammes de phases des autre supraconducteurs ferromagnétiques. La phase supraconductrice à l'intérieur de la phase ferromagnétique est continuellement reliée à la phase supraconductrice en dehors de la phase ferromagnétique, bien que le paramètre d'ordre supraconducteur ait des symétries différentes. Il est impossible de déterminer l'ordre de la transition. L'interaction entre le ferromagnétisme et la supraconductivité est un nouveau champ d'étude avec beaucoup d'effets intéressants, par exemple la supraconductivité réentrante sous champ.

Cette thèse est divisée en quatre chapitres.
Le premier chapitre explique brièvement les phénomènes physiques importants dans les composés à fermions lourds.
Les conditions extrêmes de mesures (fort champs magnétique, basse température) et les techniques de haute pression sont décrites dans le chapitre 2.
Le chapitre 3 donne une introduction aux propriétés du composé URu_2Si_2 incluant des résultats de neutrons obtenues pendant ma thèse par notre groupe. Ensuite, les résultats sur la surface de Fermi de URu_2Si_2 à pression ambiante dans la phase HO et sous pression dans la phase AF sont présentés.
Le dernier chapitre présente le diagramme de phase de UCoGe.

4.6 Résumé de chaque chapitre

Chapitre 1

Le premier chapitre traite les phénomènes physiques fondamentaux dans les systèmes à fermions lourds et plus particulièrement dans les composés URu_2Si_2 et UCoGe. La compétition entre l'effet Kondo et l'interaction RKKY amène au diagramme de phase de Doniach avec un point critique quantique. Ceci est une transition de phase à température nulle où l'état fondamental change sous la variation d'un paramètre autre que la température comme par exemple la pression ou le champ magnétique. Proche d'une telle instabilité magnétique, on trouve souvent un comportement dit de non-liquide de Fermi et de la supraconductivité non-conventionnelle. UCoGe est un supraconducteur ferromagnétique, et les théories existantes ainsi que les deux autres matériaux avec cette propriété sont présentés dans ce chapitre.

A la fin du premier chapitre la théorie des oscillations quantiques, notamment des oscillations Shubnikov-de Haas, méthode de mesure de la surface de Fermi dont les résultats sont décrits dans le chapitre 3, est traitée plus en détail.

Chapitre 2

Le deuxième chapitre décrit les méthodes expérimentales utilisées dans cette thèse. La préparation des échantillons par croissance Czochralski, les différentes techniques de mesures comme la résistivité, la chaleur spécifique alternative et la susceptibilité alternative sont introduites avant de mettre en avant les conditions extrêmes de mesure. En plus des très basses températures et du fort champ magnétique, la spécialité de ce laboratoire sont des mesures sous très haute pression. Les techniques d'applications, de mesure et de variation de la pression sont montrées en détail. Ces techniques sont utilisées pour établir le diagramme de phase de UCoGe proche du point critique du ferromagnétisme et pour mesurer et comparer la surface de Fermi dans la phase HO et la phase AF dans URu_2Si_2.

Le dernier paragraphe explique les aspects techniques de l'analyse des mesures de Shubnikov-de Haas par un programme de traitement de données (Matlab) en utilisant les transformés de Fourier rapide (FFT de l'anglais Fast Fourier transforms).

Chapitre 3

En première partie, le chapitre 3 introduit le composé URu_2Si_2 et plus précisément les mesures de neutrons effectuées sur ce composé pendant cette thèse par notre groupe. Les résultats sur URu_2Si_2 par mesures de résistivité et magnétorésistance et l'effet Shubnikov-de Haas sont présentés ensuite. D'abord, la surface de Fermi à pression ambiante dans la phase HO est déterminée en faisant une étude des fréquences d'oscillation en fonction de l'angle. Les masses effectives cyclotron sont déterminées avec des mesures des oscillations en fonction de la température. Deux nouvelles branches lourdes sont détectées sur des cristaux d'une très bonne qualité. En comparant ces mesures avec des mesures sous pression dans la phase AF, il est possible de montrer que la surface de Fermi ne change pas entre les deux phases et que le doublement de la maille a lieu dans les deux phases. Le comportement sous champ magnétique est étudié.

La dernière partie du chapitre 3 présente une étude du comportement en température de la résistivité de URu_2Si_2 en fonction de la pression. Ce comportement change d'une dépendance plus faible que T^2 dans la phase HO à une dépendance en T^2 dans la phase AF.

Chapitre 4

Le dernier chapitre décrit mes résultats sur le composé UCoGe. Après une introduction, deux paragraphes décrivent, comment le diagramme de phase sous pression a d'abord été déterminé sur un polycristal avec des mesures de résistivité et ensuite sur un " presque " monocristal (polycristal avec de grands grains monocristallins) avec des mesures de résistivité et susceptibilité simultanées. Le ferromagnétisme est supprimé sous pression et la température de Néel peut être détectée jusqu'à 1 GPa où elle devient égale à la température critique supraconductrice. Celle-ci augmente légèrement de la pression ambiante jusqu'à cette pression. Ensuite elle diminue légèrement mais est détectée jusqu'à la pression mesurée la plus haute de 2.4 GPa. Les mesures de calorimétrie alternative sur un monocristal montrent que la supraconductivité dans la phase paramagnétique est volumique.

4.7 Conclusion française

Cette thèse présente des résultats sur deux composés de fermion lourd à base d'uranium, le composé URu_2Si_2 qui présente à basse température l'ordre caché (HO) et le supraconducteur ferromagnétique UCoGe.

Des techniques de mesures très variées sous pression et sous haut champ magnétique ont été utilisées pour explorer les états fondamentaux de ces matériaux dans un large domaine de paramètres. Des mesures de résistivité, susceptibilité alternative et calorimétrie alternative ont été effectuées dans une cellule de pression à enclumes en diamant et une cellule de pression piston cylindre. Les conditions extrêmes de mesures étaient des pressions jusqu'à 2.4 GPa, des températures jusqu'à 20 mK et des champs magnétiques jusqu'à 13 T.

Le diagramme de phase de URu_2Si_2 est maintenant bien établi. Le choix de comparer les propriétés électroniques et magnétiques des phases HO et AF induite sous pression est pertinent pour élucider le vecteur d'ordre du paramètre d'ordre HO. Un premier résultat important était l'identification de l'excitation magnétique propre à la phase HO à travers des mesures de diffusion inélastiques de neutrons. C'était la première indication que le vecteur d'ordre de la phase HO pourrait être le même que le vecteur d'ordre de la phase AF. Ceci est supporté par le comportement de paramètre d'ordre de la dépendance en température de l'intensité de l'excitation. C'est une explication naturelle du comportement similaire de la résistivité et de la chaleur spécifique dans les deux phases.

Jusqu'à ce que le paramètre d'ordre soit observé directement, il n'est pas clair quelles symétries sont brisées dans la phase HO. Néanmoins, quand une symétrie du cristal est brisée, ceci a un effet sur la surface de Fermi. L'étude de la surface de Fermi présentée dans cette thèse à pression ambiante et sous pression par des mesures de Shubnikov-de Haas (SdH) donne un résultat expérimental important[2] et un grand pas dans l' élucidation du paramètre d'ordre HO. Ces expériences, où plus que 50 % de la surface de Fermi est détecté, vont permettre la comparaison avec les différentes théories, c'est à dire la confrontation de la surface de Fermi calculée à partir d'un paramètre d'ordre proposé avec la surface de Fermi mesurée.

La dépendance angulaire des fréquences SdH, leur valeur assez petite et leur insensibilité à la pression sont en bon accord avec le changement de symétrie de tétragonal centré dans la phase paramagnétique à tétragonal simple dans les phases HO et AF. Ceci peut être expliqué par le fait que la symétrie cristalline est la même dans les deux phases HO et AF grâce au même vecteur d'ordre.

Jusqu'à présent, le seul calcul de bande de référence est ceux de Elgazzar et al. (2009) et Oppeneer et al. (2010) dans la phase AF. L'accord est assez bon. Il y a deux autres propositions récentes de paramètre d'ordre HO (l'ordre quadripolaire (Harima 2010) et l'ordre hexadécapolaire de (Haule and Kotliar 2009)) avec le même vecteur d'ordre. Mais dans les deux cas, le paramètre d'ordre n'a pas été inclus dans les calculs de bande pour proposer une surface de Fermi et notamment la dépendance angulaire des fréquences d'oscillations. Un test décisif sera de vérifier si ces calculs décrivent les donnés expérimentales encore mieux ou s'il est trop difficile de prendre en compte les corrélations dans ce composé.

[2]Un résumé plus détaillé de ces résultats se trouve dans la conclusion du chapitre 3.

Les théories doivent expliquer aussi l'anisotropie contradictoire des masses effectives déterminé par des mesures de SdH et autres expériences comme l'anisotropie de H_{c2}.

Dans la deuxième partie de cette thèse, le diagramme de phase sous pression du supraconducteur ferromagnétique UCoGe a été déterminé par résistivité et susceptibilité alternative. La transition ferromagnétique est supprimée sous pression et peut être suivi jusqu'à la pression où sa température de transition devient inférieure à la température de transition supraconductrice $P_c^\star = 1.2\,\mathrm{GPa}$. La phase supraconductrice s'étend dans la phase paramagnétique jusqu'à la pression la plus haute mesurée de 2.4 GPa. La nature volumique de la supraconductivité a été confirmée par des mesures de calorimétrie alternative à 1.6 GPa. La phase supraconductrice forme un dôme avec la température de transition maximale à $P_c^\star$ où $T_{Curie} = T_{sc}$. Contrairement aux théories basées sur une singularité magnétique quantique du deuxième ordre, on n'observe pas de minimum de la température de transition supraconductrice à cette pression.

A présent, les questions ouvertes concernent le comportement de T_{Curie} quand elle devient plus petite que T_{sc} et l'ordre de la transition ferromagnétique. Pour répondre à ces questions, une étude complète thermodynamique est nécessaire. Les mesures de RMN récentes semblent montrer que déjà à pression nulle la transition paramagnétique-ferromagnétique est du premier ordre.

UCoGe semble avoir sous champ magnétique des propriétés en commun avec d'autres supraconducteurs ferromagnétiques comme la phase supraconductrice réentrante lié à soit du métamagnétisme comme dans UGe_2 soit à une transition de réorientation des moments sous champs comme dans URhGe. Mais il reste beaucoup de questions ouvertes. Il serait intéressant de voir si la transition ferromagnétique se termine dans un point tricritique prédit par la théorie et si un diagramme de "wings" va être observé comme dans UGe_2. Les supraconducteurs ferromagnétiques présentent un nouveau champ d'étude. Deux points importants pour un progrès dans ce champ sont la qualité cristalline et la découverte d'un système idéal comme par exemple les systèmes 115 à base de cérium. Ceux-ci ont été des cas idéaux pour étudier l'interaction entre antiferromagnétisme et supraconductivité dans les composés à fermions lourds.

Bibliography

H. Adachi and M. Sigrist. Anomalous thermal conductivity of semi-metallic superconductors with electron-hole compensation. *J. Phys. Soc. Jpn.*, 77:053704, 2008.

G. Aeppli, E. Bucher, C. Broholm, J. K. Kjems, J. Baumann, and J. Hufnagl. Magnetic order and fluctuations in superconducting UPt3. *Phys. Rev. Lett.*, 60:615–618, 1988.

A. Amato, M. J. Graf, A. de Visser, H. Amitsuka, D. Andreica, and A. Schenck. Weak-magnetism phenomena in heavy-fermion superconductors: selected μSR studies. *J. Phys.: Condens. Matter*, 16:S4403–S4420, 2004.

H. Amitsuka, M. Sato, N. Metoki, M. Yokoyama, K. Kuwahara, T. Sakakibara, H. Morimoto, S. Kawarazaki, Y. Miyako, and J. A. Mydosh. Effect of pressure on tiny antiferromagnetic moment in the heavy-electron compound URu_2Si_2 *Phys. Rev. Lett.*, 83:5114–5117, 1999.

H. Amitsuka, K. Matsuda, I. Kawasaki, K. Tenya, and M. Yokoyama. Pressure-temperature phase diagram of the heavy-electron superconductor URu_2Si_2. *J. Magn. Magn. Mater.*, 310:214–220, 2007.

H. Amitsuka, K. Matsuda, M. Yokoyama, I. Kawasaki, S. Takayama, Y. Ishihara, K. Tenya, N. Tatelwa, T. C. Kobayashi, and H. Yoshizawa. Dependence of pressure-induced phase transitions on pressure-transmitting media in the heavy-electron superconductor URu_2Si_2. *Physica B:*, 403:925–927, 2008.

D. Aoki, A. Huxley, E. Ressouche, D. Braithwaite, J. Flouquet, J. P. Brison, E. Lhotel, and C. Paulsen. Coexistence of superconductivity and ferromagnetism in URhGe. *Nature*, 413:613–616, 2001.

D. Aoki, F. Bourdarot, E. Hassinger, G. Knebel, A. Miyake, S. Raymond, V. Taufour, and J. Flouquet. Field reentrance of the hidden order state of URu_2Si_2 under pressure. *J. Phys. Soc. Jpn.*, 78:053701, 2009a.

D. Aoki, T. D. Matsuda, V. Taufour, E. Hassinger, G. Knebel, and J. Flouquet. Extremely large and anisotropic upper critical field and the ferromagnetic instability in UCoGe. *J. Phys. Soc. Jpn.*, 78:113709, 2009b.

D. Aoki, F. Bourdarot, E. Hassinger, G. Knebel, A. Miyake, S. Raymond, V. Taufour, and J. Flouquet. Field re-entrant hidden-order phase under pressure in URu_2Si_2. *J. Phys. Condens. Matter*, 22:164205, 2010.

A. Auerbach and K. Levin. Universal low-temperature properties of normal heavy-fermion systems. *J. Appl. Phys.*, 61:3162–3167, 1987.

P. Aynajian, E. H. D. Neto, C. V. Parker, Y. K. Huang, A. Pasupathy, J. Mydosh, and A. Yazdani. Visualizing the formation of the Kondo lattice and the hidden order in URu_2Si_2. *Proc. Nat. Acad. Sci. U.S.A.*, 107:10383–10388, 2010.

S. H. Baek, M. J. Graf, A. V. Balatsky, E. D. Bauer, C. Cooley, J. L. Smith, and N. J. Curro. Antiferromagnetic patches and hidden order in URu_2Si_2 by impurity doping. *Phys. Rev. B*, 81:132404, 2010.

K. Bakker, A. de Visser, E. Bruck, A. A. Menovsky, and J. J. M. Franse. Anisotropic variation of T_c and t_n in URu_2Si_2 by uniaxial pressure. *J. Magn. Magn. Mater.*, 108: 63–64, 1992.

A. V. Balatsky, A. Chantis, H. P. Dahal, D. Parker, and J. X. Zhu. Incommensurate spin resonance in URu_2Si_2. *Phys. Rev. B*, 79:214413, 2009.

E. D. Bauer. *lecture script*, 2007.

M.T. Béal-monod, S. K. Ma, and D. R. Fredkin. Temperature dependence of spin susceptibility of a nearly ferromagnetic Fermi liquid. *Phys. Rev. Lett*, 20:929, 1968.

K. Behnia, R. Bel, Y. Kasahara, Y. Nakajima, H. Jin, H. Aubin, K. Izawa, Y. Matsuda, J. Flouquet, Y. Haga, Y. Onuki, and P. Lejay. Thermal transport in the hidden-order state of URu_2Si_2. *Phys. Rev. Lett.*, 94:156405, 2005.

R. Bel, H. Jin, K. Behnia, J. Flouquet, and P. Lejay. Thermoelectricity of URu_2Si_2: Giant nernst effect in the hidden-order state. *Phys. Rev. B*, 70:220501, 2004.

D. Belitz, T. R. Kirkpatrick, and T. Vojta. First order transitions and multicritical points in weak itinerant ferromagnets. *Phys. Rev. Lett.*, 82:4707–4710, 1999.

C. Bergemann, S. R. Julian, G. J. McMullan, B. K. Howard, G. G. Lonzarich, P. Lejay, J. P. Brison, and J. Flouquet. Quantum oscillations in URu_2Si_2. *Physica B*, 230: 348–350, 1997.

N. Bernhoeft, G. H. Lander, M. J. Longfield, S. Langridge, D. Mannix, E. Lidstrom, E. Colineau, A. Hiess, C. Vettier, F. Wastin, J. Rebizant, and P. Lejay. Fragile thermodynamic order. *Acta Phys. Pol. B*, 34:1367–1376, 2003.

D. A. Bonn, J. D. Garrett, and T. Timusk. Far-infrared properties of URu_2Si_2. *Phys. Rev. Lett*, 61:1305–1308, 1988.

F. Bourdarot, B. Fak, K. Habicht, and K. Prokes. Inflection point in the magnetic field dependence of the ordered moment of URu_2Si_2 observed by neutron scattering in fields up to 17 T. *Phys. Rev. Lett.*, 90:067203, 2003a.

F. Bourdarot, B. Fak, V. P. Mineev, M. E. Zhitomirsky, N. Kernavanois, S. Raymond, P. Burlet, F. Lapierre, P. Lejay, and J. Flouquet. Pressure dependence of magnetism in URu_2Si_2. *arXiv0312206*, 2003b.

F. Bourdarot, B. Fåk, V. P. Mineev, M. E. Zhitomirsky, N. Kernavanois, S. Raymond, F. Lapierre, P. Lejay, and J. Flouquet. Pressure dependence of magnetic transitions in URu_2Si_2. *Physica B*, 350:e179–e181, 2004.

F. Bourdarot, A. Bombardi, P. Burlet, M. Enderle, J. Flouquet, P. Lejay, N. Kernavanois, V. P. Mineev, L. Paolasini, M. E. Zhitomirsky, and B. Fak. Hidden order in URu_2Si_2. *Physica B: Condens. Matter*, 359:986–993, 2005a.

F. Bourdarot, B. Fak, F. Lapierre, I. Sheikin, and P. Lejay. Magnetic phase diagram of $URu_{0.98}Rh_{0.02})_2Si_2$. *Physica B:*, 359:1132–1134, 2005b.

F. Bourdarot, E. Hassinger, S. Raymond, D. Aoki, V. Taufour, and J. Flouquet. Temperature dependence of the energy gap in the superconducting state in URu_2Si_2. *J. Phys. Soc. Jpn.*, 79:094706, 2010a.

F. Bourdarot, E. Hassinger, S. Raymond, D. Aoki, V. Taufour, L. P. Regnault, and J. Flouquet. Precise study of the resonance at Q(0) = (1,0,0) in URu_2Si_2. *J. Phys. Soc. Jpn.*, 79:064719, 2010b.

N. B. Brandt and V. V. Moschalkov. Concentrated Kondo systems. *Adv. Phys.*, 33: 373–467, 1984.

P. W. Bridgman. *Proc. Am. Acad. Arts Sci.*, 68:27, 1932.

E. Oran Brigham. *The Fast Fourier Transform*. Prentice Hall, Inc., Englewood Cliffs, N. J., 1974.

J. P. Brison, N. Keller, A. Verniere, P. Lejay, L. Schmidt, A. Buzdin, J. Flouquet, S. R. Julian, and G. G. Lonzarich. Anisotropy of the upper critical-field in URu_2Si_2 and FFLO state in antiferromagnetic superconductors. *Physica C*, 250:128–138, 1995.

C. Broholm, J. K. Kjems, W. J. L. Buyers, P. Matthews, T. T. M. Palstra, A. A. Menovsky, and J. A. Mydosh. Magnetic excitations and ordering in the heavy-electron superconductor URu_2Si_2. *Phys. Rev. Lett.*, 58:1467–1470, 1987.

C. Broholm, H. Lin, P. T. Matthews, T. E. Mason, W. J. L. Buyers, M. F. Collins, A. A. Menovsky, J. A. Mydosh, and J. K. Kjems. Magnetic excitations in the heavy-fermion superconductor URu_2Si_2. *Phys. Rev. B*, 43:12809–12822, 1991.

K. H. J. Buschow, E. Bruck, R. G. Vanwierst, F. R. Deboer, L. Havela, V. Sechovsky, P. Nozar, E. Sugiura, M. Ono, M. Date, and A. Yamagishi. Specific-heat and magnetic-behavior of UTGe compounds. *J. Appl. Phys.*, 67:5215–5217, 1990.

N. P Butch et al. *to be published*, 2010.

P. Chandra, P. Coleman, and J. A. Mydosh. Pressure-induced magnetism and hidden order in URu_2Si_2. *Physica B*, 312:397–400, 2002.

J. Chaussy, P. Gandit, K. Matho, and A. Ravex. Absolute thermoelectric-power of AuFe alloys between 0.01 K and 7 K. *J. Low Temp. Phys.*, 49:167–175, 1982.

A. V. Chubukov, C. Pepin, and J. Rech. Instability of the quantum-critical point of itinerant ferromagnet. *Phys. Rev. Lett.*, 92:147003, 2004.

P. Coleman, C. Pepin, Q. M. Si, and R. Ramazashvili. How do fermi liquids get heavy and die? *J. Phys. Condens. Matter*, 13:R723–R738, 2001.

F. Cricchio, F. Bultmark, O. Granas, and L. Nordstrom. Itinerant magnetic multipole moments of rank five as the hidden order in URu_2Si_2. *Phys. Rev. Lett*, 103:107202, 2009.

A. L. Dawson, W. R. Datars, J. D. Garrett, and F. S. Razavi. Electrical transport in URu_2Si_2. *J. Phys. Condens. Matter*, 1:6817–6828, 1989.

P. de la Mora and O. Navarro. Electronic structure of the ferromagnetic superconductor UCoGe from first principles. *J. Phys. Condens. Matter*, 20:285221, 2008.

J. Derr, G. Knebel, B. Salce, M-A Méasson, and J. Flouquet. Valence and magnetic ordering in intermediate valence compounds: TmSe versus SmB_6. *J. Phys. Condens. Matter*, 18:2089, 2006.

A. de Visser, F. E. Kayzel, A. A. Menovsky, J. J. M. Franse, J. Vandenberg, and G. J. Nieuwenhuys. Thermal-expansion and specific-heat of monocrystalline URu_2Si_2. *Phys. Rev. B*, 34:8168–8171, 1986.

A. de Visser, N. T. Huy, A. Gasparini, D. E. de Nijs, D. Andreica, C. Baines, and A. Amato. Muon spin rotation and relaxation in the superconducting ferromagnet UCoGe. *Phys. Rev. Lett.*, 102:167003, 2009.

F. R. DeBoer, J. J. M. Franse, E. Louis, A. A. Menovsky, J. A. Mydosh, T. T. M. Palstra, U. Rauchschwalbe, W. Schlabitz, F. Steglich, and A. de Visser. High-magnetic-field and high-pressure effects in monocrystalline URu_2Si_2. *Physica B & C*, 138(1-2):1–6, March 1986.

A. Demuer, C. Marcenat, J. Thomasson, R. Calemczuk, B. Salce, P. Lejay, D. Braithwaite, and J. Flouquet. Calorimetric study of $CeRu_2Ge_2$ under continuously swept hydrostatic pressure up to 8 GPa. *J. Low Temp. Phys.*, 120:245–257, 2000.

R. B. Dingle. *Proc. Roy. Soc. A*, 211:517, 1952.

M. Divis. Electronic structure and magnetism of UCoGe from first principles. *Physica B*, 403:2505–2508, 2008.

N. Doiron-Leyraud, I. R. Walker, L. Taillefer, M. J. Steiner, S. R. Julian, and G. G. Lonzarich. Fermi-liquid breakdown in the paramagnetic phase of a pure metal. *Nature*, 425:595–599, 2003.

N. Doiron-Leyraud, P. Auban-Senzier, S. René de Cotret, C. Bourbonnais, D. Jérome, K. Bechgaard, and L. Taillefer. Correlation between linear resistivity and T_c in the Bechgaard salts and the pnictide superconductor Ba (Fe1-x Cox) 2 As2. *Phys. Rev. B*, 80:214531, 2009.

S. Doniach. Kondo lattice and weak antiferromagnetism. *Physica B & C*, 91:231–234, 1977.

S. Doniach and S. Engelsberg. Low-temperature properties of nearly ferromagnetic Fermi liquids. *Phys. Rev. Lett*, 17:750–&, 1966.

Y: Dubi and A. V. Balatsky. Hybridization wave as the "hidden order" in URu_2Si_2. *to be published*, 2010.

S. Elgazzar, J. Rusz, M. Amft, P. M. Oppeneer, and J. A. Mydosh. Hidden order in URu_2Si_2 originates from Fermi surface gapping induced by dynamic symmetry breaking. *Nat. Mater.*, 8:337–341, 2009.

C. Enss and S. Hunklinger. *Low Temperature Physics*. Springer Verlag, Heidelberg, 2005.

B. Fak, C. Vettier, J. Flouquet, F. Bourdarot, S. Raymond, A. Verniere, P. Lejay, P. Boutrouille, N. R. Bernhoeft, S. T. Bramwell, R. A. Fisher, and N. E. Phillips. Influence of sample quality on the magnetic properties of URu_2Si_2. *J. Magn. Magn. Mat.*, 154:339–350, 1996.

E. Fawcett. Spin-density-wave antiferromagnetism in chromium. *Rev. Mod. Phys.*, 60: 209–283, 1988.

E. Fawcett, H. L. Alberts, V. Y. Galkin, D. R. Noakes, and J. V. Yakihmi. Spin-density-wave antiferromagnetism in chromium-alloys. *Rev. Mod. Phys.*, 66:25–127, 1994.

D. Fay and J. Appel. Coexistence of p-state superconductivity and itinerant ferromagnetism. *Phys. Rev. B*, 22:3173–3182, 1980.

J. Flouquet. *Progress in Low Temperature Physics*, chapter On the heavy fermion road, page 139. Amsterdam: Elsevier, 2005.

J. L. Fry, N. E. Brener, J. L. Thompson, and P. H. Dickinson. Hartree band-structure, Fermi-surface, and nesting wave vector for paramagnetic chromium. *Phys. Rev. B*, 21: 384–390, 1980.

P. Fulde. *Electron Correlations in Molecules and Solids*. Springer, Berlin, 1995.

A. Gasparini, Y. K. Huang, J. Hartbaum, H. von Lohneysen, and A. de Visser. Thermal expansion of the superconducting ferromagnet ucoge. *Phys. Rev. B*, 82:052502, 2010. doi: 10.1103/PhysRevB.82.052502.

F. Hardy. *to be published*, 2010.

F. Hardy and A. D. Huxley. P-wave superconductivity in the ferromagnetic superconductor URhGe. *Phys. Rev. Lett*, 94:247006, 2005.

F. Hardy, A. Huxley, J. Flouquet, B. Salce, G. Knebel, D. Braithwaite, D. Aoki, M. Uhlarz, and C. Pfleiderer. (P,T) phase diagram of the ferromagnetic superconductor URhGe. *Physica B:*, 359:1111–1113, 2005.

H. Harima, K. Miyake, and J. Flouquet. Why the hidden order in URu_2Si_2 is still hidden-one simple answer. *J. Phys. Soc. Jpn.*, 79:033705, 2010.

S. Harima. *private communication and SCES conference proceedings*, 2010.

E. Hassinger, G. Knebel, K. Izawa, P. Lejay, B. Salce, and J. Flouquet. Temperature-pressure phase diagram of URu_2Si_2 from resistivity measurements and ac calorimetry: Hidden order and Fermi-surface nesting. *Phys. Rev. B*, 77:115117, 2008.

E. Hassinger, G. Knebel, T. Matsuda, D. Aoki, V. Taufour, and J. Flouquet. Similarity of the Fermi surface in the hidden order state and the antiferromagnetic state of URu_2Si_2. *submitted to Phys. Rev. Lett.*, 2010.

K. Haule and G. Kotliar. Arrested Kondo effect and hidden order in URu_2Si_2. *Nat. Phys.*, 5:796–799, 2009.

K. Haule and G. Kotliar. Complex Landau-Ginzburg theory of the hidden order in URu_2Si_2. *Europhys. Lett.*, 89:57006, 2010.

N. Hessel Andersen. *Crystalline Field and Structural Effects in f-Electron Systems*, page 373. Plenum, New York, 1980.

K. Hiebl, C. Horvath, P. Rogl, and M. J. Sienko. Magnetic-properties and structural chemistry of ternary silicides (rare-earth, Th, U)Ru_2Si_2. *J. Magn. Magn. Mat.*, 37: 287–296, 1983.

T. Honma, Y. Haga, E. Yamamoto, N. Metoki, Y. Koike, H. Ohkuni, N. Suzuki, and Y. Onuki. Interplay between magnetism and superconductivity in URu_2Si_2 studied by neutron scattering experiments. *J. Phys. Soc. Jpn.*, 68:338–341, 1999.

N. T. Huy and A. de Visser. Ferromagnetic order in U(Rh, Co)Ge. *Solid State Commun.*, 149:703–706, 2009.

N. T. Huy, A. Gasparini, D. E. de Nijs, Y. Huang, J. C. P. Klaasse, T. Gortenmulder, A. de Visser, A. Hamann, T. Gorlach, and H. von Lohneysen. Superconductivity on the border of weak itinerant ferromagnetism in UCoGe. *Phys. Rev. Lett.*, 99:067006, 2007.

N. T. Huy, D. E. de Nijs, Y. K. Huang, and A. de Visser. Unusual upper critical field of the ferromagnetic superconductor UCoGe. *Phys. Rev. Lett.*, 1:077002, 2008.

H. Ikeda and Y. Ohashi. Theory of unconventional spin density wave: A possible mechanism of the micromagnetism in U-based heavy fermion compounds. *Phys. Rev. Lett*, 81:3723–3726, 1998.

K. Iki, G. Oomi, Y. Uwatoko, H. Takahashi, N. Mori, Y. Onuki, and T. Komatsubara. The effect of pressure on the Neel temperature of URu_2Si_2. *J. Alloys Compd.*, 181: 71–75, 1992.

E. S. Itskevich and V. F. Kraidenov. Measurement of temperatures in the liquid-helium region under pressure. *Instrum. Exp. Tech.*, 21:1640–1643, 1978.

J. R. Jeffries. *arXiv:1002.2245v1*, 2010.

J. R. Jeffries, N. P. Butch, B. T. Yukich, and M. B. Maple. The evolution of the ordered states of single-crystal URu_2Si_2 under pressure. *J. Phys. Condens. Matter*, 20:095225, 2008.

D. Jerome, A. Mazaud, M. Ribault, and K. Bechgard. Superconductivity in a synthetic organic conductor (TMTSF)2PF6. *Comptes Rendus Hebdomadaires Des Seances De L Academie Des Sciences Serie B*, 290:27–30, 1980.

Y. J. Jo, L. Balicas, C. Capan, K. Behnia, P. Lejay, J. Flouquet, J. A. Mydosh, and P. Schlottmann. Field-induced fermi surface reconstruction and adiabatic continuity between antiferromagnetism and the hidden-order state in URu_2Si_2. *Phys. Rev. Lett.*, 98:166404, 2007.

Y. J. Jo, L. Balicas, C. Capan, K. Behnia, P. Lejay, J. Flouquet, J. A. Mydosh, and P. Schlottmann. Pressure effect on the magnetic field-temperature (H-T) phase diagram of URu_2Si_2. *Physica B*, 403:749–751, 2008.

K. Kadowaki and S. B. Woods. Universal relationship of the resistivity and specific-heat in heavy-fermion compounds. *Solid State Commun.*, 58:507–509, 1986.

Y. Kasahara, T. Iwasawa, H. Shishido, T. Shibauchi, K. Behnia, Y. Haga, T. D. Matsuda, Y. Onuki, M. Sigrist, and Y. Matsuda. Exotic superconducting properties in the electron-hole-compensated heavy-fermion "semimetal" URu_2Si_2. *Phys. Rev. Lett*, 99: 116402, 2007.

T. Kasuya. Hidden ordering and heavy mass in URu_2Si_2 and its alloys. *J. Phys. Soc. Jpn.*, 66:3348–3351, 1997.

T. Kasuya, O. Sakai, H. Harima, and M. Ikeda. Consistent treatment of high and low-frequency phenomena in Kondo and vf systems. *J. Magn. Magn. Mater.*, 76-7:46–52, 1988.

N. Keller, S. A. J. Wiegers, J. A. A. J. Perenboom, A. de Visser, A. A. Menovsky, and J. J. M. Franse. Fermi surface and heavy quasi-particles of URu_2Si_2. *J. Magn. Magn. Mat.*, 177:298–299, 1998.

J. S. Kim, D. Hall, P. Kumar, and G. R. Stewart. Specific heat of URu_2Si_2 in fields up to 42 T: Clues to the hidden order. *Phys. Rev. B*, 67:014404, 2003a.

K. H. Kim, N. Harrison, M. Jaime, G. S. Boebinger, and J. A. Mydosh. Magnetic-field-induced quantum critical point and competing order parameters in URu_2Si_2. *Phys. Rev. Lett.*, 91:256401, 2003b.

K. H. Kim, N. Harrison, M. Jaime, G. S. Boebinger, and J. A. Mydosh. Novel competing orders near the field-induced quantum critical point in URu_2Si_2. *J. Magn. Magn. Mater.*, 272:50–51, 2004.

T. R. Kirkpatrick and D. Belitz. Coexistence of ferromagnetism and superconductivity. *Phys. Rev. B*, 67:24515–1–15, 2003.

A. Kiss and P. Fazekas. Group theory and octupolar order in URu_2Si_2. *Phys. Rev. B*, 71: 054415, 2005.

R. A. Klemm and K. Scharnberg. Upper critical-field in p-wave superconductors with anisotropic pairing interactions. *Physica B & C*, 135:53–56, 1985.

G. Knebel, D. Braithwaite, P. C. Canfield, G. Lapertot, and J. Flouquet. Electronic properties of $CeIn_3$ under high pressure near the quantum critical point. *Phys. Rev. B*, 65:024425, 2002.

G. Knebel, M. A. Measson, B. Salce, D. Aoki, D. Braithwaite, J. P. Brison, and J. Flouquet. High-pressure phase diagrams of $CeRhIn_5$ and $CeCoIn_5$ studied by ac calorimetry. *J. Phys. Condens. Matter*, 16:8905–8922, 2004.

G. Knebel, D. Aoki, D. Braithwaite, B. Salce, and J. Flouquet. Coexistence of antiferromagnetism and superconductivity in $CeRhIn_5$ under high pressure and magnetic field. *Phys. Rev. B*, 74:020501, 2006.

J. Kondo. Resistance minimum in dilute magnetic alloys. *Prog. Theor. Phys.*, 32:37, 1964.

J. F. Kwak. Fermi-surface nesting, closed orbits, and the threshold field in an organic superconductor. *Phys. Rev. B*, 28:3277–3282, 1983.

L. D. Landau. The theory of a Fermi liquid. *Soviet Physics Jetp-ussr*, 3:920–925, 1957.

A. J. Leggett. A theoretical description of the new phases of liquid ^{3}He. *Rev. Mod. Phys.*, 47:331, 1975.

J. Levallois, K. Behnia, J. Flouquet, P. Lejay, and C. Proust. On the destruction of the hidden order in URu_2Si_2 by a strong magnetic field. *Europhys. Lett.*, 85:27003, 2009.

J. Levallois, F. Levy-Bertand, J. Tran, M. K. Mydosh, Y. Huang, and D. van der Marel. Hybridization gap and anisotropic far-infrared optical conductivity of URu_2Si_2. *to be published*, 2010.

F. Levy, I. Sheikin, B. Grenier, and A. D. Huxley. Magnetic field-induced superconductivity in the ferromagnet URhGe. *Science*, 309:1343–1346, 2005.

I. M. Lifshitz and A. M. Kosevitch. *Sov. Phys.-JETP*, 2:636, 1956.

G. G. Lonzarich. *Electron.* Cambridge University Press, 1997.

L. Malone et al. *to be published*, 2010.

M. B. Maple, J. W. Chen, Y. Dalichaouch, T. Kohara, C. Rossel, M. S. Torikachvili, M. W. McElfresh, and J. D. Thompson. Partially gapped Fermi-surface in the heavy-electron superconductor URu_2Si_2. *Phys. Rev. Lett.*, 56:185–188, 1986.

C. Marcenat, R. A. Fisher, N. E. Phillips, and J. Flouquet. Comparison of the specific-heat of heavy fermion cerium compounds. *J. Magn. Magn. Mat.*, 76-7:115–116, 1988.

M. Marcinkowski and H. A. Lipsitt. Electrical resistivity of chromium in vicinity of Neel temperature. *J. Appl. Phys.*, 32:1238, 1961.

T. E. Mason, H. Lin, M. F. Collins, W. J. L. Buyers, A. A. Menovsky, and J. A. Mydosh. Antiferromagnetism and superconductivity in URu_2Si_2. *Physica B*, 163:45–48, 1990.

T. E. Mason, W. J. L. Buyers, T. Petersen, A. A. Menovsky, and J. D. Garrett. Nontrivial magnetic order in URu_2Si_2. *J. Phys. Condens. Matter*, 7:5089–5096, 1995.

N. D. Mathur, F. M. Grosche, S. R. Julian, I. R. Walker, D. M. Freye, R. K. W. Haselwimmer, and G. G. Lonzarich. Magnetically mediated superconductivity in heavy fermion compounds. *Nature*, 394:39–43, 1998.

K. Matsuda, Y. Kohori, T. Kohara, K. Kuwahara, and H. Amitsuka. Spatially inhomogeneous development of antiferromagnetism in URu_2Si_2: Evidence from Si-29 NMR under pressure. *Phys. Rev. Lett*, 87:087203, 2001.

K. Matsuda, Y. Kohori, T. Kohara, H. Amitsuka, K. Kuwahara, and T. Matsumoto. The appearance of homogeneous antiferromagnetism in URu_2Si_2 under high pressure: a Si-29 nuclear magnetic resonance study. *J. Phys.: Condens. Matter*, 15:2363–2373, 2003.

T. Matsuda et al. *to be published*, 2010.

A. McCollam, S. R. Julian, P. M. C. Rourke, D. Aoki, and J. Flouquet. Anomalous de Haas-van Alphen oscillations in $CeCoIn_5$. *Phys. Rev. Lett.*, 94:186401, 2005.

M. W. McElfresh, J. D. Thompson, J. O. Willis, M. B. Maple, T. Kohara, and M. S. Torikachvili. Effect of pressure on competing electronic correlations in the heavy-electron system URu_2Si_2. *Phys. Rev. B*, 35:43–47, 1987.

A. J. Millis. Effect of a nonzero temperature on quantum critical-points in itinerant fermion systems. *Phys. Rev. B*, 48:7183–7196, 1993.

V. P. Mineev. Coexistence of triplet superconductivity and itinerant ferromagnetism. *Adv. Theor. Phys.*, 1134:68–73, 2009.

V. P. Mineev and T. Champel. Theory of superconductivity in ferromagnetic superconductors with triplet pairing. *Phys. Rev. B*, 69, 2004.

V. P. Mineev and M. E. Zhitomirsky. Interplay between spin-density wave and induced local moments in URu_2Si_2. *Phys. Rev. B*, 72:014432, 2005.

A. Miyake, D. Aoki, and J. Flouquet. Field re-entrant superconductivity induced by the enhancement of effective mass in URhGe. *J. Phys. Soc. Jpn.*, 77:094709, 2008.

A. Miyake, D. Aoki, and J. Flouquet. Pressure evolution of the ferromagnetic and field re-entrant superconductivity in URhGe. *J. Phys. Soc. Jpn.*, 78:063703, 2009.

K. Miyake and J. Flouquet. Note on anisotropy of resistivity in hidden ordered state of URu_2Si_2. *J. Phys. Soc. Jpn.*, 79:035001, 2010.

G. Motoyama, T. Nishioka, and N. K. Sato. Phase transition between hidden and antiferromagnetic order in URu_2Si_2. *Phys. Rev. Lett.*, 90:166402, 2003.

G. Motoyama, N. Yokoyama, A. Sumiyama, and Y. Oda. Electrical resistivity and thermal expansion measurements of URu_2Si_2 under pressure. *J. Phys. Soc. Jpn.*, 77:123710, 2008.

G. Motoyama, H. Sakai, A. Yamaguchi, A. Sumiyama, and Y. Oda. Anisotropy of magnetic susceptibility of URu_2Si_2 under pressure. *SCES conference proceedings*, 2010.

M. Nakashima, S. Ikeda, T. Okubo, Y. Inada, R. Settai, H. Ohkuni, E. Yamamoto, Y. Haga, and Y. Onuki. De Haas-van Alphen effect under pressure in URu_2Si_2. *Physica B*, 329:566–567, 2003.

G. J. Nieuwenhuys. Crystalline electric-field effects in UPt_2Si_2 and URu_2Si_2. *Phys. Rev. B*, 35:5260–5263, 1987.

P. G. Niklowitz, C. Pfleiderer, T. Keller, M. Vojta, Y. . K. Huang, and J. A. Mydosh. Parasitic small-moment antiferromagnetism and nonlinear coupling of hidden order and antiferromagnetism in URu_2Si_2 observed by larmor diffraction. *Phys. Rev. Lett.*, 104: 106406, 2010.

R. A. Noack and W. B. Holzapfel. *High Pressure Science and Technology*. Plenum, New York, 1979.

F. J. Ohkawa and H. Shimizu. Quadrupole and dipole orders in URu_2Si_2. *J. Phys. Condens. Matter*, 11:L519–L524, 1999.

H. Ohkuni, T. Ishida, Y. Inada, Y. Haga, E. Yamamoto, Y. Onuki, and S. Takahashi. De Haas-van Alphen oscillation in the superconducting mixed state of URu_2Si_2. *J. Phys. Soc. Jpn.*, 66:945–948, 1997.

H. Ohkuni, Y. Inada, Y. Tokiwa, K. Sakurai, R. Settai, T. Honma, Y. Haga, E. Yamamoto, Y. Onuki, H. Yamagami, S. Takahashi, and T. Yanagisawa. Fermi surface properties and de Haas-van Alphen oscillation in both the normal and superconducting mixed states of URu_2Si_2. *Philos. Mag. B*, 79:1045–1077, 1999.

T. Ohta, Y. Nakai, Y. Ihara, K. Ishida, K. Deguchi, N. K. Sato, and I. Satoh. Ferromagnetic quantum critical fluctuations and anomalous coexistence of ferromagnetism and superconductivity in UCoGe revealed by Co-NMR and NQR studies. *J. Phys. Soc. Jpn.*, 77:023707, 2008.

T. Ohta, T. Hattori, K. Ishida, Y. Nakai, E. Osaki, K. Deguchi, N. K. Sato, and I. Satoh. Microscopic coexistence of ferromagnetism and superconductivity in single-crystal UCoGe. *J. Phys. Soc. Jpn.*, 79:023707, 2010.

Y. Okuno and K. Miyake. Induced-moment weak antiferromagnetism and orbital order on the itinerant-localized duality model with nested fermi surface: A possible origin of exotic magnetism in URu_2Si_2. *J. Phys. Soc. Jpn.*, 67:2469–2476, 1998.

P. M. Oppeneer, J. Rusz, S. Elgazzar, M.-T. Suzuki, T. Durakiewicz, and J. Mydosh. Electrionic structure theory of the hidden order material URu_2Si_2. *to be published*, 2010.

D. D. Osheroff, W. J. Gully, Richards.RC, and D. M. Lee. New magnetic phenomena in liquid He-3 below 3 mK. *Phys. Rev. Lett*, 29:920–&, 1972.

T. T. M. Palstra, A. A. Menovsky, J. Vandenberg, A. J. Dirkmaat, P. H. Kes, G. J. Nieuwenhuys, and J. A. Mydosh. Superconducting and magnetic transitions in the heavy-fermion system URu_2Si_2. *Phys. Rev. Lett.*, 55(24):2727–2730, 1985.

T. T. M. Palstra, A. A. Menovski, and J. A. Mydosh. Anisotropic electrical-resistivity of the magnetic heavy-fermion superconductor URu_2Si_2. *Phys. Rev. B*, 33:6527–6530, 1986.

J. G. Park, K. A. McEwen, S. deBrion, G. Chouteau, H. Amitsuka, and T. Sakakibara. High-field magnetization study of single-csystal URu_2Si_2. *J. Phys. Condens. Mat.*, 9: 3065–3069, 1997.

C. Pfleiderer. Superconducting phases of f-electron compounds. *Rev. Mod. Phys.*, 81: 1551–1624, 2009.

C. Pfleiderer and A. D. Huxley. Pressure dependence of the magnetization in the ferromagnetic superconductor UGe_2. *Phys. Rev. Lett.*, 89:147005, 2002.

C. Pfleiderer, J. A. Mydosh, and M. Vojta. Pressure dependence of the magnetization of URu_2Si_2. *Phys. Rev. B*, 74:104412, 2006.

D. Pines and P. Nozière. *The theory of quantum liquids*. Benjamin, New York, 1966.

A. B. Pippard. *The Dynamics of Conduction Electrons*. Blackiee & Son, Glasgow, 1965a.

A. B. Pippard. *Proc. Roy. Soc.*, 287:165, 1965b.

A. B. Pippard. *Magnetoresistance in Metals*. Cambridge University Press, 1989.

J. Prokleska, J. Pospisil, J. P. Vejpravova, V. Sechovsky, and J. Sebek. Low temperature ac susceptibility of UCoGe crystals. *J. Physics: Conference Series*, 200:012161, 2010.

A. P. Ramirez, P. Coleman, P. Chandra, E. Bruck, A. A. Menovsky, Z. Fisk, and E. Bucher. Nonlinear susceptibility as a probe of tensor spin order in URu_2Si_2. *Phys. Rev. Lett*, 68:2680–2683, 1992.

R. Roussev and A. J. Millis. Quantum critical effects on transition temperature of magnetically mediated p-wave superconductivity. *Phys. Rev. B*, 63:140504, 2001.

M. A. Rudermann and C. Kittel. *Phys. Rev.*, 96, 1954.

T. Sakakibara, J. Custers, K. Yano, A. Yamada, T. Tayama, Y. Aoki, H. Sato, H. Sugawara, H. Amitsuka, and M. Yokoyama. Probing the nodal structures of heavy electron superconductors by means of specific heat measurements in magnetic fields. *Physica B*, 403:990–993, 2008.

M. Samsel-Czekala, S. Elgazzar, P. M. Oppeneer, E. Talik, W. Walerczyk, and R. Troc. The electronic structure of UCoGe by ab initio calculations and XPS experiment. *J. Phys. Condens. Matter*, 22:015503, 2010.

A. F. Santander-Syro, M. Klein, F. L. Boariu, A. Nuber, P. Lejay, and F. Reinert. Fermi-surface instability at the 'hidden-order' transition of URu_2Si_2. *Nat. Phys.*, 5:637–641, 2009.

P. Santini and G. Amoretti. Crystal-field model of the magnetic-properties of URu_2Si_2. *Phys. Rev. Lett*, 73:1027–1030, 1994.

S. S. Saxena, P. Agarwal, K. Ahilan, F. M. Grosche, R. K. W. Haselwimmer, M. J. Steiner, E. Pugh, I. R. Walker, S. R. Julian, P. Monthoux, G. G. Lonzarich, A. Huxley, I. Sheikin, D. Braithwaite, and J. Flouquet. Superconductivity on the border of itinerant-electron ferromagnetism in UGe_2. *Nature*, 406:587–592, 2000.

W. Schlabitz. In *Fourth International Conference on Valence Fluctuations, Cologne*, 1984.

A. R. Schmidt, M. H. Hamidian, P. Wahl, F. Meier, A. V. Balatsky, J. D. Garrett, T. J. Williams, G. M. Luke, and J. C. Davis. Imaging the fano lattice to 'hidden order' transition in URu_2Si_2. *Nature*, 465:570–576, 2010.

L. Schmidt. *Etude sous pression du fermion lourd URu_2Si_2*. PhD thesis, UJF Grenoble, 1993.

J. Schoenes, C. Schoeneberger, J. J. M. Franse, and A. A. Menovsky. Hall-effect and resistivity study of the heavy-fermion system URu_2Si_2. *Phys. Rev. B*, 35(10):5375–5378, April 1987.

G. Seyfarth, J. P. Brison, M. . A. Measson, J. Flouquet, K. Izawa, Y. Matsuda, H. Sugawara, and H. Sato. Multiband superconductivity in the heavy fermion compound $PrOs_4Sb_{12}$. *Phys. Rev. Lett.*, 95:107004, 2005.

P. A. Sharma, N. Harrison, M. Jaime, Y. S. Oh, K. H. Kim, C. D. Batista, H. Amitsuka, and J. A. Mydosh. Phonon thermal transport of URu_2Si_2: Broken translational symmetry and strong-coupling of the "hidden order" to the lattice. *Phys. Rev. Lett*, 97: 156401, 2006.

Q. G. Sheng and B. R. Cooper. Prediction of pressure-induced changes in magnetic-ordering of correlated-electron uranium systems. *J. Appl. Phys.*, 75:7035–7040, 1994.

H. Shishido, K. Hashimoto, T. Shibauchi, T. Sasaki, H. Oizumi, N. Kobayashi, T. Takamasu, K. Takehana, Y. Imanaka, T. D. Matsuda, Y. Haga, Y. Onuki, and Y. Matsuda. Possible phase transition deep inside the hidden order phase of ultraclean URu_2Si_2. *Phys. Rev. Lett.*, 102:156403, 2009.

D. Shoenberg. *Magnetic Oscillations in metals*. Cambridge University Press, New York, 1984.

A. V. Silhanek, N. Harrison, C. D. Batista, M. Jaime, A. Lacerda, H. Amitsuka, and J. A. Mydosh. Gamma(5) quasiparticles and avoided quantum criticality in $U(Ru,Rh)_{(2)}Si_2$. *Physica B*, 378-80:373–375, 2006.

E. Slooten, T. Naka, A. Gasparini, Y. K. Huang, and A. de Visser. Enhancement of superconductivity near the ferromagnetic quantum critical point in UCoGe. *Phys. Rev. Lett*, 103:097003, 2009.

A. V. Sologubenko, J. Jun, S. M. Kazakov, J. Karpinski, and H. R. Ott. Thermal conductivity of single-crystalline MgB_2. *Phys. Rev. B*, 66, 2002.

G. R. Stewart. *Rev. Mod. Phys*, 56, 1984.

G. R. Stewart, Z. Fisk, J. O. Willis, and J. L. Smith. Possibility of coexistence of bulk superconductivity and spin fluctuations in UPt_3. *Phys. Rev. Lett.*, 52:679–682, 1984.

K. Sugiyama, M. Nakashima, H. Ohkuni, K. Kindo, Y. Haga, T. Honma, E. Yamamoto, and Y. Onuki. Metamagnetic transition in a heavy fermion superconductor URu_2Si_2. *J. Phys. Soc. Jpn.*, 68:3394–3401, 1999.

P. F. Sullivan and G. Seidel. Steady-state ac-temperature calorimetry. *Phys. Rev.*, 173: 679, 1968.

A. Suslov, J. B. Ketterson, D. G. Hinks, D. F. Agterberg, and B. K. Sarma. H-T phase diagram of URu_2Si_2 in high magnetic fields. *Phys. Rev. B*, 68:020406, 2003.

S. Takagi, S. Ishihara, S. Saitoh, H. I. Sasaki, H. Tanida, M. Yokoyama, and H. Amitsuka. No evidence for "small-moment antiferromagnetism" under ambient pressure in URu_2Si_2 single-crystal Si-29 NMR study. *J. Phys. Soc. Jpn.*, 76:033708, 2007.

S. Takashima, M. Nohara, H. Ueda, N. Takeshita, C. Terakura, F. Sakai, and H. Takagi. Robustness of non-Fermi-liquid behavior near the ferromagnetic critical point in clean $ZrZn_2$. *J. Phys. Soc. Jpn.*, 76:043704, 2007.

N. Tateiwa and Y. Haga. Evaluations of pressure-transmitting media for cryogenic experiments with diamond anvil cell. *Rev. Sci. Instrum.*, 80:123901, 2009.

N. Tateiwa, Y. Haga, T. D. Matsuda, S. Ikeda, E. Yamamoto, Y. Okuda, Y. Miyauchi, R. Settai, and Y. Onuki. Strong-coupling superconductivity of $CeIrSi_3$ with the noncentrosymmetric crystal structure. *J. Phys. Soc. Jpn.*, 76:083706, 2007.

N. Tateiwa et al. *SCES conference proceedings*, 2010.

J. Thomasson et al. *private communication*, 1989.

R. Troc and V. H. Tran. Magnetic-properties of UT(Si, Ge) series. *J. Magn. Magn. Mat.*, 73:389–397, 1988.

R. Troc, R. Wawryk, W. Miiller, H. Misiorek, and M. Samsel-Czekala. Bulk properties of the UCoGe Kondo-like system. *Philos. Mag.*, 90:2249–2271, 2010.

S. Uemura, G. Motoyama, Y. Oda, T. Nishioka, and N. K. Sato. Correlation among long-range ordered states revealed by pressure versus temperature phase diagram in URu_2Si_2. *J. Phys. Soc. Jpn.*, 74:2667–2670, 2005.

N. H. van Dijk, A. de Visser, J. J. M. Franse, and A. A. Menovski. Thermal-expansion and magnetostriction of superconducting URu_2Si_2. *Phys. Rev. B*, 51:12665–12672, 1995.

C. M. Varma and L. J. Zhu. Helicity order: Hidden order parameter in URu_2Si_2. *Phys. Rev. Lett*, 96:036405, 2006.

A. Verniere, P. Lejay, J. X. Boucherle, J. Muller, S. Raymond, J. Flouquet, and A. Sulpice. Low temperature structural and physical behaviour of UIr_2Si_2 single crystal. *Physica B*, 206-207:509–11, 1995.

A. Verniere, S. Raymond, J. X. Boucherle, P. Lejay, B. Fak, J. Flouquet, and J. M. Mignot. Magnetic structure and physical properties of the heavy fermion UIr_2Si_2. *J. Magn. Magn. Mat.*, 153:55–62, 1996.

A. Villaume, F. Bourdarot, E. Hassinger, S. Raymond, V. Taufour, D. Aoki, and J. Flouquet. Signature of hidden order in heavy fermion superconductor URu_2Si_2: Resonance at the wave vector Q(0)=(1,0,0). *Phys. Rev. B*, 78:012504, 2008.

P. Wachter. *Handbook on the Physics and Chemistry of Rare Earths, vol. 19*, chapter 132, page 1. North Holland, Amsterdam, 1993.

S. Watanabe and K. Miyake. *to be published.*

C. R. Wiebe. APS march meeting. 2009.

C. R. Wiebe, G. M. Luke, Z. Yamani, A. A. Menovsky, and W. J. L. Buyers. Search for hidden orbital currents and observation of an activated ring of magnetic scattering in the heavy fermion superconductor URu_2Si_2. *Phys. Rev. B*, 69:132418, 2004.

C. R. Wiebe, J. A. Janik, G. J. MacDougall, G. M. Luke, J. D. Garrett, H. D. Zhou, Y. J. Jo, L. Balicas, Y. Qiu, J. R. D. Copley, Z. Yamani, and W. J. L. Buyers. Gapped itinerant spin excitations account for missing entropy in the hidden-order state of URu_2Si_2. *Nat. Phys.*, 3:96–100, 2007.

H. Wilhelm and D. Jaccard. Alternating current calorimetry at very high pressure and low temperature. *J. Phys. Condens. Matter*, 14:10683–10687, 2002.

H. Yamagami and N. Hamada. Relativistic electronic structure and fermi surface of URu_2Si_2 in antiferromagnetic state. *Physica B*, 284:1295–1296, 2000.

H. Yamagami et al. *SCES conference proceedings and private communication*, 2010.

K. Yano, T. Sakakibara, T. Tayama, M. Yokoyama, H. Amitsuka, Y. Homma, P. Miranovic, M. Ichioka, Y. Tsutsumi, and K. Machida. Field-angle-dependent specific heat measurements and gap determination of a heavy fermion superconductor URu_2Si_2. *Phys. Rev. Lett*, 100:017004, 2008.

D.-X. Yao and E. W. Carlson. Magnetic excitations in the high-T_c iron pnictides. *Phys. Rev. B*, 78:052507–1–4, 2008.

M. Yashima, S. Kawasaki, H. Mukuda, Y. Kitaoka, H. Shishido, R. Settai, and Y. Onuki. Quantum phase diagram of antiferromagnetism and superconductivity with a tetracritical point in $CeRhIn_5$ in zero magnetic field. *Phys. Rev. B*, 76:020509, 2007.

M. Yokoyama, H. Amitsuka, K. Tenya, K. Watanabe, S. Kawarazaki, H. Yoshizawa, and J. A. Mydosh. Competition between hidden order and antiferromagnetism in URu_2Si_2 under uniaxial stress studied by neutron scattering. *Phys. Rev. B*, 72:214419, 2005.

M. Yokoyama, K. Matsuda, H. Amitsuka, K. Tenya, N. Aso, and H. Yoshizawa. Low-energy magnetic fluctuations in $U(Ru_{1-x}Rh_x)_{(2)}Si_2$(x <= 0.02). *J. Magn. Magn. Mater.*, 310:328–330, 2007.

R. Yoshida, Y. Nakamura, M. Fukui, Y. Haga, E. Yamamoto, Y. Onuki, M. Okawa, S. Shin, M. Hirai, Y. Muraoka, and T. Yokoya. Clear signature of hidden order and evidence for unit cell doubling in URu_2Si_2. *to be published*, 2010.

Z. W. Zhu, E. Hassinger, Z. A. Xu, D. Aoki, J. Flouquet, and K. Behnia. Anisotropic inelastic scattering and its interplay with superconductivity in URu_2Si_2. *Phys. Rev. B*, 80:172501, 2009.

G. Zwicknagl, A. N. Yaresko, and P. Fulde. Microscopic description of origin of heavy quasiparticles in UPt_3. *Phys. Rev. B*, 65:081103, 2002.